

MILLIMETRE WAVE QUASI-OPTICAL SIGNAL PROCESSING SYSTEMS

M. R. Webb

**A Thesis Submitted for the Degree of PhD
at the
University of St. Andrews**



1993

**Full metadata for this item is available in
Research@StAndrews:FullText
at:**

<http://research-repository.st-andrews.ac.uk/>

Please use this identifier to cite or link to this item:

<http://hdl.handle.net/10023/2827>

This item is protected by original copyright

**This item is licensed under a
Creative Commons License**

MILLIMETRE WAVE QUASI-OPTICAL SIGNAL PROCESSING SYSTEMS

A thesis presented by
M. R. Webb B.E. *Hons Adelaide*
to the
University of St. Andrews
in application for the degree of
Doctor of Philosophy.

July 1992



Declaration

I hereby certify that this thesis has been composed by myself, that it is a record of my own work, and that it has not been accepted in partial or complete fulfilment of any other degree of professional qualification.

I was admitted to the Faculty of Science of the University of St. Andrews under Ordinance General No. 12 during July 1989, and as a candidate for the degree of Ph.D. during July 1990.

In submitting this thesis to the University of St. Andrews, I understand that I am giving permission for it to be made available for use in accordance with the regulations of the University Library for the time being in force, subject to any copyright vested in the work not being affected thereby. I also understand that the title and abstract will be published, and that a copy of the work may be made and supplied to any *bona fide* library or research worker.

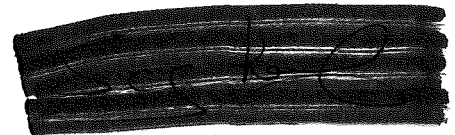


M. R. Webb

©1992

Certificate

I hereby certify that M. R. Webb has fulfilled the conditions of the Resolution and Regulations appropriate to the degree of Ph.D.

A dark, horizontal, textured rectangular area representing a handwritten signature, likely in ink on a light background.

Dr. J. C. G. Lesurf
Research Supervisor

Soli Deo Gloria

Acknowledgements

I cannot adequately express my gratitude to those who have enabled me to do the work that this thesis represents. In a large measure, the fruit of this thesis belongs to them also. I am indebted to them.

Jim, your insight into physical phenomena and in particular electromagnetic phenomena is tremendous, and has proved invaluable to me at every step along the way. You have been honest, supportive and encouraging. I will sorely miss you.

Gill, sharing this whole experience with you has been a real joy. It has been full of hard work for both of us. We have had our ups and downs, but it has been good to have been here with you.

Graham and Andy, my work would not have been possible if you had not gone before me and paved the way. It is easy to reach high, when you stand on the shoulders of giants. I have valued your friendship, encouragement and criticism. I hope our paths cross again in the future.

Mike, many of our circumstances are similar and it has been good to have been able to share this PhD experience with you. Your meticulous attention to detail has more than once come to my aid. Thank you for your friendship.

Malcolm, Darrell and Duncan, you have all been a source of encouragement and friendship. In a variety of ways, you have made my time spent both in the lab. and in St. Andrews, all the more enjoyable and enriching. Thank you for your friendship.

The University of St. Andrews mechanical workshop has provided essential support throughout my time here in St. Andrews. In particular, I would like to thank you Willie for all the work and advice you have given me; and George, you also have always been ready to help me in various ways. Without your contributions, I would quite literally have had very little to show for all my time here. Thank you both.

The Microwave Radar Division, DSTO Australia, has supported me personally throughout my three years here. At a specific time of difficulty, they provided much needed additional support and encouragement. Hugh, I have appreciated your guidance, advice and concern. I am indebted to both you and the Division. Thank you for always being there.

Abstract

The development of spatial signal processing techniques at millimetre wavelengths represents an area of science and technology that is new. At optical wavelengths, spatial signal processing techniques are well developed and are being applied to a variety of situations. In particular they are being used in pattern recognition systems with a great deal of success. At millimetre wavelengths, the kind of technology used for signal transport and processing is typically either waveguide based or quasi-optically based, or some hybrid of the two. It is the use of quasi-optical methods that opens up the possibility of applying some of the spatial signal processing techniques that up to the present time have almost exclusively been used at optical wavelengths.

A generic device that opens up this dimension of spatial signal processing to millimetre wave quasi-optical systems is at the heart of the work described within this thesis. The device could be suitably called a millimetre wave quasi-optical spatial light modulator (SLM), and is identical in operation to the spatial light modulators used in many optical signal processing systems. Within this thesis both a theoretical and an experimental analysis of a specific millimetre wave quasi-optical spatial light modulator is undertaken. This thesis thus represents an attempt to open up this new area of research and development, and to establish for it, a helpful theoretical and experimental foundation. It is an area that involves a heterogeneous mix of various technologies, and it is an area that is full of potential.

The development of the experimental method for measuring the beam patterns produced by millimetre wave quasi-optical spatial light modulators involved the separate development of two other components. Firstly, a sensitive, low-cost millimetre wave pyroelectric detector has been developed and characterised. And secondly, a high performance quasi-optical Faraday rotator (a polarisation rotator) has been developed and characterised. The polarisation state of a quasi-optical beam is the parameter most often exploited for signal processing applications in millimetre wave quasi-optical systems, and thus a high performance polarisation rotator has readily found many opportunities for use.

Contents

1	Spatial Signal Processing at Millimetre Wavelengths	5
2	Millimetre Wave Technology	9
2.1	Millimetre Wave Optics	9
2.1.1	Theoretical Methodology	9
2.1.2	MMW QO Devices and Systems	10
2.2	The Wider Context	13
2.2.1	Surveillance Technologies	13
2.2.2	Planar Grids	15
2.2.3	Mode Converters	15
2.2.4	Optical Signal Processing	16
2.2.5	MMW Propagation in the Atmosphere	16
2.2.6	Material Properties and Measurement Techniques	17
2.2.7	E-Plane Integrated Circuits	17
2.2.8	Communications	18
2.2.9	Radioastronomy	18
	References	19
3	SLM Pattern Analysis	27
3.1	The Angular Spectrum of Plane Waves	28
3.2	Gaussian Beam-Mode Optics	31
3.2.1	Derivation of Beam-modes	31
3.2.2	Application to MMW QO SLMs	38
3.2.3	Aperture Considerations	40
3.3	Fourier Optics	41
3.3.1	Coherent Optical Imaging	41

3.3.2	Apertures—Two Models	44
	References	45
4	SLM Pattern Measurement	47
4.1	MMW QO SLM Design	48
4.1.1	Background	48
4.1.2	A Mechanical Spatial Phase Modulator	49
4.1.3	Future Directions for MMW QO SLMs	52
4.2	Radiation Pattern Measurement Issues	52
4.2.1	The Receiving System	53
4.2.2	The Positioning System	58
4.2.2.1	The Rotating Arm	58
4.2.2.2	The Precision DC Servo System	61
4.2.2.3	The Position Controller and Interface Electronics	63
4.2.3	The Recording and Data Processing Systems	65
4.3	The MMW QO Circuit	66
4.3.1	Circuit Description	66
4.3.1.1	Components and Configuration	66
4.3.1.2	Variation of the Source Aperture Position	69
4.3.1.3	Other Issues	71
4.3.2	QO Beam Parameters	73
4.3.2.1	Propagation of the Fundamental Mode Only	73
4.3.2.2	Multi-mode Propagation	74
4.4	System Evaluation	75
4.4.1	Dynamic Range and Angular Resolution	75
4.4.2	Standing Waves	76
4.4.3	Circuit Imposed Distortions	76
4.4.4	Source Aperture Position	78
	References	79
5	A Millimetre Wave Pyroelectric Detector	82
5.1	Introduction	82
5.2	Detector Description	83
5.2.1	The Pyroelectric Sensor	83

5.2.2	The Detector Housing	83
5.3	Performance	84
5.3.1	Measurement Approach	84
5.3.2	Measurement Results	84
5.4	Conclusion	89
	References	89
6	A Millimetre Wave Faraday Rotator	90
6.1	A MM-Wave Four-Port Quasi-Optical Circulator	90
6.1.1	Introduction	91
6.1.2	Circulator Description	92
6.1.2.1	Topology	92
6.1.2.2	Bandwidth	93
6.1.2.3	Materials	94
6.1.3	Circulator Performance	96
6.1.3.1	Definition of Performance Parameters	96
6.1.3.2	Measurement Results	98
6.1.4	Conclusion	105
6.1.5	Appendix I	107
6.1.6	Appendix II	108
6.2	The Performance of a Large Area Faraday Rotator	109
6.3	The Magnetic Field Strength within a Ferrite Disc	111
6.4	Reflection Properties in Detail	115
6.4.1	Introduction	115
6.4.2	A Transmission Line Model	115
6.4.2.1	The Equivalent Circuit	115
6.4.2.2	Polarisation Duality	119
6.4.3	Ferrite Reflectances	123
6.4.3.1	Unmagnetised Ferrite Sheet	123
6.4.3.2	Magnetised Ferrite Sheet	124
	References	126
7	SLM Pattern Evaluation	129
7.1	An SLM Pattern Model and Measurement	129

7.1.1	Gaussian Beam-Mode Model	130
7.1.2	Comparison with Measurement	133
7.2	Other SLM Configurations	138
7.2.1	An SLM with a Single $\lambda/4$ Step	139
7.2.2	Higher Order SLM Configurations	139
7.2.3	An SLM with a Single $\lambda/2$ Step	142
	References	144
	Epilogue	145
	A RADPAT : A Radiation Pattern Measurement Program	147
	B Multi-mode Propagation Through a Lens	162
	C FE1 : Modelling the Reflectance of a Ferrite Sheet	166
	D FE2 : Modelling the Reflectance of a Polarisation Active Ferrite Sheet	172
	E PSI13 : A Gaussian Beam-Mode Model	179

Chapter 1

Spatial Signal Processing at Millimetre Wavelengths

The invention of coherent optical sources¹ marked the beginning of a whole new era in optics, though at the outset it was not obvious how these new sources were to be employed, nor to what end. Longer wavelength coherent sources had been in use for some time and, for example, had been extensively exploited in radar and communications systems. It was from areas such as these, that ideas and inspiration were initially derived regarding possible concepts and techniques relevant to this new optical source, the laser. For example, the concept of spatial frequency was taken from communications theory just prior to the laser's advent, and was found to provide many rich insights and to have broad application to many of the new uses being found for the laser. However, this cross-discipline exchange appears to have waned with time. The reason for this is undoubtedly related to the large difference in wavelength—from 5 to 8 orders of magnitude—between the optics and longer wavelength régimes. The use of coherent sources within the optics régime has taken a distinctly different course from that of the longer wavelength coherent sources. Within the optics régime, emphasis has tended to be placed upon *spatial* signal processing methods, where holography and 2-dimensional Fourier transform correlators are good examples of this type of processing. With the longer wavelengths, emphasis has been placed on *temporal* signal processing methods such as inverse synthetic aperture radar (ISAR), which exploits sophisticated doppler processing for image formation.

¹Theodore H. Maiman built the first laser in July 1960.

Electromagnetic radiation at millimetre wavelengths is readily able to exploit concepts and techniques that are used in both of these régimes, because of its position mid-way between them in the electromagnetic spectrum, albeit with varying degrees of compromise. The kind of technology used for signal transport and processing at millimetre wavelengths is typically either waveguide based or quasi-optically based, or some hybrid of the two. It is the use of quasi-optical methods that opens up the possibility of applying some of the spatial signal processing methods that up to the present time have almost exclusively been used within the optics régime.² And so it has turned around; where once the radar and communications fields of knowledge *gave* to the optics researchers ideas and inspiration, it is now the radar and communications researchers turn to *take* from the optics field of knowledge, ideas and inspiration.

It is in the areas of radar and communications that millimetre wavelength technologies are most exploited by humankind, though perhaps the most mature area of exploitation is in radio-astronomy. It is with specific reference to **radar systems** operating at millimetre wavelengths, that the ideas explored within this thesis are directed.

Quasi-optical methods are primarily of relevance for wavelengths less than say 4 mm, that is, for frequencies above 75 GHz. Above this frequency, conventional wave-guiding systems suffer from severe losses and from narrow-bandedness due to mismatches with source and detector diodes. Also, extreme demands are put on machining and fabrication, which is expensive. Advantages are to be had in carrying out some signal transport and processing at the front end of a system, where the signal is still in the form of a free space beam, that is, a quasi-optical beam. For example, applications where this is so include:

- transporting signal beams to stationary receivers in steerable antennas;
- diplexing the signal and local oscillator beams for a heterodyne receiver;
- frequency multiplexing;
- polarisation analysis;
- beam shaping.

Also, for systems working at frequencies above 75 GHz, basic instruments such as spectrum analysers, reflectometers, and network analysers are required for the testing of

²There are some noteworthy exceptions that will be mentioned in the following chapter.

components and materials at these frequencies, and these may with distinct advantage be based on quasi-optical, rather than wave-guiding techniques.

It is primarily the opportunity that exists for signal processing to be carried out quasi-optically that is of particular relevance here to radar systems. From the earliest stages of radar development, signal processing has been an essential and integral part of that development, and has played an increasingly more significant role. One of the reasons why any optical signal processing is of special interest is because of the potential that exists for fast parallel processing exploiting the two-dimensional nature of a free space beam.

There are a large number of different applications for which radar systems have been developed, and of growing significance are those that involve some sort of target imaging and identifying function. *Temporal* waveform construction and analysis has played the most significant role in augmenting the basic radar functions (i.e. range finding and detection), to include these functions of target imaging and identification. However, direct access to the information contained within the *spatial* structure of reflected electromagnetic waves is impractical for most radars—which typically operate at wavelengths greater than a few centimetres—because any suitable spatial signal processing devices would be too large. For electromagnetic radiation at millimetre wavelengths the situation is different. The wavelength is sufficiently small for the realisation of suitable spatial signal processing devices and systems to be practical. The intention of this research effort, is to provide a sound basis for the future development of millimetre wavelength quasi-optical radar systems that process the information contained within the full *spatio-temporal* structure of electromagnetic waves scattered by radar targets.

A generic device that opens up this dimension of spatial signal processing to radar systems is at the heart of the work described within this thesis. The device could be suitably called a *millimetre wave quasi-optical spatial light modulator*, (i.e. a MMW QO SLM), and is identical in operation to the spatial light modulator used in many optical signal processing systems. Within this thesis both a theoretical and an experimental analysis of a specific millimetre wave quasi-optical spatial light modulator is undertaken. Thus represented here is an attempt to open up a whole new area of research and development to both the radar and opto-electronics research communities. It is an area that involves a heterogeneous mix of various technologies, and it is an area that is full of potential.

Of secondary significance in the present context, but still of relevance to the basic idea of spatial signal processing, is the work reported within this thesis concerning a high performance quasi-optical circulator or more simply a quasi-optical Faraday rotator. The polarisation state of a quasi-optical beam is the parameter most often exploited for signal processing applications in millimetre wave quasi-optical systems and thus a high performance polarisation rotator has found many opportunities for use in a wide variety of circumstances.

Before moving into a detailed analysis of the MMW QO SLM, it is valuable to have a grasp of both the immediate and wider contexts of the technology upon which the subsequent work is founded. The following chapter therefore seeks to provide these contexts.

Chapter 2

Millimetre Wave Technology

2.1 Millimetre Wave Optics

2.1.1 Theoretical Methodology

Electromagnetic waves are employed by humankind to perform many functions that are valued by society, such as surveillance, communications, astronomical observations, atmospheric observations and many others. The principles that these functions rely upon are not generally wavelength specific, but the *technology* used to carry out the functions, *does* depend on wavelength. Broadly speaking, there are three classes of technology for electromagnetic waves applications:

1. $\lambda \gg \ell$: guided-current methods are applicable;
2. $\lambda \sim \ell$: guided-wave methods are applicable;
3. $\lambda \ll \ell$: directed-wave methods are applicable.

In the above, λ is the wavelength of the electromagnetic waves and ℓ is a characteristic dimension of the technology employed, that is of the equipment or apparatus used to transmit, transfer, receive and process the electromagnetic radiation. There is some overlap between these three classes, and in fact millimetre wave quasi-optical technology requires analytical tools that relate to the region between the latter two classes, that is, where $\lambda < \ell$, but by less than say two orders of magnitude.

The theoretical methodology of prime relevance to this in-between region, is that of Gaussian beam-mode optics. Gaussian beam-mode optics originally was developed as a body of theory in response to the need to analyse confocal multimode resonators

for millimetre and optical wavelength masers[1]. A parallel development was provided for the analysis of beam waveguides[2]. An excellent tutorial paper summarising these early developments was provided by Kogelnik and Li[3]. Martin and Lesurf[4] related this earlier work to millimetre wave and submillimetre wave systems. Goldsmith[5] has also provided a summary of Gaussian beam-mode optics as applied to millimetre wave systems. Lesurf[6, 7] has applied Gaussian beam-mode optics to the design of millimetre wave Martin-Puplett instruments and two further helpful publications that describe the application of Gaussian beam-mode optics to different horn antenna situations are given by Wylde[8] and Torchinsky[9]. A recently published textbook[10] summarises millimetre wave quasi-optical theory together with a discussion on devices and systems. Significantly, a powerful, systematic and formalised technique for analysing millimetre wave quasi-optical *circuits* is also presented within this text. Marcuse[11] has provided a particularly comprehensive and insightful treatment of Gaussian beam-mode optics as it is applied to optical fibre communications.

Optical spatial signal processing techniques are covered within the body of theory called **Fourier optics**[12, 13]. Both Fourier optics and Gaussian beam-mode optics employ the *paraxial* or *Fresnel approximation*, and both of these theoretical approaches can be derived from the **angular spectrum of plane waves** description of a propagating electromagnetic wave[14, 15, 13, 16]. An understanding of this common foundation and connection is vital if quasi-optical spatial signal processing at millimetre wavelengths is to be explored in any detail, because concepts and techniques from both of these bodies of theory will need to be exploited. Chapter 3 of this thesis outlines and explores this connection.

2.1.2 MMW QO Devices and Systems

The range of instruments and systems that have been developed and which use MMW QO technology, is wide, and thus only a brief survey will be given here. Firstly, the desire to perform radio-astronomical observations in the millimetre and submillimetre wave bands has provided one of the major driving forces for the development of efficient quasi-optical systems[17]. Another strong driver has been the need for making precise materials measurements at millimetre and submillimetre wavelengths. Most notably, the technique of dispersive Fourier transform spectroscopy has been developed[18]. This technique is typically used for frequencies varying from about 100 GHz to more than

1 THz[19].

The Martin-Puplett interferometer[20], a polarising Michelson interferometer, has been used to make precise frequency and spectral measurements. This instrument is an important generic instrument which is quasi-optical by its very nature of operation. A millimetre wave quasi-optical reflectometer[21, 22] has been built which provides measurements with amplitude errors of around 0.05% and phase errors of around 0.1° . This instrument is a complex nulling reflection bridge with the nulling performed via polarising interferometry. A highly sensitive millimetre wave quasi-optical FM noise measurement system[23, 24] that exploits the very high Q cavities that are possible with this technology has also been constructed. It allows for the direct measurement of phase locked sources at low input power levels over ultra-wideband frequency ranges. A follow-on from this work has been the design and construction of cavity-stabilised oscillators[25] with ultra-low noise levels.

A continuous comparison radiometer operating at 97 GHz[26] has been developed using quasi-optical techniques for local oscillator injection and the realisation of a 90° hybrid. Major performance gains for this system were achieved through the use of quasi-optical techniques as opposed to the more commonly used waveguide components and techniques. Millimetre wave staring array[27] technology has also been developed. It uses multiple beams through lenses with a focal plane array of receivers with integral antennas to *stare* at a particular field of view. It has shown direction finding accuracy comparable to a monopulse radar.

A 225 GHz radar has been developed that has employed a quasi-optical duplexer, and that also provides for beam scanning optically[28]. A 94 GHz polarisation analysing FMCW radar[29] has been developed using quasi-optical technology, that provides for a continuous measure of the polarisation state of an elliptically polarised signal, as well as providing the opportunity for doppler processing to be performed. An especially interesting recent development for radar systems, is the emerging possibility of exploiting the commonly used laser technique of mode locking a source to produce high power RF pulses. There are a variety of ways to attempt this. One way is to use an array of oscillators[30] set at frequencies all offset from one another by a set amount, and have them phase locked together. Alternatively, a simpler quasi-optical approach could be taken, where a single oscillator is made to oscillate within a quasi-optical circuit and is biased in such a manner as to oscillate at a number of frequencies simultaneously[31].

A number of interesting devices have been reported recently that exploit a quasi-optical approach. A quasi-optical notch filter[32] which operates at 140 GHz has been constructed for use within a diagnostic system for the JET (Joint European Torus) nuclear fusion project. High- T_c superconductors have been used to construct a millimetre wave quasi-optical band-pass filter[33]. A quasi-optical Faraday rotator[34] that exhibits both high isolation and low insertion loss when used as a circulator has been developed. This device is described in detail within this thesis.

Antennas for use at millimetre wavelengths have also seen some interesting developments. A perforated plate quasi-optical lens[35] has been constructed that has the advantage of being practical in hostile environments (e.g. plasma diagnostics). A thorough treatment of Fresnel zone plate antennas[36] has been given. These zone plates have advantages over lenses and paraboloids that include reduced loss, weight, volume and cost, as well as simple planar construction. A recent colloquium[37] covered a number of aspects of millimetre wave quasi-optical antennas, including multiplexing issues, electrically large antenna measurements and various antenna analysis issues.

Finally, there are two spatial signal processing applications that deserve special attention. Firstly, computer generated phase holograms¹ (kinoforms) have been used in optics for some time, and recently a kinoform was designed and produced for use at 100 GHz[38]. This kinoform consisted of a PTFE plate with a computer generated surface profile milled onto it. It was in effect a transmission mode spatial light modulator. The particular kinoform reported was designed to convert an incident fundamental mode Gaussian beam into four spatially separated fundamental mode Gaussian beams. The purpose here could, for example, be distribution of a local oscillator. This kinoform basically worked as intended, however it also transmitted a large proportion of the original zeroth order beam. This may well have been due to manufacturing limitations. The computer generative process is iterative in nature and essentially derives the required two dimensional phase profile at a specific location that will, when convolved with the incident beam and Fourier transformed through a lens, produce the desired output beam profile. A quasi-optical description of the transformation process may give a better *a priori* understanding of the best approach for the application of this technology. The kinoform profiles produced by the above approach are *not* unique. Even so, this work has shown that a well understood optical technique can give re-

¹The following section will reference these *optical* devices.

sults at millimetre wavelengths that seem reasonable. A better understanding of the transformation processes within a quasi-optical setting may well provide a means for producing more effective and efficient kinoforms.

Secondly, spatial spectral estimation using multiple beam antennas[39] is a *form* of spatial signal processing that has been in use for some time at lower frequencies, typically in spaceborne scenarios. This particular application involves using an array of feeds at the focal plane of a lens and using the spatial layout of the feeds to provide a first order estimate of the location of a source in the antennas field of view, (i.e. like the staring array mentioned earlier). A more significant and widely exploited application is that of the satellite communications scenario where a particular spatial profile at the earth's surface is required. This kind of application has seen extensive research and development.

2.2 The Wider Context

In 1984, Wiltse provided an historical review[40] of the major events that have occurred in the development of millimetre and submillimetre wave technology from its beginnings in the 1890's, through to the 1980's. The value of an historical review such as this one, is that it enables research work such as that described here to be placed in a broad perspective. It enables one to see how this present work relates to the major thrusts of millimetre wave technological research and development from its beginnings up until the present point in time. But just as importantly, the contemporary setting for this research work needs to be understood, and this is provided within the following material. Again, this material is presented as a brief survey only. The whole area of research and development on MMW sources and detectors is vast and reference[10] provides a suitable introduction to this area.

2.2.1 Surveillance Technologies

There are many purposes for which the *surveillance* function is central. There are also many technological approaches to performing surveillance tasks, not all of which employ electromagnetic waves. Those approaches that are most relevant, and thus particularly worth mentioning here, are microwave and millimetre wave *radar* and microwave and millimetre wave *radiometry*. Radar systems have many military and civilian applica-

tions, such as airborne target detection, ship detection and space object detection[41]. Mere *detection* is rarely all that is required from a surveillance system. Typically additional information is required, such as positional and velocity information. Also, signal processing for target imaging and/or identification is often desired, and many techniques have been developed that attempt to provide this sort of information. The techniques most commonly exploited for this identifying function are invariably temporal signal processing techniques. However, there are two further interesting recent developments worth mentioning here. Firstly, *fractal* geometry techniques have been applied to the radar stationary target detection problem[42] and promising results have been obtained. A fractal dimension (i.e. a number) is evaluated for a given set of range profile data, within which a target may exist. A fractal dimension close to an integer value indicates the presence of reflections from an object with Euclidean geometry. This is interpreted as meaning that there is a man-made object within the data. If this technique is coupled with say a CFAR (constant false alarm rate) technique, then the probability of detection for a given false alarm rate is increased. This is so because the two techniques are in fact independent from one another. Secondly, radar polarimetry which involves using the additional dimension of polarisation diversity to provide another parameter for clarifying a target's identity, is theoretically well established[43] and experimentally is seeing increasing activity[44].

Two interesting radar developments are also mentioned here, as they give an indication of some of the current trends in millimetre wave radar research and development. A 94 GHz bistatic FMCW radar for imaging runways from aircraft during conditions of low or zero visibility, is currently under development[45]. A detection and tracking system that combines the differing advantages of a radar (35 GHz) and a ladar (Nd:YAG pulsed laser) together in one system has also been described[46].

Millimetre wave radiometry provides a means for covert battlefield surveillance through smoke, dust or fog—see section 2.2.5—and similarly for space-borne surveillance of surface targets or fast moving targets against clutter. Millimetre wave radiometry has enabled high altitude storm research to be carried out[47]. Forward-looking imagery for aircraft landing is one further application for millimetre wave radiometry.

Knowledge of the reflectivity of targets, vegetation and other objects typically illuminated by millimetre wave radiation—either from a radar or from the cosmic background radiation—is of prime importance to all millimetre wave surveillance systems.

There have been several major measurement programs organised for the collection of radar backscatter data from various types of ground clutter[48]. Whilst more measurements are still needed, the amount of data available now is large and well documented, and should provide a useful basis for the development of systems. In addition, a millimetre wave radar cross section range for the characterisation of targets has been developed[49].

2.2.2 Planar Grids

A recent development within the literature has been the description of a number of planar grid devices. They are mentioned explicitly here because of their potential for use within quasi-optical systems. One motivation has been the increasing demand for watt-level coherent sources in the millimetre and submillimetre wave region. Watt-level power outputs have been obtained in doubling to 66 GHz[50]. Various approaches have been described for millimetre wave generation using solid-state and vacuum microelectronics arrays[51]. An impedance model for these quasi-optical diode arrays has been developed[52] that is based on a simple unit-cell approach. A number of lower frequency models of possible millimetre wave grids has been developed and include: a grid amplifier[53]; a planar MESFET grid oscillator that uses gate feedback[54]; and a 100-element planar Schottky diode grid mixer[55].

2.2.3 Mode Converters

Gyrotron sources produce output power beams that are decidedly not fundamental mode Gaussian beams. The applications that gyrotrons are typically put to require a beam that is essentially a fundamental mode Gaussian beam. To convert the so-called whispering gallery modes normally produced within a gyrotron to fundamental mode beams involves the design of high efficiency *mode converters*. These are related in many ways to the millimetre wave quasi-optical spatial light modulator described within this thesis. A particularly efficient converter called MAGICTRAC has recently been reported[56]. Calculated conversion efficiencies of 96% have been achieved for the conversion of a $TE_{15,2}$ mode at 140 GHz to a fundamental mode beam. Vlasov[57, 58] antenna type converters are also commonly exploited.

2.2.4 Optical Signal Processing

Optical signal processing covers many different areas of application, from optical computing through to imaging and correlation work. A recent review by Flannery and Horner[59] on Fourier optical signal processors included a relevant and useful discussion on 2D correlators, in which spatial light modulators were used as spatial filters. References[60]–[69] deal with various aspects of spatial filter design as it relates primarily to pattern recognition. The differing advantages and disadvantages of *phase-only* and *binary phase-only* filters compared to matched filters is described. These issues would be of importance to the next stage of development of the work presented within this thesis. A tutorial paper on spatial light modulators[70] published recently, looks at the various types of spatial light modulators that have been developed and also describes alternative approaches to their design.

Optical kinoforms[71] are computer-generated wavefront reconstruction devices that, like the hologram, provide displays of three-dimensional images. Refinements on the original design approaches have been developed that produce more robust kinoforms[72]. Reference[73] describes a practical iterative algorithm for the determination of the phase transformations required for given image and diffraction plane pictures.

Finally, under this heading, reference[74] discusses the very issue that is the motivation for this thesis but as it relates to *IR sensor technology* and *Fourier optics* analysis. A number of insights and system considerations are provided within this paper that would be relevant to any millimetre wave based system.

2.2.5 MMW Propagation in the Atmosphere

Most radar applications require as great a detection range as possible, and thus radar research and development has been concentrated in the areas of low atmosphere attenuation, that is, at the MMW window frequencies of 35 GHz, 94 GHz, 140 GHz and 220 GHz[75]. Very little radar development has occurred above 220 GHz. Water vapour and oxygen molecule electromagnetic interaction resonances provide regions of abnormally large absorption which are approximately at the frequencies 60 GHz, 120 GHz and 180 GHz. Radars have been developed at these frequencies that take advantage of the potential for covert operation possible because of absorption. These absorption bands also provide terrestrial isolation for systems operating in exoatmospheric space. Compared to IR imaging systems, MMW systems perform better under

adverse weather conditions (i.e. rain, fog, etc.), because of the reduced absorption and scattering involved.

Millimetre wave propagation within clear[76] and turbid[77] atmospheres has also been explored theoretically. Recently, complete analytic expressions for temporal power spectral functions in a millimetric wave absorption region for plane and spherical waves have been developed for both amplitude and phase fluctuations due to atmospheric turbulence[78]. These expressions correlate well with experimental data.

2.2.6 Material Properties and Measurement Techniques

The important technique of dispersive Fourier transform spectroscopy has already been mentioned. A summary of relevant measurement techniques has been provided by Asfar and Button[79]. Materials that are of particular importance to millimetre wave quasi-optical systems are those that are used for lenses, quarter-wave matching, beam-splitting and those materials that are used in the making of detectors and sources. A number of PTFE loaded materials have been characterised[80, 81, 82]. A set of measurements² made recently reveal that a number of different compounds may have properties useful at millimetre wavelengths. One promising possibility that comes out of these measurements is the possibility of producing a PTFE glass-fibre loaded material with a refractive index to specification, (i.e. somewhere between the refractive index of PTFE and that of the glass fibres being used). Non-linear materials[83] are also of importance. Spatial light modulators could be produced that operate in a transmission mode, providing controllable phase delays across an aperture. This could be achieved by changing the properties of the material locally with for example, an applied static electric field in the case where the Kerr effect is being exploited. Liquid crystals are already used for optical spatial light modulators and new possibilities for these kinds of materials[84] are the focus of much current materials research. Ferroelectric liquid crystals[85] offer the potential for very fast switching for optical systems.

2.2.7 E-Plane Integrated Circuits

There are a number of planar and quasi-planar transmission media that have been studied, with perhaps the most significant structures being *E-Plane* structures or *fin-lines*. Reference[86] provides an excellent survey and summary of this whole field

²M. R. Webb and J. R. Birch (NPL, Teddington.)

of research. The prime advantage gained from using E-plane technology rather than waveguide or QO technology, is that integrated circuit fabrication techniques can be used in the production of otherwise difficult-to-make components. In the long-term this is a low-cost approach (i.e. for the mass market). E-plane technology is not seen as being particularly relevant in the context of this thesis, and is mentioned here only because of its growing significance for many other millimetre wave system applications.

2.2.8 Communications

Wiltse[87] has briefly summarised the development of MMW communications systems. Both terrestrial and satellite systems have seen extensive activity. Terrestrial systems generally fall into one of two categories, viz. short-range point-to-point links, or enclosed, low-loss, circular waveguide for use in wide-band, long-haul, heavy route communication systems. For the point-to-point systems, the carrier frequency can be chosen to have low atmospheric attenuation (e.g. 35 GHz) or for security reasons, high atmospheric attenuation (e.g. 60 GHz). A number of inherent advantages are available from millimetre wave systems, such as, wide bandwidth, link privacy and reduced interference by virtue of the narrow beamwidths possible, as well as the low density of other radio and radar users in this band.

2.2.9 Radioastronomy

The importance of this field of research to millimetre wave quasi-optical systems has already been stated. Reference[17] is a good review of the whole field, though significant advances have been made since this reference was first published. A review of millimetre and submillimetre wavelength radio astronomy by Payne[88] includes a discussion on the James Clerk Maxwell Telescope (JCMT), situated in Hawaii. This telescope represents the state-of-the-art in instruments for millimetre wave radioastronomy. Both the antenna and the receiver technology are discussed in some detail. Millimetre waves are of special interest to astronomers because their existence in any observed spectral measurements provide unique keys to the understanding of various phenomena such as molecular clouds and star formation.

References

- [1] G. D. Boyd and J. P. Gordan, "Confocal Multimode Resonator for Millimeter Through Optical Wavelength Masers," *The Bell System Tech. Journal*, pp. 489–508, March 1961.
- [2] G. Goubau and F. Schwing, "On the Guided Propagation of Electromagnetic Wave Beams," *IRE Trans. on Antennas and Propagation*, pp. 248–256, May 1961.
- [3] H. Kogelnik and T. Li, "Laser Beams and Resonators," *Proceedings of the IEEE*, vol. 54, no. 10, pp. 1312–1329, 1966.
- [4] D. H. Martin and J. C. G. Lesurf, "Submillimetre-wave Optics," *Infrared Physics*, vol. 18, pp. 405–412, 1978.
- [5] P. F. Goldsmith, *Infrared and Millimeter Waves—Vol. 6*. Academic Press, 1982, chapter 5.
- [6] J. C. G. Lesurf, "Gaussian Optics and the Design of Martin-Puplett Diplexers," *Infrared Physics*, vol. 21, pp. 383–390, 1981.
- [7] J. C. G. Lesurf, "Gaussian Beam-mode Optics and the Design of Millimetre-wave Martin-Puplett Instruments," *Infrared Physics*, vol. 28, pp. 129–137, 1988.
- [8] R. J. Wylde, "Gaussian beam-mode optics and corrugated feed horns," *IEE Proceedings*, vol. 131, pt. H, no. 4, pp. 258–262, 1984.
- [9] S. A. Torchinsky, "Analysis of a Conical Horn Fed by a Slightly Oversized Waveguide," *International Journal of Infrared and Millimeter Waves*, vol. 11, pp. 791–808, 1990.
- [10] J. C. G. Lesurf, *Millimetre-wave Optics, Devices and Systems*. Adam Hilger, 1990.
- [11] D. Marcuse, *Light Transmission Optics 2nd ed*. Van Nostrand Reinhold Company, 1982, chapters 4–6.
- [12] E. G. Steward, *Fourier Optics - an introduction 2nd ed*. Ellis Horwood Limited, 1987.
- [13] J. W. Goodman, *Introduction to Fourier Optics*. McGraw-Hill Book Company, 1968.

- [14] H. G. Booker and P. C. Clemmow, "The Concept of an Angular Spectrum of Plane Waves, and it's relation to that of Polar Diagram and Aperture Distribution," *Proceedings IEE London*, vol. 97(3), pp. 11–17, 1950.
- [15] P. C. Clemmow, *The Plane Wave Spectrum Representation of Electromagnetic Fields*. International Series of Monographs in Electromagnetic Waves, Editors: A. L. Cullen, V. A. Fock and J. R. Wait; Volume 12; Pergamon Press, 1966.
- [16] D. H. Martin, "Gaussian Beam-Mode Analysis of Paraxial Propagation," Lecture 4 of a course held at Queen Mary & Westfield College, University of London, 1980.
- [17] J. E. Beckman and J. P. Philips, eds. *Submillimetre Wave Astronomy*. Cambridge University Press, 1982.
- [18] J. R. Birch and T. J. Parker, *Infrared and Millimeter Waves—Vol. 2*. Academic Press, 1979.
- [19] G. J. Simonis, "Index to the Literature Dealing with the Near-Millimeter Wave Properties of Materials," *International Journal of Infrared and Millimeter Waves*, vol. 3, 1982.
- [20] D. H. Martin and E. Puplett, "Polarised Interferometric Spectrometry for the Millimetre and Submillimetre Spectrum," *Infrared Physics*, vol. 10, pp. 105–109, 1969.
- [21] A. R. Harvey, *PhD Thesis*. University of St. Andrews, 1990.
- [22] A. R. Harvey and J. C. G. Lesurf, "A millimetre wave, single mode, quasi-optical, complex reflectometer operating as a nulling bridge," *SPIE Fifteenth International Conference on Infrared and Millimeter Waves, Orlando*, vol. 1514, pp. 198–200, December 1990.
- [23] G. M. Smith, *PhD Thesis*. University of St. Andrews, 1990.
- [24] G. M. Smith and J. C. G. Lesurf, "A Highly Sensitive Millimeter Wave Quasi-Optical FM Noise Measurement System," *IEEE Trans. Microwave Theory Tech.*, vol. 39, pp. 2229–2236, 1991.
- [25] G. M. Smith, *Private Communication*. 1992.

- [26] C. R. Predmore, N. R. Erickson, G. R. Huguenin and P. F. Goldsmith, "A Continuous Comparison Radiometer at 97 GHz," *IEEE Trans. Microwave Theory Tech.*, vol. 33, 1985.
- [27] C. J. Alder *et al*, "Microwave and Millimetre-Wave Staring Array Technology," *IEEE Microwave Theory Tech. Symposium Digest*, pp. 1249–1252, 1991.
- [28] C. W. Trussell, R. W. McMillan, R. E. Forsythe and R. A. Bohlander, "225 GHz Radar System," *IEEE 6th International Conference on Infrared and Millimeter Waves*, 1981.
- [29] M. J. Leeson, *PhD Thesis*. In press, University of St. Andrews, 1992.
- [30] R. A. York and R. C. Compton, "Mode-Locked Oscillator Arrays," *IEEE Microwave and Guided Wave Letters*, vol. 1, pp. 215–218, 1991.
- [31] G. M. Smith, *Private Communication*.
- [32] A. R. Harvey, "A 140 GHz Quasi-Optical Notch Filter," *SPIE Sixteenth International Conference on Infrared and Millimeter Waves, Lausanne*, vol. 1576, pp. 358–359, August 1991.
- [33] D. Zhang *et al*, "Quasi-Optical Millimeter-Wave Band-Pass Filters Using High- T_c Superconductors," *IEEE Trans. Microwave Theory Tech.*, vol. 39, pp. 1493–1497, 1991.
- [34] M. R. Webb, "A MM-Wave Four-Port Quasi-Optical Circulator," *International Journal of Infrared and Millimeter Waves*, vol. 12, pp. 45–63, 1991.
- [35] P. F. Goldsmith, "Perforated Plate Lens for Millimeter Quasi-Optical Systems," *IEEE Trans. Antennas Prop.*, vol. 39, pp. 834–838, 1991.
- [36] J. E. Garrett and J. C. Wiltse, "Fresnel Zone Plate Antennas at Millimeter Wavelengths," *International Journal of Infrared and Millimeter Waves*, vol. 12, pp. 195–220, 1991.
- [37] IEE Electronics Division Colloquium, *Millimetre-Wave and Quasi-Optical Antennas*. June 1990.

- [38] S. Jacobsson, A. Lundgren and J. Johansson, "Computer Generated Phase Holograms (Kinoforms) for Millimeter and Submillimeter Wavelengths," *International Journal of Infrared and Millimeter Waves*, vol. 11, pp. 1251–1261, 1990.
- [39] J. T. Mayhen and L. Niro, "Spatial Spectral Estimation Using Multiple Beam Antennas," *IEEE Antennas Prop.*, vol. 35, 1987.
- [40] J. C. Wiltse, "History of Millimeter and Submillimeter-Waves," *IEEE Microwave Theory Tech.*, vol. 32, 1984.
- [41] K. Chang *et al*, "System Feasibility Study of a Microwave/Millimeter-Wave Radar for Space Debris Tracking," *International Journal of Infrared and Millimeter Waves*, vol. 10, 1989.
- [42] J. I. Butterfield, "Fractal Interpolation of Radar Signatures for Detecting Stationary Targets in Ground Clutter," *IEEE Aerospace and Electronic SYSTEMS Magazine*, vol. 6, pp. 10–14, July 1991.
- [43] H. A. Zebker and J. J. van Zyl, "Imaging Radar Polarimetry: A Review," *IEEE Proc.*, vol. 79, pp. 1583–1606, 1991.
- [44] J. B. Mead *et al*, "Polarimetric Scattering from Natural Surfaces at 225 GHz," *IEEE Trans. Antennas Prop.*, vol. 39, pp. 1405–1411, 1991.
- [45] L. Q. Bui and A. T. Morton, "94 GHz FMCW Radar for Low Visibility Aircraft Landing System," *IEEE Microwave Theory Tech. Symposium Digest*, pp. 1147–1150, 1991.
- [46] J. Gavan and A. Peled, "Optimized LADAR/RADAR System for Detection and Tracking," *International Journal of Infrared and Millimeter Waves*, vol. 12, p. 1143, 1991.
- [47] T. P. Morton *et al*, "Millimeter Wave Radiometry," *SPIE Millimeter Wave Technology*, vol. 337, 1982.
- [48] T. L. Lane, C. R. Scheer and N. C. Currie, "An Overview of MMW Radar Reflectivity," *IEEE National Radar Conference*, 1988.
- [49] J. A. Scheer *et al*, "MMW Radar Cross Section Range Characterises Targets," *IEEE National Radar Conference*, 1988.

- [50] C. F. Jou *et al*, "Millimeter-wave monolithic Schottky diode-grid frequency doublers," *IEEE Trans. Microwave Theory Tech.*, vol. 36, pp. 1507–1514, 1988.
- [51] R. J. Hwu *et al*, "Array Concepts for Solid-State and Vacuum Microelectronics Millimeter-Wave Generation," *IEEE Trans. Electron Devices*, vol. 36, pp. 2645–2649, 1989.
- [52] L. B. Sjoren and N. C. Luhmann, Jr., "An Impedance Model for the Quasi-Optical Diode Array," *IEEE Microwave and Guided Wave Letters*, vol. 1, pp. 297–299, 1991.
- [53] M. Kim *et al*, "A Grid Amplifier," *IEEE Microwave and Guided Wave Letters*, vol. 1, pp. 322–324, 1991.
- [54] R. M. Wiekke *et al*, "Planar MESFET Grid Oscillators using Gate Feedback," Submitted to the *IEEE Trans. Microwave Theory Tech.*, August 1991.
- [55] J. B. Hacker *et al*, "A 100-Element Planar Schottky Diode Grid Mixer," Submitted to the *IEEE Trans. Microwave Theory Tech.*, July 1991.
- [56] B. W. Stallard, J. A. Byers and M. A. Makowski, "MAGICTRAC, A Novel Method for Conversion of Whispering-Gallery Modes into a Free-Space Gaussian-Like Beam," *International Journal of Infrared and Millimeter Waves*, vol. 11, pp. 1011–1032, 1990.
- [57] S. N. Vlasov and I. M. Orlova, "Quasioptical Transformer which Transforms the Waves in a Waveguide having a Circular Cross Section into a Highly Directional Wave Beam," *Scientific-Research Radio-Physics Institute. Translated from Izvestiya Vysshikh Uchebnykh Zavedennii, Radiofizika*, vol. 17, no. 1, pp. 148–154, January 1974, pp. 115–119, 1974.
- [58] P. R. Winning, S. N. Spark and A. D. R. Phelps, "Quasi-Optical Mode Converter for K_a-Band Application on a Gyrotron," *International Journal of Infrared and Millimeter Waves*, vol. 12, pp. 629–648, 1991.
- [59] D. L. Flannery and J. L. Horner, "Fourier Optical Signal Processors," *IEEE Proceedings*, vol. 77, no. 10, 1989.

- [60] Q. Tang, B. Javidi, E. Jäger and T. Tschudi, "Design of Binary Phase-Only Filters Implemented with Computer-Generated Holograms," *Optics Communications*, vol. 87, pp. 87–92, 1992.
- [61] Ph. Refregier, "Optical Pattern Recognition: optimal trade-off circular harmonic filters," *Optics Communications*, vol. 86, pp. 113–118, 1991.
- [62] H. Yamazaki and M. Yamaguchi, " 4×4 free-space optical switching using real-time binary phase-only holograms generated by a liquid-crystal display," *Optics Letters*, vol. 16, pp. 1415–1417, 1991.
- [63] F. M. Dickey and L. A. Romero, "Normalized correlation for pattern recognition," *Optics Letters*, vol. 16, pp. 1186–1188, 1991.
- [64] B. V. K. Vijaya Kumar and R. D. Juday, "Design of phase-only, binary phase-only, and complex ternary matched filters with increased signal-to-noise ratios for colored noise," *Optics Letters*, vol. 16, pp. 1025–1027, 1991.
- [65] Ph. Refregier, "Optimal trade-off filters for noise robustness, sharpness of the correlation peak, and Horner efficiency," *Optics Letters*, vol. 16, pp. 829–831, 1991.
- [66] B. Javidi and J. Wang, "Binary nonlinear joint transform correlation with median and subset median thresholding," *Applied Optics*, vol. 30, pp. 967–976, 1991.
- [67] L. A. Romero and F. M. Dickey, "Comparison between the peak-to-sidelobe ratio of the matched and phase-only filters," *Optics Letters*, vol. 16, pp. 253–254, 1991.
- [68] T. H. Barnes *et al*, "The application of phase-only filters to optical interconnects and pattern recognition," *Journal of Modern Optics*, vol. 37, pp. 1849–1863, 1990.
- [69] H. Bartelt, *Optical Signal Processing*. Editor: J. L. Horner, Academic Press, 1987, chapter 2.2.
- [70] J. A. Neff, R. A. Athale and S. H. Lee, "Two-Dimensional Spatial Light Modulators : A Tutorial," *IEEE Proceedings*, vol. 78, no.5, 1990.
- [71] L. B. Lesem, P. M. Hirsch and J. A. Jordan, Jr., "The Kinoform: A New Wavefront Reconstruction Device," *IBM J. Res. Develop.*, vol. 13, pp. 150–155, 1969.
- [72] S. Jacobsson, S. Hard and A. Bolle, "Partially illuminated kinoforms: a computer study," vol. 26, pp. 2773–2781, 1987.

- [73] R. W. Gerchberg and W. O. Saxton, "A Practical Algorithm for the Determination of Phase from Image and Diffraction Plane Pictures," *OPTIK*, vol. 35, pp. 237–246, 1972.
- [74] D. N. Kato, R. D. Holben, A. S. Politopoulos and B. H. Yin, "Ship Classification and Aimpoint Maintenance," *SPIE Infrared Systems and Components II*, vol. 890, 1988.
- [75] E. K. Reedy, *Principles and Applications of Millimeter-Wave Radar*. Editors: N. C. Currie and C. E. Brown, Artech House, 1987, chapter 2.
- [76] R. M. Manning, F. L. Merat and P. C. Claspy, "Theoretical investigation of millimeter wave propagation through a clear atmosphere," *SPIE Millimeter Wave Technology*, vol. 337, pp. 67–80, 1982.
- [77] F. L. Merat, P. C. Claspy and R. M. Manning, "Characterization of millimeter wave propagation through a turbid atmosphere," *SPIE Proceedings Optical Engineering for Cold Environments*, vol. 414, pp. 126–134, 1983.
- [78] G. L. Siqueira and R. S. Cole, "Temporal-Frequency Spectra for Plane and Spherical Waves in a Millimetric Wave Absorption Band," *IEEE Antennas Prop.*, vol. 39, pp. 229–235, 1991.
- [79] M. N. Asfar and K. J. Button, "Precise Millimeter Wave Measurements of Complex Refractive Index, Complex Dielectric Permittivity and Loss Tangent," *IEEE Instrumentation and Measurement Conference Proceedings*, 1984.
- [80] J. R. Birch, J. D. Dromey and J. C. G. Lesurf, "The Optical Constants of Some Low-loss Polymers Between 4 and 40 cm^{-1} ," *Infrared Physics*, vol. 21, pp. 225–228, 1981.
- [81] J. R. Birch and J. C. G. Lesurf, "The Near Millimetre Wavelength Optical Constants of Fluorosint," *Infrared Physics*, vol. 27, pp. 423–424, 1987.
- [82] P. B. Whibberley and J. R. Birch, "The Temperature Variation of the Near-mm Wavelength Optical Constants of Fluorosint," *Infrared Physics*, vol. 29, pp. 995–996, 1989.
- [83] R. McGraw, D. N. Rogovin *et al*, "Nonlinear Response of a Suspension Medium to Millimeter-Wavelength Radiation," *Physical Review Letters*, vol. 61, 1988.

- [84] G. Attard and C. Imrie, "Plastics of a new order," *New Scientist*, pp. 38–43, 11 May 1991.
- [85] C. R. Lavers *et al*, "Optical mode characterization of the configuration of a thin ferroelectric liquid crystal cell under an applied electric field," *Journal of Modern Optics*, vol. 38, pp. 1451–1461, 1991.
- [86] P. Bhartia and P. Pramanick eds., *E-Plane Integrated Circuits*. Artech House, 1987.
- [87] J. C. Wiltse, "Development of Terrestrial Millimeter-Wave Communications," *Eighth International Conference on Infrared and Millimeter Waves*, 1983.
- [88] J. M. Payne, "Millimeter and Submillimeter Wavelength Radio Astronomy" *IEEE Proceedings*, vol. 77, no. 7, 1989.

Chapter 3

SLM Pattern Analysis

A spatial light modulator (SLM) is a device capable of modifying the amplitude (or intensity), phase or polarisation of an electromagnetic wavefront as a function of the two spatial dimensions transverse to the wavefront's direction of propagation. The theoretical approach developed within this chapter seeks to provide a method for analysing of the wavefront modifying function of a MMW QO SLM within the constraints imposed by real MMW QO systems. The chief constraint to be considered is that of the finite diameters of the various components that comprise MMW QO systems (e.g. lenses, polarisers, Faraday rotators, SLMs, etc.). The apertures through which the MMW QO beams must propagate modify the beams. These effects are normally minimised within MMW QO systems by an appropriate choice of the beam size and form. Typically fundamental mode Gaussian beams are used and their size is chosen according to some aperture related criterion[1]. However, a MMW QO SLM deliberately modifies this optimally formed fundamental mode Gaussian beam, and so the aperture effects need further consideration.

The analytical approach developed within this chapter is based upon Gaussian beam-mode optics. Theoretical results for a specific SLM configuration are compared with experimentally derived results in chapter 7. Fourier optics offers an alternative approach, and the essence of it's relationship to Gaussian beam-mode optics is briefly discussed within the closing sections of this chapter. Common roots exist for these two approaches within the angular spectrum of plane waves description of a propagating electromagnetic wave and an outline of this common foundation and connection now follows.

3.1 The Angular Spectrum of Plane Waves

Throughout this development, electromagnetic radiation is treated as a scalar phenomenon. This means that only the scalar amplitude of one transverse component of either the electric or magnetic field is considered, it being assumed that any other component of interest can be treated independently in a similar fashion. This assumption greatly simplifies the analysis. With this assumption, it is well known that Maxwell's equations for a time-harmonic field within a source-free region of an isotropic homogeneous medium, lead to the scalar Helmholtz wave equation

$$\nabla^2\psi + k^2\psi = 0 \quad (3.1)$$

where $k = \omega\sqrt{\epsilon\epsilon_0\mu\mu_0}$ is a constant for the medium¹ and ψ is any of the Cartesian components of the vector fields \mathbf{E}, \mathbf{H} ; (ψ is complex with the time-dependent factor $e^{j\omega t}$ suppressed, i.e. ψ is a phasor).

This scalar theory yields very accurate results if three conditions are met[2]:

1. Any aperture where diffraction takes place must be large compared with a wavelength.
2. The diffracted fields must not be observed too close to the aperture.
3. Any transformation of the propagating wavefront (e.g. by a lens) must not cause too rapid a change of ψ in the direction of propagation. For example, significant longitudinal components of the propagating electromagnetic wave would exist within the focal region of a beam, if the beam was made to converge to a focus (i.e. beam waist) too rapidly.

Martin and Jones[3] have examined the relationship between solutions of the scalar and vector wave equations. They have shown that for the case of paraxial propagation, solutions to the scalar wave equation provide accurate results. They have also shown that the corresponding solutions to the vector wave equation can be found by applying small correction factors to the solutions of the scalar wave equation. These correction factors are in fact small components along the direction of propagation.

¹Within free space, $k = \omega/c = 2\pi/\lambda$, where $c = 299.79 \text{ Mms}^{-1}$ is the speed of light in a vacuum.

The Angular Spectrum

The essential elements to this concept of an angular spectrum of plane waves can be stated in words as follows: if the complex field distribution across any plane is Fourier analysed, the various spatial Fourier components can be identified as plane waves travelling in different directions. The field amplitude at any point can be calculated by adding the contributions of these plane waves, taking into account the differing phase-shifts associated with their propagation to the point in question. The following development follows Goodman's[4, §3.7].

Consider the situation where a monochromatic electromagnetic wave is incident upon the xy plane, and is travelling in the positive z -direction. Let the complex field across the xy plane be represented by $\psi(x, y, 0)$. The purpose is to find $\psi(x, y, z)$, (i.e. ψ for $z > 0$), given that $\psi(x, y, 0)$ is known.

The two-dimensional inverse Fourier transform of $\psi(x, y, 0)$ is given by

$$A_o(k_x, k_y) = \frac{1}{(2\pi)^2} \iint_{-\infty}^{\infty} \psi(x, y, 0) e^{j(k_x x + k_y y)} dx dy \quad (3.2)$$

where $k_{x,y} = 2\pi f_{x,y}$ and $f_{x,y}$ are the spatial frequencies in the two directions orthogonal to the direction of propagation. The forward Fourier transform is

$$\psi(x, y, 0) = \iint_{-\infty}^{\infty} A_o(k_x, k_y) e^{-j(k_x x + k_y y)} dk_x dk_y \quad (3.3)$$

Recall that the Fourier transform operation may be regarded as a decomposition of a complicated function into a collection of simple complex-exponential functions. Consider the form of the expression that describes a propagating plane wave of unit amplitude, viz.

$$e^{-j\mathbf{k}\mathbf{n}\cdot\mathbf{r}} \quad (3.4)$$

where $k = 2\pi/\lambda$ is the propagation constant, \mathbf{n} is the unit vector in the direction of propagation,² and \mathbf{r} is the position vector for the observation point $P(x, y, z)$. Expression 3.4 is in fact a solution of the scalar Helmholtz wave equation 3.1. Thus across the plane $z = 0$, the complex-exponential function $e^{-j(k_x x + k_y y)}$, as found in equation 3.3, may be regarded as a plane wave propagating with a direction given by \mathbf{n} where

$$\mathbf{n} = \frac{\mathbf{k}}{k}, \quad \mathbf{k} = (k_x, k_y, k_z) \quad (3.5)$$

²It is assumed here that \mathbf{n} is real, that is, that the plane wave is *homogenous*. By homogenous it is meant that the equi-phase and equi-amplitude planes are coincident. The components of \mathbf{n} are in fact direction cosines.

or

$$n_x = \frac{k_x}{k} \quad n_y = \frac{k_y}{k} \quad n_z = \left(1 - \left(\frac{k_x}{k}\right)^2 - \left(\frac{k_y}{k}\right)^2\right)^{\frac{1}{2}} \quad (3.6)$$

and with a complex amplitude $A_o(k_x, k_y) dk_x dk_y$ evaluated at (k_x, k_y) . Hence, by integrating over all directions—all (k_x, k_y) — $A_o(k_x, k_y)$ can be considered to be the *angular spectrum* of $\psi(x, y, 0)$.

Consider now the angular spectrum of $\psi(x, y, z)$ in a plane parallel to the xy plane. Let $A(k_x, k_y; z)$ represent this angular spectrum. Thus

$$A(k_x, k_y; z) = \frac{1}{(2\pi)^2} \int \int_{-\infty}^{\infty} \psi(x, y, z) e^{j(k_x x + k_y y)} dx dy \quad (3.7)$$

If the relationship between $A_o(k_x, k_y)$ and $A(k_x, k_y; z)$ can be found, then $\psi(x, y, z)$ would be able to be determined from knowledge of $\psi(x, y, 0)$. The Fourier transform for this case is

$$\psi(x, y, z) = \int \int_{-\infty}^{\infty} A(k_x, k_y; z) e^{-j(k_x x + k_y y)} dk_x dk_y \quad (3.8)$$

Now $\psi(x, y, z)$ must satisfy the scalar Helmholtz wave equation 3.1. By substitution, it can be shown that $A(k_x, k_y; z)$ must satisfy the following differential equation (and with the aid of Leibniz's Theorem[5, §3.3.7, p.11])

$$\frac{d^2}{dz^2} A(k_x, k_y; z) + (k^2 - k_x^2 - k_y^2) A(k_x, k_y; z) = 0 \quad (3.9)$$

A solution for this equation can be written in the following form

$$A(k_x, k_y; z) = A_o(k_x, k_y) e^{-jk_z z} \quad (3.10)$$

where from equation 3.6

$$\begin{aligned} k_z &= \sqrt{k^2 - k_x^2 - k_y^2} \\ &= k n_z \\ &= k \sqrt{1 - (k_x^2 + k_y^2)/k^2} \end{aligned} \quad (3.11)$$

Note that if

$$k_x^2 + k_y^2 < k^2 \quad (3.12)$$

then the effect of propagating over a distance z is simply a change in the relative phases of the various components of the angular spectrum. That is, each plane wave component propagates at a different angle, and so each travels a different distance to

reach a given observation point and relative phase delays are thus introduced. However, if

$$k_x^2 + k_y^2 > k^2 \quad (3.13)$$

then evanescent waves are produced. For this case the scalar theory itself is suspect because condition 2 on page 28 would now be violated. This is because evanescent waves are rapidly attenuated and so if their character were to be explored using the scalar theory, the fields would have to be examined too close to the plane in which they originate. If paraxial propagation is being considered, then this condition is of no interest and is in fact disallowed.

Hence for a given field distribution in the xy plane, $\psi(x, y, 0)$ and its associated angular spectrum $A_o(k_x, k_y)$, the field that propagates into $z > 0$ can be described by the Fourier transform

$$\begin{aligned} \psi(x, y, z) &= \iint_{-\infty}^{\infty} A_o(k_x, k_y) e^{-jk\sqrt{1-\frac{k_x^2+k_y^2}{k^2}}z} e^{-j(k_x x + k_y y)} dk_x dk_y \\ &= \iint_{-\infty}^{\infty} A_o(k_x, k_y) e^{-j\mathbf{k}\mathbf{n}\cdot\mathbf{r}} dk_x dk_y \end{aligned} \quad (3.14)$$

The whole field for $z > 0$ is specified by $A_o(k_x, k_y)$, which itself does not change over the half-space $z > 0$. It should be noted that it is *interference* between this collection of plane waves that gives rise to the changing form of the field with x, y and z . In particular the *localisation* of the beam is a consequence of the interference, since the plane waves themselves are unbounded, except for the plane $z = 0$.

3.2 Gaussian Beam-Mode Optics

3.2.1 Derivation of Beam-modes

Consider the situation where an electromagnetic wave propagates essentially parallel to some axis, with a restricted degree of divergence from that axis. If the amount of divergence is kept within certain bounds then the propagation can be called *paraxial* and certain approximations can be made. These approximations are called the *paraxial* or *Fresnel* approximations. Within this section it is shown that a beam propagating paraxially along an axis can be represented as a superposition of independent beam-modes. Each beam-mode maintains its characteristic field amplitude distribution as it propagates, apart from scaling, and also maintains a spherical phase-front (though it does have a shifting centre of curvature).

In the first instance, the beam-modes themselves will be described and then it will be shown how these follow from the angular spectrum of plane waves treatment given in the previous section. The following development is essentially that of Martin[6].

The beam-modes typically incorporate either the Hermite or Laguerre polynomials. The treatment here incorporates only the Hermite polynomials, though a parallel treatment could be presented for the Laguerre polynomials. The Hermite polynomials $\mathcal{H}_n(\chi)$, $n = 0, 1, 2, \dots$ constitute an infinite set. The n denotes the mode or order number, and all the modes together form an orthogonal set. χ can be taken to be some constant times a Cartesian coordinate x or y . Given that $\mathcal{H}_0(\chi)$ is unity and $\mathcal{H}_1(\chi)$ is 2χ , the following recursion formula generates the subsequent members of the set.

$$\mathcal{H}_{n+1} = 2(\chi\mathcal{H}_n - n\mathcal{H}_{n-1}) \quad (3.15)$$

The first five members of the set are

$$\mathcal{H}_0(\chi) = 1 \quad (3.16)$$

$$\mathcal{H}_1(\chi) = 2\chi \quad (3.17)$$

$$\mathcal{H}_2(\chi) = 4\chi^2 - 2 \quad (3.18)$$

$$\mathcal{H}_3(\chi) = 8\chi^3 - 12\chi \quad (3.19)$$

$$\mathcal{H}_4(\chi) = 16\chi^4 - 48\chi^2 + 12 \quad (3.20)$$

The beam-modes are formed by combining the Hermite polynomial functions with the Gaussian function e^{-ax^2} and by including a normalisation factor. The normalisation ensures that the square of the field amplitude integral over any beam-mode cross-section is unity, (i.e. normalised to carry constant unity power). These *Gauss-Hermite* functions also constitute an infinite set of orthogonal functions. The first mode (i.e. the zeroth-order mode) is called the fundamental beam-mode, and the form of this mode is

$$u_{00}(x, y, z) = \sqrt{\frac{2}{\pi}} \frac{1}{\omega} e^{-\left(\frac{x^2+y^2}{\omega^2}\right)} e^{-j\left(\frac{kr^2}{2R} - \Phi\right)} \quad (3.21)$$

where

$$\Phi = \tan^{-1} \hat{z} \quad (3.22)$$

$$\omega^2 = \omega_0^2(1 + \hat{z}^2) \quad (3.23)$$

$$\hat{R} = \hat{z} + \frac{1}{\hat{z}} \quad (3.24)$$

or

$$R = z \left(1 + \frac{1}{\hat{z}^2} \right) \quad (3.25)$$

and the normalised distance \hat{z} has been introduced. The normalisation factor is $k\omega_o^2/2$ and this factor is sometimes called the confocal distance or the Rayleigh range. It is the distance at which the wavefront curvature is a maximum and it also marks the transition between the near-field and the far-field. Thus

$$\hat{z} = \frac{2(z - z_o)}{k\omega_o^2} \quad (3.26)$$

where z_o is the position of the beam waist and ω_o it's magnitude. In general ω is the beam radius and it is the radial distance from the axis of propagation at which the amplitude has fallen to $1/e$ of it's on-axis value at the same z . It's minimum value is ω_o . R is the radius of the phase-front curvature and Φ is called the anomolous phase term. Φ is in fact the difference between the phase of the beam at a given z from what the phase would have been for a plane wave that had travelled the same distance. If the fundamental beam-mode is not axially symmetric, (i.e. astigmatic), then there are different beam size parameters for the x and y directions. Hence

$$u_{oo}(x, y, z) = \sqrt{\frac{2}{\pi}} \frac{1}{\sqrt{\omega_x \omega_y}} e^{-\left(\frac{x^2}{\omega_x^2} + \frac{y^2}{\omega_y^2}\right)} e^{-j\left(\frac{kx^2}{2R_x} + \frac{ky^2}{2R_y} - \frac{\Phi_x}{2} - \frac{\Phi_y}{2}\right)} \quad (3.27)$$

Using the Hermite polynomials, the general beam-mode can now be written as

$$u_{mn}(x, y, z) = \left[\frac{1}{2^{n+m} m! n!} \mathcal{H}_m \left(\frac{\sqrt{2} x}{\omega_x} \right) \mathcal{H}_n \left(\frac{\sqrt{2} y}{\omega_y} \right) e^{j(m\Phi_x + n\Phi_y)} \right] u_{oo}(x, y, z) \quad (3.28)$$

The polynomials modulate the Gaussian amplitude distribution of the fundamental beam-mode, and a phase-slippage $m\Phi_x + n\Phi_y$ relative to the fundamental beam-mode is introduced. For a beam with $\omega_{ox} = \omega_{oy} = \omega_o$ and $z_{ox} = z_{oy} = z_o$, $u_{mn}(x, y, z)$ simplifies to

$$u_{mn}(x, y, z) = \left[\frac{1}{2^{n+m} m! n!} \mathcal{H}_m \left(\frac{\sqrt{2} x}{\omega} \right) \mathcal{H}_n \left(\frac{\sqrt{2} y}{\omega} \right) e^{j(m+n)\Phi} \right] u_{oo}(x, y, z) \quad (3.29)$$

It is important to note that all of the beam-modes are characterised by the same beam waist width parameter ω_o and it's associated location z_o , (at which the phase-front is planar). Once these are specified the consequent beam width parameter ω and phase-front radius of curvature R depend only upon z , and specifically not upon the mode numbers m, n . However the z -dependent phase slippage also depends upon the

mode numbers. Specifically, for the case where $\omega_{ox} = \omega_{oy} = \omega_o$ and $z_{ox} = z_{oy} = z_o$, $u_{mn}(x, y, z)$, the anomolous phase term Φ_{mn} becomes

$$\Phi_{mn} = (m + n + 1) \tan^{-1} \hat{z} \quad (3.30)$$

Superpositions of Gauss-Hermite (or Gauss-Laguerre) functions can be found to fit any distribution of field amplitude over a spherical phase-front. Such a fitting comprises an analysis into beam-modes which in paraxial approximation, propagate independently in an isotropic medium. The choice of the beam waist parameter ω_o is arbitrary, though a sensible choice would normally exist (e.g. one that minimises the number of modes having significant magnitude in the superposition).

In order to show that the above defined Gaussian beam-modes indeed form a solution to the scalar Helmholtz wave equation, consider again the angular spectrum of plane waves solution of the wave equation for the field $\psi(x, y, z)$, as given in equation 3.14, viz.

$$\psi(x, y, z) = \iint_{-\infty}^{\infty} A_o(k_x, k_y) e^{-j\mathbf{k}\cdot\mathbf{r}} dk_x dk_y$$

For paraxial propagation, the paraxial or Fresnel assumption can be made, which is that the angular spectral function $A_o(k_x, k_y)$ will only have a significant magnitude at values of k_x, k_y such that

$$k_x \ll k \quad k_y \ll k \quad (3.31)$$

This means that the electromagnetic wave is essentially propagating along the z -axis, with only a small amount of divergence in the two orthogonal directions. Since $k^2 = k_x^2 + k_y^2 + k_z^2$, and with the above assumption, k_z can be written as follows

$$\begin{aligned} k_z &= k \left(1 - \frac{k_x^2 + k_y^2}{k^2} \right)^{\frac{1}{2}} \\ &\approx k \left(1 - \frac{k_x^2 + k_y^2}{2k^2} \right) \end{aligned} \quad (3.32)$$

and thus

$$\mathbf{k}\cdot\mathbf{r} \approx kz + \left(k_x x + k_y y - \frac{k_x^2 + k_y^2}{2k} z \right) \quad (3.33)$$

Therefore the field amplitude $\psi(x, y, z)$ can now be expressed as

$$\begin{aligned} \psi(x, y, z) &= u(x, y, z) e^{-jkz} \\ &\approx e^{-jkz} \iint_{-\infty}^{\infty} A_o(k_x, k_y) e^{j \left(\frac{k_x^2 + k_y^2}{2k} \right) z} e^{-j(k_x x + k_y y)} dk_x dk_y \end{aligned} \quad (3.34)$$

and $u(x, y, z)$ is revealed to be the *Fourier transform* of the product

$$A(k_x, k_y) e^{j \left(\frac{k_x^2 + k_y^2}{2k} \right) z} \quad (3.35)$$

There are two Fourier transform properties of Gauss-Hermite functions that can now be used to unveil the relationship between the beam-modes described by equation 3.28 and the above solution $\psi(x, y, z)$ of the scalar Helmholtz wave equation in paraxial approximation. Ultimately, the requirement is to find the form of $u(x, y, z)$ in equation 3.34. Recall that the basic form of the Gauss-Hermite function is

$$\mathcal{G}_m(\chi) = \mathcal{H}_m(\chi) e^{-\frac{\chi^2}{2}} \quad (3.36)$$

The Fourier transform of an m th-order Gauss-Hermite function is itself an m th-order Gauss-Hermite function and similarly for the inverse Fourier transform of an m th-order Gauss-Hermite function [7, §7.376(1)]. Thus

$$\begin{aligned} \mathcal{F}^{-1}[\mathcal{G}_m(\chi)] &= \frac{1}{2\pi} \int_{-\infty}^{\infty} \mathcal{H}_m(\chi) e^{-\frac{\chi^2}{2}} e^{j\kappa_x \chi} d\chi \\ &= \frac{j^m}{\sqrt{2\pi}} \mathcal{G}_m(\kappa_x) \end{aligned} \quad (3.37)$$

Also, the Fourier transform of an m th-order Gauss-Hermite function multiplied by a Gaussian function is a scaled and phase-shifted version of the original m th-order Gauss-Hermite function, that is

$$\mathcal{F} \left[\mathcal{G}_m(\kappa_x) e^{j \frac{v \kappa_x^2}{2}} \right] = \frac{(-j)^m}{(1 - v^2)^{\frac{1}{4}}} \mathcal{G}_m \left(\frac{\chi}{(1 + v^2)^{\frac{1}{2}}} \right) e^{-j \left(\frac{v \chi^2}{2(1 + v^2)} - (m + \frac{1}{2}) \tan^{-1} v \right)} \quad (3.38)$$

The Gauss-Hermite functions form a complete orthogonal set and thus the field over the xy plane ($z = 0$) can be expressed as a linear combination of these functions, that is

$$\psi(x, y, 0) = \sum_{m,n} C_{mn} \mathcal{G}_m(\chi) \mathcal{G}_n(\Lambda) \quad (3.39)$$

where $\chi = \sqrt{2} x / \omega_{ox}$ and $\Lambda = \sqrt{2} y / \omega_{oy}$ and ω_{ox} and ω_{oy} can be identified as the beam waist parameters (i.e. e^{-1} level). The C_{mn} coefficients can be found by evaluating the following integral (i.e. essentially a two-dimensional cross-correlation integral)

$$C_{mn} = \iint_{-\infty}^{\infty} \psi(x, y, 0) \mathcal{G}_m \left(\frac{\sqrt{2} x}{\omega_{ox}} \right) \mathcal{G}_n \left(\frac{\sqrt{2} y}{\omega_{oy}} \right) dx dy \quad (3.40)$$

Recall that the angular spectrum of plane waves $A_o(k_x, k_y)$ is in fact the two-dimensional inverse Fourier transform of the field distribution $\psi(x, y, 0)$. Thus $A_o(k_x, k_y)$

can be found by finding the inverse Fourier transform of equation 3.39 and taking note of property 3.37. Within the inverse Fourier transform the factors $k_x x$ and $k_y y$ are substituted with the factors $\kappa_x \chi$ and $\kappa_y \Lambda$ respectively, where

$$\begin{aligned} k_x x &= \kappa_x \chi \\ \Rightarrow \kappa_x &= \frac{\sqrt{2} k_x}{\omega_{kx}} \end{aligned} \quad (3.41)$$

and where

$$\omega_{kx} = \frac{2}{\omega_{0x}} \quad (3.42)$$

Similarly for $\kappa_y \Lambda$

$$\kappa_y = \frac{\sqrt{2} k_y}{\omega_{ky}} \quad (3.43)$$

and

$$\omega_{ky} = \frac{2}{\omega_{0y}} \quad (3.44)$$

Therefore $A_o(k_x, k_y)$ can be expressed as follows

$$\begin{aligned} A_o(k_x, k_y) &= \frac{1}{(2\pi)^2} \int \int_{-\infty}^{\infty} \psi(x, y, 0) e^{j(k_x x + k_y y)} dx dy \\ &= \frac{\omega_{0x} \omega_{0y}}{2(2\pi)^2} \sum_{m,n} C_{mn} \int_{-\infty}^{\infty} \mathcal{G}_m(\chi) e^{j\kappa_x \chi} d\chi \int_{-\infty}^{\infty} \mathcal{G}_n(\Lambda) e^{j\kappa_y \Lambda} d\Lambda \\ &= \frac{\omega_{0x} \omega_{0y}}{2} \sum_{m,n} C_{mn} \frac{j^{(m+n)}}{2\pi} \mathcal{G}_m(\kappa_x) \mathcal{G}_n(\kappa_y) \end{aligned} \quad (3.45)$$

The form of $u(x, y, z)$ can now be found. Recall that

$$u(x, y, z) = \mathcal{F} \left[A_o(k_x, k_y) e^{j \left(\frac{k_x^2 + k_y^2}{2k} \right) z} \right] \quad (3.46)$$

and thus by substituting for $A_o(k_x, k_y)$ and noting property 3.38, the form of $u(x, y, z)$ can be expressed in the following way

$$\begin{aligned} u(x, y, z) &= \sum_{m,n} C_{mn} \frac{j^{(m+n)}}{2\pi} \int_{-\infty}^{\infty} \mathcal{G}_m(\kappa_x) e^{j \frac{v_x \kappa_x^2}{2}} e^{-j \kappa_x \chi} d\kappa_x \\ &\quad \int_{-\infty}^{\infty} \mathcal{G}_n(\kappa_y) e^{j \frac{v_y \kappa_y^2}{2}} e^{-j \kappa_y \Lambda} d\kappa_y \\ &= \sum_{m,n} C_{mn} \frac{j^{(m+n)}}{2\pi} \frac{(-j)^m}{(1 - v_x^2)^{\frac{1}{4}}} \mathcal{G}_m \left(\frac{\chi}{(1 + v_x^2)^{\frac{1}{2}}} \right) e^{-j \left(\frac{v_x \chi^2}{2(1 + v_x^2)} - (m + \frac{1}{2}) \tan^{-1} v_x \right)} \\ &\quad \frac{(-j)^n}{(1 - v_y^2)^{\frac{1}{4}}} \mathcal{G}_n \left(\frac{\Lambda}{(1 + v_y^2)^{\frac{1}{2}}} \right) e^{-j \left(\frac{v_y \Lambda^2}{2(1 + v_y^2)} - (n + \frac{1}{2}) \tan^{-1} v_y \right)} \end{aligned} \quad (3.47)$$

Various comparisons can now be made between this result and the form of the beam modes as described within the early part of this section, and summarised by equation 3.28. Firstly, the v variables can be identified as the normalised z distances, that is

$$\begin{aligned} v_x &= \frac{2z}{k\omega_{ox}^2} = \hat{z}_x \\ v_y &= \frac{2z}{k\omega_{oy}^2} = \hat{z}_y \end{aligned} \quad (3.48)$$

With this result the variables of the Gauss-Hermite functions can be seen to be

$$\frac{\chi}{(1 + \hat{z}_x^2)^{\frac{1}{2}}} = \frac{\sqrt{2}x}{\omega_x} \quad (3.49)$$

and

$$\frac{\Lambda}{(1 + \hat{z}_y^2)^{\frac{1}{2}}} = \frac{\sqrt{2}y}{\omega_y} \quad (3.50)$$

where

$$\begin{aligned} \omega_x^2 &= \omega_{ox}^2(1 + \hat{z}_x^2) \\ \omega_y^2 &= \omega_{oy}^2(1 + \hat{z}_y^2) \end{aligned} \quad (3.51)$$

Also the first phase terms can similarly be shown to be equal to

$$\frac{kx^2}{2R_x} \quad \text{and} \quad \frac{ky^2}{2R_y} \quad (3.52)$$

where

$$R_x = z_x(1 + \hat{z}_x^{-2}) \quad \text{and} \quad R_y = z_y(1 + \hat{z}_y^{-2}) \quad (3.53)$$

The anomolous phase terms $\Phi_{m,n}$ are already in the right form, and the j factors are seen to all cancel. Finally, note that the $(1 - v^2)^{\frac{1}{4}}$ factors have the same order of dependence on \hat{z} as the $1/\sqrt{\omega}$ factors in equation 3.27. Thus it is seen that there is an essential equivalence, (i.e. excepting for normalisation), between the beam-modes as decribed in equation 3.28 and the angular spectrum of plane waves solution to the scalar Helmholtz wave equation in paraxial approximation, as given in equation 3.34. Hence it can be stated that

$$u(x, y, z) \equiv \sum_{m,n} C_{mn} u_{mn}(x, y, z) \quad (3.54)$$

apart from normalisation.

The Far-Field

It is interesting to examine the form of $\psi(x, y, z)$ in the far-field, (i.e. as $z \rightarrow \infty$). Foley and Wolf[8] have shown how in the far-field $\psi(x, y, z)$ is directly related to $A_o(k_x, k_y)$. Transforming to spherical polar coordinates, $(x, y, z) \rightarrow (\rho, \theta, \phi)$, $A_o(k_x, k_y)$ becomes $A_o(\theta, \phi)$ and

$$\lim_{k\rho \rightarrow \infty} \psi(\rho, \theta, \phi) = -2\pi j \cos \theta A_o(\theta, \phi) \frac{e^{-jk\rho}}{k\rho} \quad (3.55)$$

Thus an observer at a distant point (ρ, θ, ϕ) receives a beam with a spherical wave-front, centred at the origin, with amplitude $2\pi A_o(\theta, \phi) \cos \theta$. For paraxial directions, $\cos \theta \rightarrow 1$ and thus $\psi(x, y, z) \equiv A_o(k_x, k_y)$. That is, the far-field pattern is the Fourier transform of the field distribution over the aperture. This is a well known result. This result is expressed in terms of Gaussian beam-modes in equation 3.45. Note that the $j^{(m+n)}$ factor in this equation and the j factor in the above equation are all inherently present within the Gaussian beam-mode representation of the field for the whole half-space $z > 0$ as given in equations 3.47 and 3.28. In the far-field the anomolous phase term Φ_{mn} within these equations, becomes

$$\lim_{z \rightarrow \infty} \Phi_{mn} = (m + n + 1) \frac{\pi}{2} \quad (3.56)$$

which accounts for all of the j factors present in the above far-field expression, (i.e. the $(m + n)j$ in $A_o(\theta, \phi)$ and the explicit j).

3.2.2 Application to MMW QO SLMs

When a millimetre wave beam within a quasi-optical circuit encounters a MMW QO SLM, it's form is modified in some fashion (i.e. in amplitude, phase, or polarisation). Typically the incident beam would be an axially symmetric fundamental mode Gaussian beam. In terms of the foregoing description of a MMW QO beam, and SLM converts a single mode beam into a multi-mode beam, and the purpose of this section is to outline how the mode coefficients can be calculated for a given SLM function.

Equation 3.54 shows that a general beam propagating in free space may be regarded as a linear superposition of modes, where from equations 3.28 and 3.34, each mode is of the form

$$\psi_{mn}(x, y, z) = e^{-jkz} u_{mn}(x, y, z) \quad (3.57)$$

If the total beam is represented by $\Psi(x, y, z)$, then again from the foregoing work

$$\Psi = \sum_{mn} A_{mn} \psi_{mn} \quad (3.58)$$

where A_{mn} is a complex number which determines the amplitude and phase of the contribution of ψ_{mn} , and recall that ψ_{mn} has been normalised in such a way that the beam-mode carries constant unity power. Following Lesurf, the normalisation can be expressed in the following succinct way[9]

$$\langle \psi_{mn} | \psi_{mn} \rangle = 1 \quad (3.59)$$

where the bracket notation is defined as follows

$$\langle \Phi | \Psi \rangle \equiv \iint_{-\infty}^{\infty} \Phi \Psi^* dx dy \quad (3.60)$$

This notation enables the equations to be written in a coordinate free sense. The functions ψ_{mn} are mutually orthogonal, and thus

$$\langle \psi_{mn} | \psi_{pq} \rangle = 0 \quad \text{if } m \neq p \text{ or } n \neq q \quad (3.61)$$

From the above it can be seen that

$$\langle \Psi | \psi_{mn} \rangle = \sum_{pq} \langle A_{pq} \psi_{pq} | \psi_{mn} \rangle \quad (3.62)$$

and thus from equation 3.61, the mode coefficients for a multi-mode beam are given by

$$A_{mn} = \langle \Psi | \psi_{mn} \rangle \quad (3.63)$$

Note also that these expressions may be separated into one-dimensional expressions, and so

$$\langle \psi_m | \psi_m \rangle = 1 \quad (3.64)$$

and

$$A_m = \langle \Psi | \psi_m \rangle \quad (3.65)$$

also hold. The plane of integration can be at any point along the beam, but there is normally a convenient plane, and here it will invariably be the plane in which the SLM is positioned. Therefore, if Ψ represents the multi-mode beam that is produced by the SLM, the modal coefficients of the various modes that go to make up Ψ can be found by using the above equation. For example, consider the simple illustrative case where

the SLM function involves imposing a π radian phase shift over half of the beam. For this case, the form of Ψ can be written directly as

$$\Psi = \begin{cases} \psi_0 & x > 0 \\ -\psi_0 & x < 0 \end{cases} \quad (3.66)$$

It can then be shown that the modal coefficients (in one dimension) are given by

$$A_m = 2 \int_0^\infty \psi_0 \psi_m^* dx \quad m = 1, 3, 5, \dots \quad (3.67)$$

3.2.3 Aperture Considerations

Thus far, the finite nature of the various apertures within a MMW QO system have not been considered. It has already been shown how the mode coefficients for the multi-mode beam produced by the SLM can be determined. Precisely the same technique can be used at an aperture[9]. The field $\Psi(x, y, z')$ at the aperture could be calculated from knowledge of the mode coefficients and the distance $z' = z_a - z_{slm}$, and then a truncated version, $\Psi'(x, y, z')$ could be used to determine a new set of mode coefficients, B_{mn} . However, if the power contained within the higher order modes is small, an approximate method can be applied. This method involves determining the efficiencies of transfer for all the modes, for a given optics configuration, (i.e. specified by a Fresnel number N), and for a specific aperture size and shape. It happens that there exists a sharp cut-off characteristic for any given finite optics configuration, and essentially only modes up to a certain order, say p , can pass through the optics without significant attenuation. Fox and Li[10] have examined numerically the losses encountered within two-mirror resonators. They considered rectangular plane mirrors, circular plane mirrors and circular confocal mirrors. This last case is the case that is of interest here, for it is equivalent to a lens waveguide which is what is effectively being considered here. Fox and Li have computed the power lost *per transit* in the resonator, which is equivalent to *per aperture*, as a function of the Fresnel number N for confocal spherical mirrors or equivalently for a confocal lens arrangement. N is given by

$$N = \frac{a^2}{b\lambda} \quad (3.68)$$

where a is the radius of the aperture, λ is the wavelength and b is the distance between the apertures (i.e. lens to lens spacing). The results given are for the first three modes. Power loss coefficients for the modes higher than those given can at least be given

lower bounds. Heurtley[11] has tackled this problem analytically with the help of hyperspheroidal functions. His work should be consulted if the the number of modes to be considered is large. Summarising then, with the approximation being used here, the total field Ψ' that can be processed by a MMW QO system is given by

$$\Psi' \approx \sum_{mn}^p A_{mn} \psi_{mn} \quad (3.69)$$

where p is determined by consulting either Fox and Li, or Heurtley. Note that this approximation will really only be useful if the power in the modes with mode numbers greater than p is small.

3.3 Fourier Optics

3.3.1 Coherent Optical Imaging

Fourier optics is primarily concerned with the formation and processing of images. Within the image formation process, diffraction is an intermediate process. A typical imaging system includes at least one lens and it is the diffraction pattern produced in the back focal plane of a converging lens that is of specific interest. This particular diffraction pattern is called a Fraunhofer diffraction pattern and it is in fact a two-dimensional Fourier transform of the *object function*[4, chapter 5]. This *object function* can be defined as the field distribution in a specific plane perpendicular to optical axis and it could be formed in a variety of ways, (for example it could be a transparency illuminated with with a mono-chromatic plane wave). If the object function is positioned in the front focal plane of the lens then the Fourier transform produced in the back focal plane is exact in amplitude and phase (neglecting aperture effects for the moment). For other positions, either side of the lens, phase and amplitude scaling factors are introduced, but the Fourier transformation process essentially remains intact. Martin[6, §4.5] has shown how this Fourier transforming function of a lens is established with the Gaussian beam-mode description developed earlier in this chapter. In summary, he shows that the total phase slippage for each mode, from the input focal plane of a lens to the output focal plane is $(m + n + 1)\pi/2$, which is consistent with the Fourier transforming properties of the Gauss-Hermite function—see equation 3.37. The Fraunhofer diffraction pattern is also formed at infinity (i.e. on a distant spherical surface) when the lens removed. Thus the Fraunhofer diffraction pattern is also called a *far-field* diffraction pattern.

Image formation may be regarded as a double Fourier process[13, §5.3] with the Fraunhofer diffraction pattern being the Fourier *analysis* of the object function and the *image* being the Fourier *synthesis* of the Fourier analysis. Again, Martin[6, §5.4] shows that within the Gaussian beam-mode description, that if there are two lenses separated by the sum of their focal lengths, the overall phase shift from input to output is twice the above, that is, $(m + n + 1)\pi$. This implies that there are no relative phase shifts between beam-modes of any order, that is, that Fourier transformation by the first lens followed by Fourier transformation by the second lens leaves the output field identical with the input. For perfect imaging, an infinite Fourier analysis and synthesis would be required. The optical imaging system would need to be able to generate and admit the entire diffraction pattern produced for any given object function. This is clearly impossible with lenses and apertures of finite diameter. Section 3.3.2 discusses how these limitations affect the imaging process.

Optical processing as opposed to imaging, is concerned with intervention in the imaging process in order to obtain an image that is altered (i.e. processed) in some desired fashion. The back focal plane of a lens within an imaging system is also called the Fourier transform plane, and it is within this plane that various optical processing techniques can be applied. The basic optical arrangement for coherent optical imaging and processing is shown in figure 3.1. Within the Fourier transform plane there exists the spatial frequency spectrum of the object function. This spatial frequency spectrum can be filtered, and for example, this might simply involve the placing of an aperture in this plane which prevents the frequencies above a certain value from contributing to the formation of the image (i.e. a low-pass filter). Various kinds of filters can be used according to the application. The low-pass filter is an example of an amplitude-only filter. Phase-only filters and complex (holographic) filters could also be employed. A spatial light modulator (SLM) is a specific physical implementation of a filter.

Of special interest within the context of pattern recognition is the cross-correlation image produced with a complex Vander Lugt filter[14]. For every object function there exists a specific complex Vander Lugt filter. Now if a number of object functions are inspected it is only when the filter and the object function are *matched* together that the cross-correlation image of a bright central spot is produced. Thus this kind of filter forms the basis for pattern identification and recognition systems. Filters of this type are called *matched filters*. The development of filters for cross-correlation image

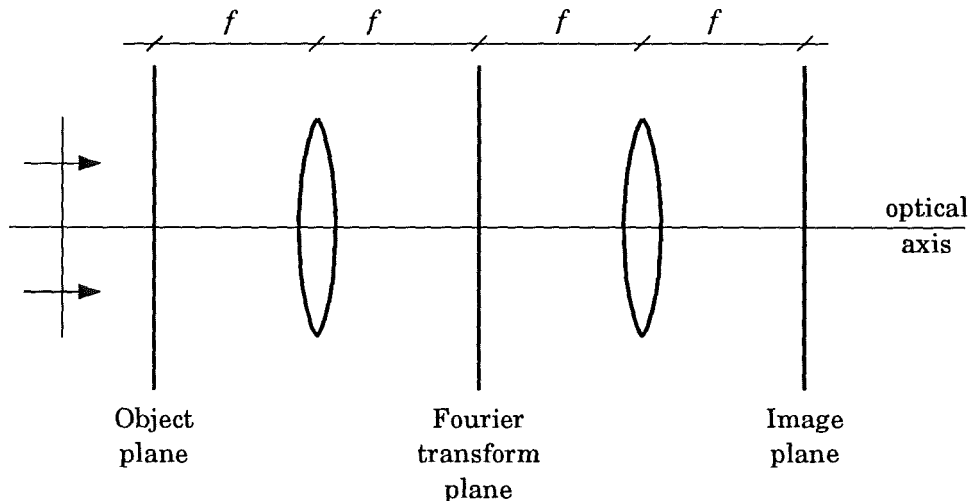


Figure 3.1: The basic arrangement for coherent optical filtering. (SOURCE: Steward[13] fig. 5.13, p. 123.)

processing has moved on from Vander Lugt's original work and section 2.2.4 references the more recent work in this area. In particular, phase-only filters and binary phase-only filters are gaining attention because they are readily able to be implemented with current SLM technology.

Coherence

The kind of optical processing that requires access to the Fourier transform of an object function, relies upon the existence of temporally and spatially coherent illumination.³ Temporal coherence can be identified qualitatively as the interval of time during which the phase of a given wave motion changes in a predictable way as it passes a fixed point in space. Related to temporal coherence is the spectral purity of sources. A truly monochromatic source would need to exist for all time, which is clearly not possible. Thus the idea of quasi-monochromaticity becomes involved. Spatial coherence conditions exist when the phase relationship between various points across the illuminating beam (and thus the object function) are constant. For the Fraunhofer diffraction pattern to be properly formed, that is, for it to be observable and able to be processed, there are minimum requirements on the temporal and spatial coherence of the illuminating

³Incoherent processing systems exist and have some advantages—see Steward[13, §5.5.2].

source. Conventional sources (i.e. coherent sources such as Gunn diode oscillators for millimetre waves and lasers for optical waves) are obviously not perfect and so provide illumination that is to a greater or lesser extent coherent, that is, the illumination is said to be partially coherent. In some circumstances the partially coherent nature of the source needs careful examination. Steward provides a brief treatment of partial coherence and correlation within the context of interferometry[13, §7.4]. When the object illumination is sufficiently coherent, the imaging system is linear in complex amplitude. In contrast, it can be noted that incoherent imaging systems are linear in intensity.

3.3.2 Apertures—Two Models

Abbe-Porter Model

The Abbe-Porter theory of image formation involves a consideration of the whole wavefront leaving an object, as opposed to the wavefront leaving each object point individually. It is within this particular theory that the image formation process can be described as a double Fourier transformation process. To calculate the effect of an aperture on the process, an aperture function can be defined that is equal to unity inside its boundary and zero outside. If the aperture exists say in the Fourier transform plane, then the image is the transform of that part of the pattern in the diffraction plane that contributes to the image. This can be expressed as follows[13]

$$\text{Image} = \mathcal{F}[\mathcal{F}[\text{Object}] \times (\text{Ap.fn})] \quad (3.70)$$

If the aperture to be considered is in a different plane, then for the above relation to hold for Gaussian beam-modes, the aperture function (Ap.fn) will need to be scaled in size. This is because with Gaussian beam-modes, the wavefront of the beam incident upon the lens is not planar, and the beam's size is a function of position, (i.e. it is characterised by ω , where $\omega = \omega_0 \sqrt{1 + \hat{z}^2}$). For example, if the aperture to be considered is in the *lens* plane, then the above relation will only hold if (Ap.fn) is scaled by the factor $\sqrt{1 + \hat{z}^2}$. This is for the case where the beam waist ω_0 is in the SLM plane, which is the most likely configuration in practise.

Rayleigh-Duffieux Model

Within this model, each object point is regarded as a source of light, and for circular apertures, is imaged as the Airy pattern⁴ of the imaging lens[13]. The whole image distribution is then the convolution of the object distribution with this Airy pattern, and thus can be expressed as

$$\text{Image} = \text{Object} * \mathcal{F}[\text{Ap.fn}] \quad (3.71)$$

The same scaling argument made above regarding the aperture function (Ap.fn) still applies. These two models are directly related by the convolution theorem, that is application of the convolution theorem to equation 3.70 produces equation 3.71.

References

- [1] J. C. G. Lesurf, *Millimetre-wave Optics Devices and Systems*. Adam Hilger, 1990.
- [2] S. Silver, "Microwave Aperture Antennas and Diffraction Theory," *J. Opt. Soc. Am.*, vol. 52, p. 131, 1962.
- [3] D. H. Martin (and R. B. Jones), *Lecture 6: Propagation of Vector Fields*. Millimetre Wave Optics Course, QMW(QMC), University of London, 1980s.
- [4] J. W. Goodman, *Introduction to Fourier Optics*. McGraw-Hill Book Company, 1968.
- [5] M. Abramowitz and I. A. Stegun, *Handbook of Mathematical Functions*. Dover Publications, Inc., New York, Dover Edition first published in 1965.
- [6] D. H. Martin, *Lecture 4: Gaussian Beam-Mode Analysis of Paraxial Propagation*. Millimetre Wave Optics Course, QMW(QMC), University of London, 1980s.
- [7] I. S. Gradshteyn and I. M. Ryzhik, *Tables of Integrals, Series and Products*. 4th ed., Academic Press, 1965.
- [8] J. T. Foley and E. Wolf, *J. Opt. Soc. Am.*, vol. 69, p. 761, 1979.
- [9] J. C. G. Lesurf, "Gaussian Beam-Mode Optics and the Design of Millimetre-wave Martin-Puplett Instruments," *Infrared Physics*, vol. 28, pp. 129–137, 1988.

⁴Note that the Fourier transform of a circular aperture function is the Airy pattern.

- [10] A. G. Fox and T. Li, "Resonant Modes in a Maser Interferometer," *The Bell System Technical Journal*, pp. 453–488, March 1961. (See figure 15 in particular.)
- [11] J. C. Heurtley, "Hyperspheroidal Functions—Optical Resonators with Circular Mirrors," *Proceedings of the Symposium on Quasi-Optics*, Polytechnic Press of the Polytechnic Institute of Brooklyn, pp. 367–375, 1964.
- [12] D. Slepian and E. Sonnenblick, "Eigenvalues Associated with Prolate Spheroidal Wave Functions of Zero Order," *The Bell System Technical Journal*, pp. 1745–1759, October 1965.
- [13] E. G. Steward, *Fourier Optics - an introduction 2nd ed.* Ellis Horwood Limited, 1987.
- [14] A. B. Vander Lugt, "Signal Detection by Complex Spatial Filtering," *IEEE Trans. Inform. Theory*, vol. 10, no. 2, 1964.

Chapter 4

SLM Pattern Measurement

The Experiment

The purpose of the experiment described within this chapter is to provide a convenient method for examining the spatial profiles of MMW QO beams that have been phase modulated by a MMW QO SLM. In essence, the experimental approach taken is to allow a phase modulated beam to propagate into the *far-field* where its *radiation pattern* is then measured. In effect, the MMW QO SLM could be viewed as a part of an antenna system, the final element of which is either a lens or possibly an open aperture.

There are two main reasons for doing this experiment. Firstly, the analytical approach described in chapter 3 needs experimental verification. The analytical methods are not complete in their representation of the true physical situation, and thus the assumptions and approximations made need some exploration so that limits on the applicability of the methods used can be determined. Secondly, this experiment establishes an approach for experimental analysis of spatial signal processing devices or systems, that is applicable to a wide variety of situations; (e.g. using a MMW QO SLM for beam forming, shaping and/or scanning). This in itself is of considerable value.

Firstly the design of MMW QO SLMs is reviewed and described. Following this, the radiation pattern measurement system and the associated quasi-optical circuit is described. Finally, the measurement system as a whole is briefly evaluated.

4.1 MMW QO SLM Design

4.1.1 Background

A spatial light modulator (SLM) is a real-time reconfigurable device capable of modifying the amplitude (or intensity), phase, or polarisation of an optical wavefront as a function of two spatial dimensions and time. The modulation is performed in response to information-bearing control signals[1]. There are four major classification categories for SLMs and within each of these categories there are number of further divisions. These categories are outlined below:

1. Modulation mechanism
 - (a) Mechanical
 - (b) Magneto-optic
 - (c) Electro-optic
 - (d) Thermal
2. Modulation variable
 - (a) Intensity (amplitude)
 - (b) Phase
 - (c) Polarisation
 - (d) Spatial frequency spectrum (texture)
3. Addressing mode
 - (a) Electrically addressed
 - (b) Optically addressed
4. Addressing mechanism
 - (a) Electrically addressed SLMs
 - i. Electron beam
 - ii. Matrix-addressed electrode array
 - iii. Active switching matrix
 - (b) Optically addressed SLMs

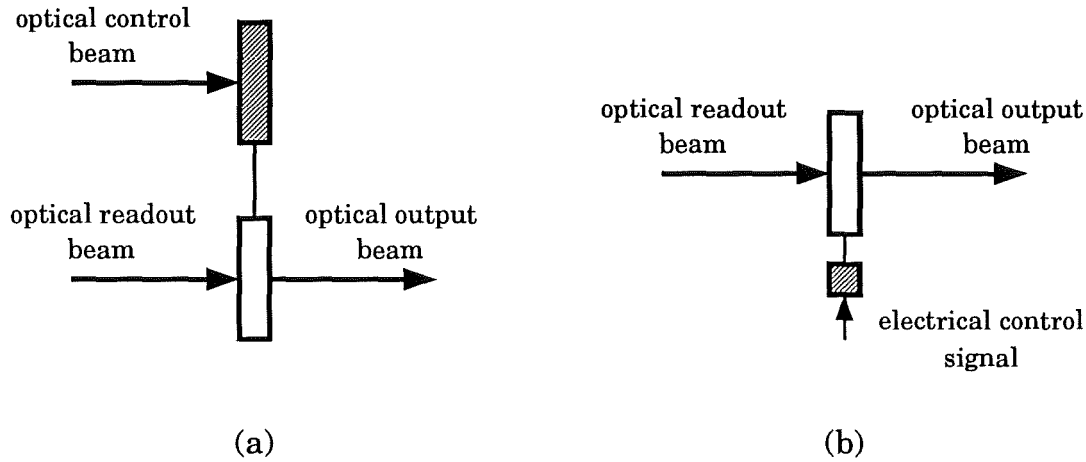


Figure 4.1: (a) A single cell of an optically addressed SLM. (b) A single cell of an electrically addressed SLM. (SOURCE: Neff *et al* [1], figure 1, p. 826.)

- i. photoconductive/photovoltaic
- ii. photoemissive
- iii. semiconductor junction (diode, transistor)
- iv. thermal

Reference [1] is a tutorial overview of 2D SLMs and describes these various categories in detail. A functional block diagram of a single resolution element of a 2D SLM is shown in figure 4.1. This figure schematically describes the manner in which the two different addressing modes function. There are many different combinations possible from the above outline, but not all combinations are logical or even feasible. The most common optically and electrically addressed category is that of electro-optic modulation employing polarisation or phase modulation. Mechanical modulation of phase is the next most exploited category, and is the category that has been chosen for the specific MMW QO SLMs used here.

4.1.2 A Mechanical Spatial Phase Modulator

This category has been chosen because of its simplicity in design and construction and also because the modulation of phase with this kind of modulator is a precisely defined

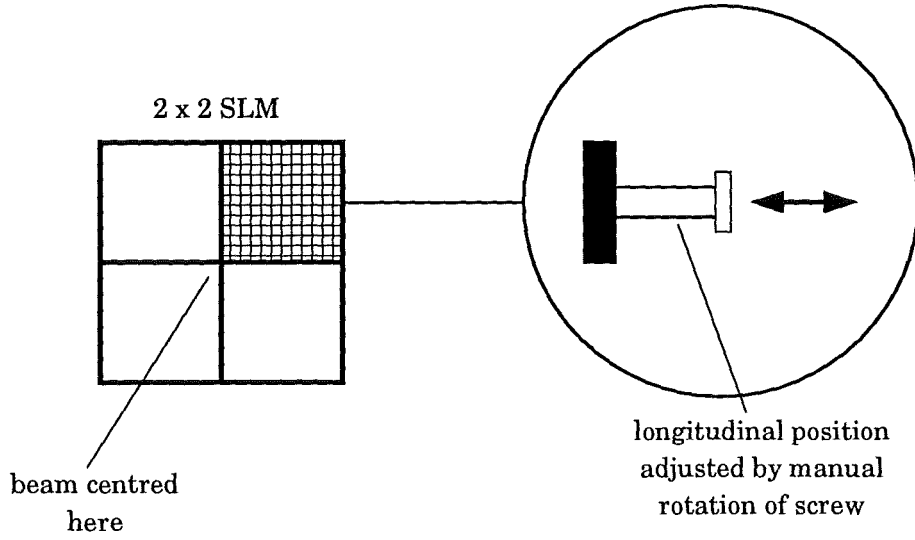


Figure 4.2: A schematic diagram of a mechanically addressed, mechanical phase modulating MMW QO SLM.

quantity and can therefore be accurately modelled. The addressing mode is in fact neither of the two mentioned earlier, but is mechanical. By *mechanical* a number of possibilities are implied, but all generally have the inherent restriction that the modulation rate is slow. The main advantages to be gained by using this addressing mode are again the simplicity of design and construction as well as the inherent low cost. Two approaches have been taken. Firstly a 2×2 (4 pixels) MMW QO SLM has been built that is comprised of four square mirror elements. Each element can be longitudinally displaced from its neighbors by means of a screw thread and dowel guides located behind each of the mirror elements. Figure 4.2 shows this schematically. Secondly a set of fixed form mirrors have been built that enable greater spatial resolution than that of the 2×2 SLM. The addressing is accomplished by manual replacement of the mirrors. A set of five mirrors has been produced and these are schematically depicted in figure 4.3. They were designed with a view to exploring their modulating properties in one dimension only. Figures 4.3(b)–(d) represent an attempt to produce specific Gaussian beam mode converters; viz. (b) a first order mode converter, (c) a second order mode converter and (d) a third order mode converter. The two parameters given are λ the wavelength of the electromagnetic beam in free space and ω the beam width of the MMW QO beam at the mirror surface. The values of ω and $\frac{\sqrt{3}}{2}\omega$ which

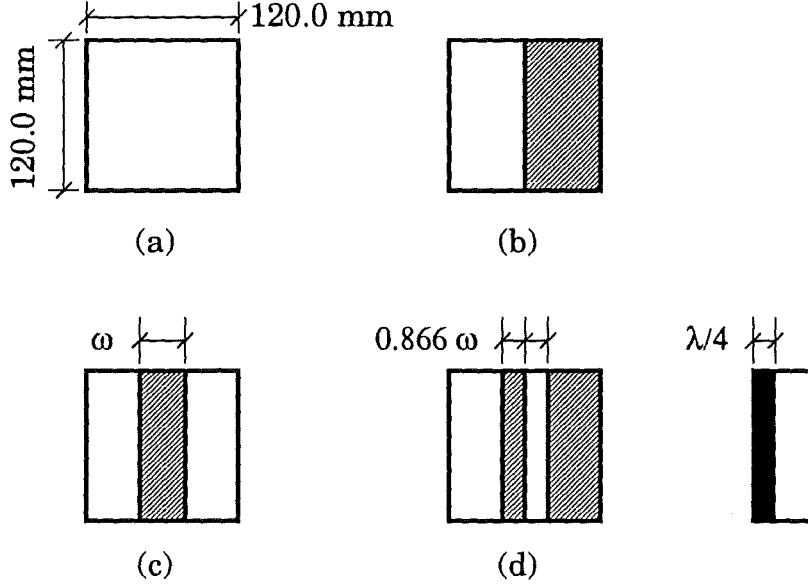


Figure 4.3: A set of fixed mechanical phase modulating MMW QO SLMs.

are given for the channel widths in (c) and (d) were derived by solving the beam mode polynomials—see Lesurf[2, appendix 1]. Thus, for (c) the second order mode converter, π radian phase changes must occur at two positions which are defined by the zeros of the second order Hermite polynomial

$$\mathcal{H}_2(t) = 4t^2 - 2 \quad (4.1)$$

where $t = x\sqrt{2}/\omega_x$ and ω_x is the beamwidth radius at some position z along the beam, and in the x direction. Thus

$$4 \left(\frac{x\sqrt{2}}{\omega_x} \right)^2 - 2 = 0$$

$$x = \pm \frac{\omega_x}{2}$$

and so the width of the recessed surface is ω_x . Similarly for (d), the third order mode converter, the zeros of the third order Hermite polynomial must be found

$$\mathcal{H}_3(t) = 8t^3 - 12t \quad (4.2)$$

where again $t = x\sqrt{2}/\omega_x$. Thus

$$8 \left(\frac{x\sqrt{2}}{\omega_x} \right)^3 - 12 \left(\frac{x\sqrt{2}}{\omega_x} \right) = 0$$

$$x = \pm \frac{\sqrt{3}}{2} \omega_x, \quad x \neq 0$$

and the three solutions for x are $0, \pm \frac{\sqrt{3}}{2}\omega_x$.

Section 4.3.1 describes the optical circuit design, from which ω_x can be determined. The kind of SLM described here operates in a reflection mode, that is, the *reflected* beam has the phase modulation imposed upon it. Therefore separation of input and output beams must be achieved in some way or other and section 4.3.1.1 describes how this aspect has been tackled.

4.1.3 Future Directions for MMW QO SLMs

There are a number of directions that could be taken in the development of future MMW QO SLMs, and the ones explored would have differing limitations and advantages. For example, alternative modulating mechanisms could be explored, such as:

- A fixed set of *transmission* mode plates could be made from, for example, PTFE[3], each having a profile for a specific phase imposition across a beam.
- Polarisation active liquid crystal technology could be explored—see section 2.2.6.

The addressing mode could be explored, and for example:

- A mechanical SLM could have individual elements driven by fast piezo-electric crystals, (i.e. fast electrical addressing).
- A metallised plastic film (e.g. Al on mylar) could be electrostatically deformed by an array of pins.

Finally, there is always the possibility of using a number of SLMs simultaneously on a beam suitably split. This might be desirable if the aim of a given system is to analyse the *mode content* of a beam.

4.2 Radiation Pattern Measurement Issues

There are standard test procedures that have been developed over the years for antenna radiation pattern measurements[4, 5]. Balanis[6] gives a helpful though brief description of antenna measurement procedure. Antenna range instrumentation can be classified into five categories[6, page 711]:

1. Source antenna and transmitting system

2. Receiving system
3. Positioning system
4. Recording system
5. Data processing system

Varying degrees of automation within each of these categories can be implemented. The first category will be dealt with in the following section, suffice to say at this stage, that at a given point in space, an effective radiating aperture of less than 15 mm in diameter is produced. It is the radiation pattern of this *effective source aperture* that is to be measured. Figure 4.4 depicts schematically the experimental setup developed for the measurement of the radiation patterns of MMW QO beam profiles. Note that the millimetre wave absorber positioned behind the receiver intercepted and effectively absorbed all of the output beam, except of course for the small part collected by the receiver. A full anechoic chamber facility was thus not thought to be necessary for this arrangement. Each of the remaining four categories will now be described with reference to figure 4.4.

4.2.1 The Receiving System

The receiving system comprises:

1. A receive antenna
2. A detector
3. Two stages of pre-amplification
4. A bandpass filter
5. A lock-in amplifier

The receive antenna was chosen to be substantially¹ polarisation insensitive. It is a circular, smooth-walled feedhorn, suitable for frequencies above about 70 GHz. From the dimensions of the feedhorn as shown in figure 4.5, the half-power beam widths (HPBW) in both the H-plane and E-plane can be estimated[8]. The two main parameters of interest are the external aperture diameter in wavelengths d/λ , and the length

¹See chapter 5, table 5.2.

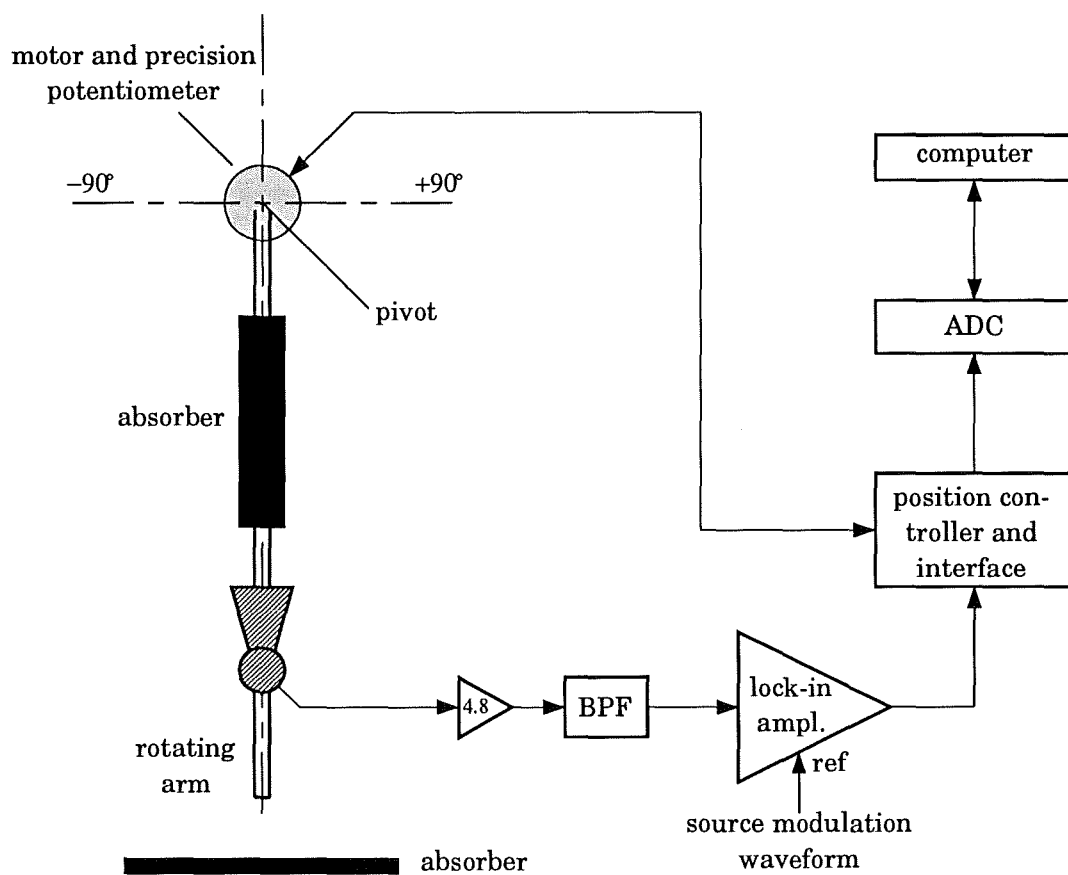


Figure 4.4: A schematic diagram of the radiation pattern measurement setup.

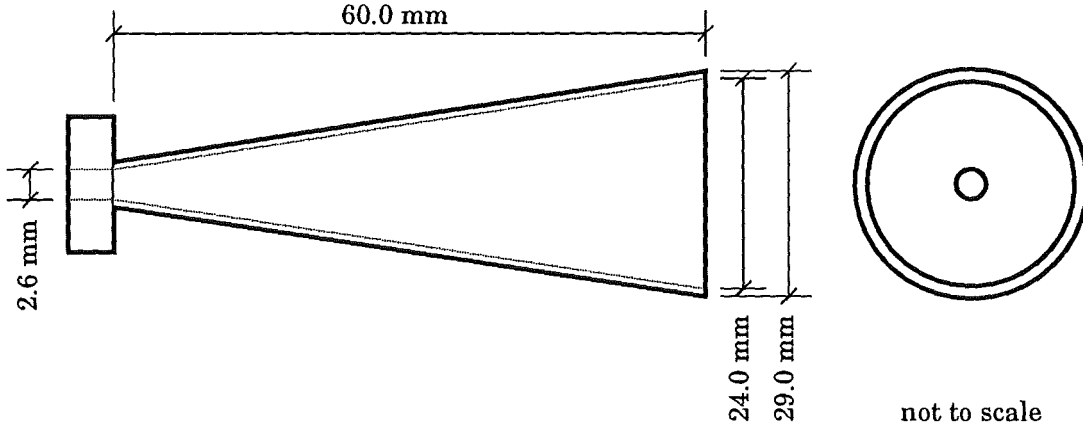


Figure 4.5: A schematic diagram of the receive antenna, a smooth-walled feedhorn.

of the cone in wavelengths L/λ . The wavelength used throughout this work is 3.32 mm and corresponds to a frequency of 90.0 GHz. For the horn here

$$\begin{aligned}\frac{d}{\lambda} &= 7.3 \\ \frac{L}{\lambda} &= 18.2\end{aligned}$$

and thus from reference [8] the gain is

$$G = 25 \text{ dB}$$

Also the horn parameters appear to be optimally configured. The HPBW's in the two planes are

$$\begin{aligned}\Theta_H &= \frac{70}{(d/\lambda)} = 9.6^\circ \\ \Theta_E &= \frac{60}{(d/\lambda)} = 8.2^\circ\end{aligned}$$

The effective aperture area is 52% of the physical aperture area. The H-plane radiation pattern has in fact been measured and is given in figure 4.6. The phase-centre of the horn antenna was estimated² as lying at about 23 mm behind (i.e. inside) the horn's aperture[9]. This phase-centre was positioned directly over the pivot of the radiation pattern measurement system. The experimentally determined H-plane HPBW is 10.5°. (Note that the 0.9° increase compared to the theoretical estimate could be accounted for by the small asymmetrical irregularity at the +5° part of the pattern.)

²Reference [9] deals with square apertures and the results are thus only approximately valid for the circular aperture considered here.

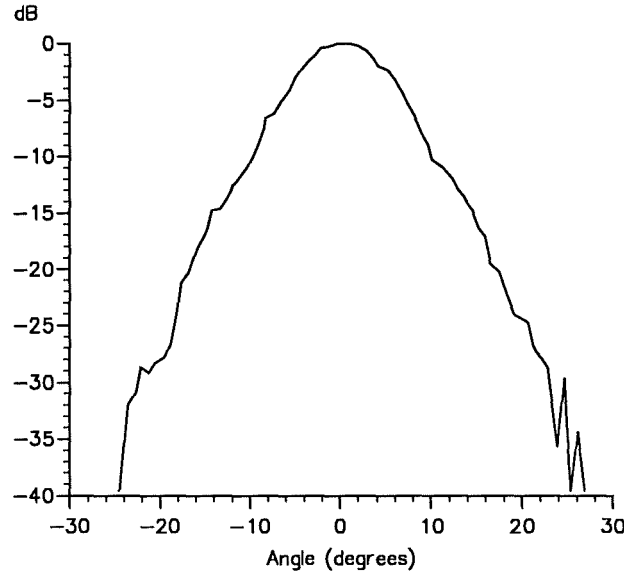


Figure 4.6: The H-plane radiation pattern of the circular smooth-walled feedhorn used with the pyroelectric detector.

A pyroelectric detector was developed specifically for this experiment, and is described within chapter 5. This detector has a minimum NEP of about $30\text{nWHz}^{-1/2}$ at a modulation rate of 20 Hz. It is low-cost, robust and simple-to-use detector. A photograph of the receive antenna and the detector is shown in figure 4.7. The antenna/detector assembly is held in place by a cylindrically machined nylon mount.

The first stage of preamplification (voltage gain of 4.8) forms an integral part of the detector circuitry. The second stage incorporates a bandpass filter (BPF) that is principally employed to reduce the noise transmitted to the following stages. Typical settings for this second stage are:

- voltage gain = 30
- low-pass cutoff = 0.5 Hz
- high-pass cutoff = 100 Hz

for a modulation rate of typically 30 Hz (square-wave). The lock-in amplifier was a Bentham 223 (200 series) which was typically used with a sensitivity setting of 100 mV per 10 V output, and a time constant of 300 ms.

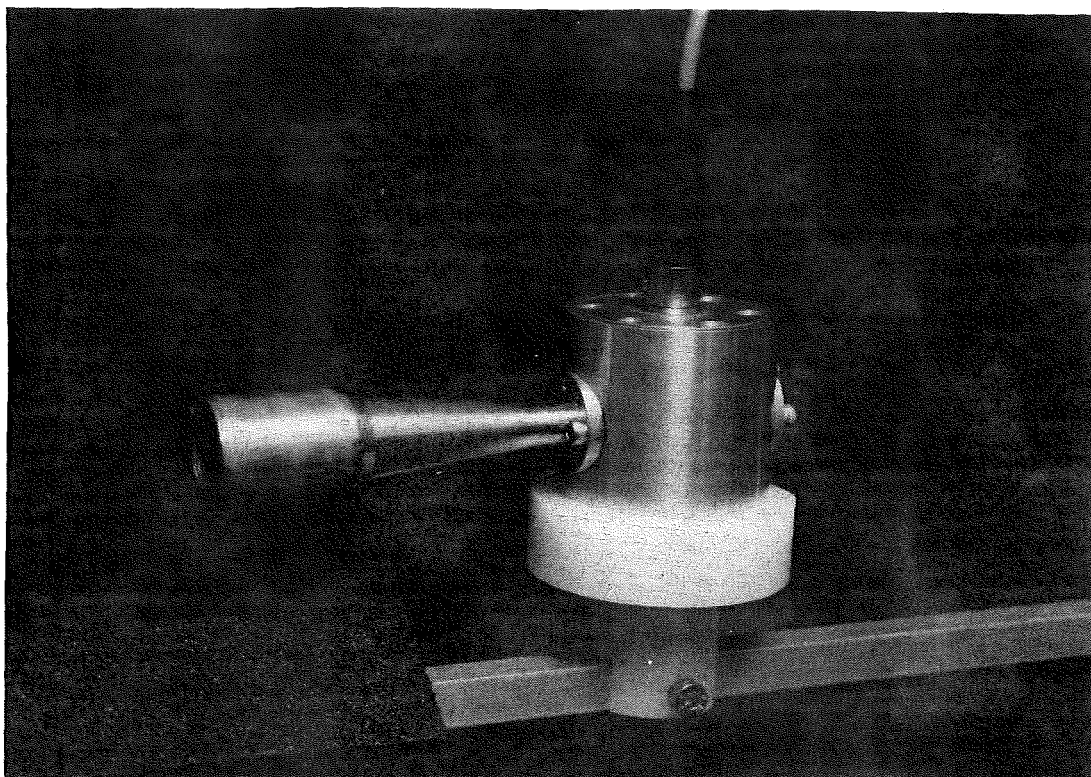


Figure 4.7: A photograph of the receive antenna and detector mounted on the rotating arm.

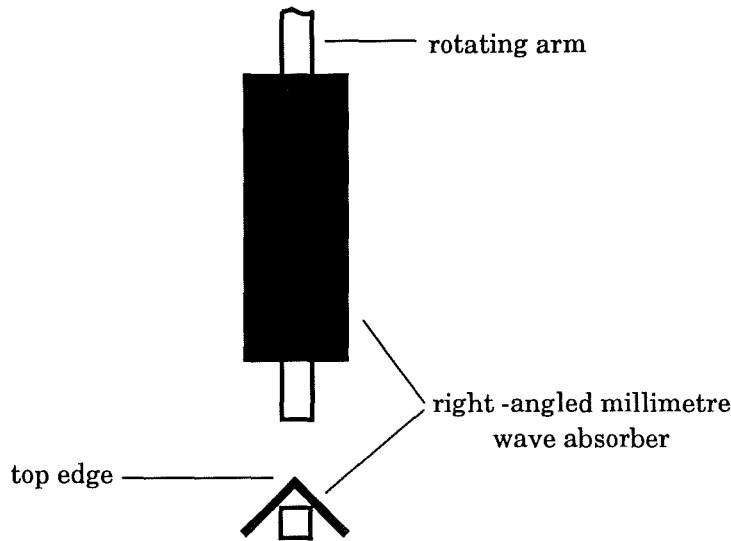


Figure 4.8: Millimetre wave absorber material covering the rotating arm.

4.2.2 The Positioning System

The main elements included within the positioning system are:

1. The rotating arm
2. A precision dc servo system
3. The position controller and interface electronics

Each of these elements is described in some detail below.

4.2.2.1 The Rotating Arm

The rotating arm is a 500 mm length of 9.5 mm square section of aluminium rod. In order to avoid corrupting the measured patterns by the close proximity of the rotating arm and the consequent reflections into the receive antenna, a right-angled piece of millimetre wave absorber was placed over the arm in the manner shown in figure 4.8. Any reflections into the receive antenna must now originate from specular reflection off of a right-angled *edge* of millimetre wave absorber material. The amount of reflection will be very small and probably not measurable with the available system sensitivities.

The receive antenna and detector assembly can be positioned at any point along the rotating arm. The position at which the receive antenna should be placed depends

upon a number of issues. Simply stated, the receive antenna must be within the far-field of the test source—here an effective source aperture—and this normally means at a distance r such that

$$r > \frac{2D^2}{\lambda} \quad (4.3)$$

where D is the diameter of the test source, and λ is the free space wavelength of the electromagnetic beam. In this situation, D is the diameter of an effective source aperture and is ≤ 15 mm. However, there are a few subtleties involved that require some attention. Reference [5, pages 18–20] describes the issues relevant here. There are three issues to be investigated and they are

1. The effect of mutual coupling between the source and the receive antenna.
2. The effect of a transverse amplitude taper of the receive antenna's pattern at the effective source aperture.
3. The effect of the phase variation of the receive antenna's pattern at the effective source aperture.

The minimum acceptable distance r between the receive antenna and the source aperture can be determined from a consideration of each of the above three effects. The effect of reflections (multipath) is not included here and is assumed to have been adequately eliminated with the various millimetre wave absorbers used within the system.

Mutual Coupling between the source aperture and the receive antenna is for most situations very low, but even so it may still cause measurable errors in the level of the signal observed near the peak of the effective source aperture's major lobe or lobes. In order to ensure that this effect is negligible, it is considered good practise to have the ratio of the plane angle δ , subtended at the receive antenna by the diameter of the effective source aperture, to the HPBW, Θ of the receive antenna, to be made less than or equal to 0.3—see figure 4.9. This ratio corresponds to a subtended angle at the source aperture of the receive antenna's pattern that is approximately equal to the beamwidth of the receive antenna at the 0.25 dB level, (i.e. a 0.25 dB amplitude taper). The angle δ is given by

$$\delta = 2 \sin^{-1} \left(\frac{D}{2r} \right) \quad (4.4)$$

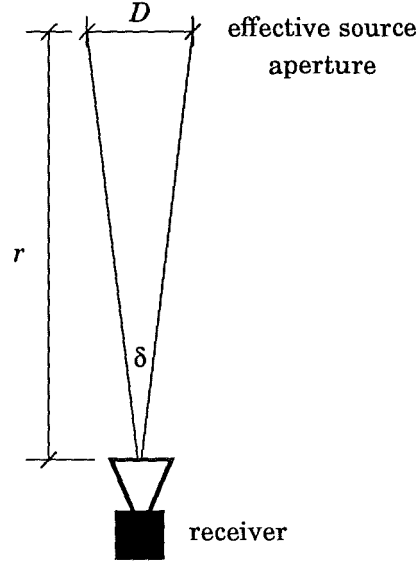


Figure 4.9: Basic source aperture and receive antenna geometry.

and the HPBW Θ for the receive antenna was measured³ to be 10.5° . Therefore with $D \leq 15$ mm, and r typically set at 300 mm,

$$\frac{\delta}{\Theta} = 0.27 < 0.3 \quad (4.5)$$

Transverse Amplitude Taper An amplitude taper for the receive antenna's pattern can produce an error in the measured pattern of the source aperture. The effect is dependent upon the aperture excitation function at the source aperture. For typical excitation functions, the effect of the amplitude taper is a broadening of the main pattern lobe, with a slight modification to the close-in side lobes. The beam broadening can be viewed as a reduction in directivity, and so for example, if the amplitude taper varies to -0.25 dB at the *edge* of the source aperture, typically a reduction in directivity of 0.1 dB would be measured. The 0.25 dB taper criterion for the receive antenna's pattern at the source aperture will generally yield acceptable pattern measurement accuracy.

Phase Variation In the absence of reflections, the 0.25 dB criterion for the amplitude variation of the receive antenna's pattern over the source aperture gives a corresponding phase variation that will be very close to that of a spherical wave apparently emanating

³See page 55.

from the phase centre of the receive antenna. It can be shown[7] that for a source aperture diameter D and a separation r , the phase deviation $\Delta\phi$ will be given by

$$\Delta\phi \approx \frac{\pi D^2}{4\lambda r} \quad (4.6)$$

A commonly employed criterion for determining the minimum allowable separation between the source aperture and the receive antenna, is to restrict $\Delta\phi$ to $\pi/8$ radians. This results in the restriction that

$$r \geq \frac{2D^2}{\lambda} \quad (4.7)$$

This is the far-field criterion typically used and quoted earlier in equation 4.3. The effect of a phase variation across an aperture is that nulls of the pattern are partially filled and that the amplitude of the side lobes is changed⁴. If D is taken as 15 mm, then this criterion yields the result

$$r \geq 136 \text{ mm} \quad (4.8)$$

for $\lambda = 3.32$ mm, (i.e. frequency $f = 90.0$ GHz). For all experiments, r has been typically set at some distance greater than or equal to 300 mm.

4.2.2.2 The Precision DC Servo System

The rotating arm is attached to a low-profile mount that incorporates a simple bearing arrangement. It's total height above the optical table is 13 mm. This height is sufficiently lower than the optical axis—height of 60.0 mm—for there to be negligible effect on the beam. The mount provides for $180^\circ(\pm 90^\circ)$ rotational movement of the arm in the horizontal plane. The pivot point of the arm is attached via a shaft to the precision dc servo system mounted *below* the optical table. Figure 4.10 provides a photograph of this assembly.

The precision dc servo system has three main elements:

1. A precision dc servo motor
2. A precision motor gearbox
3. A precision servo mount potentiometer

⁴See figure 3 in reference [5, page 21].

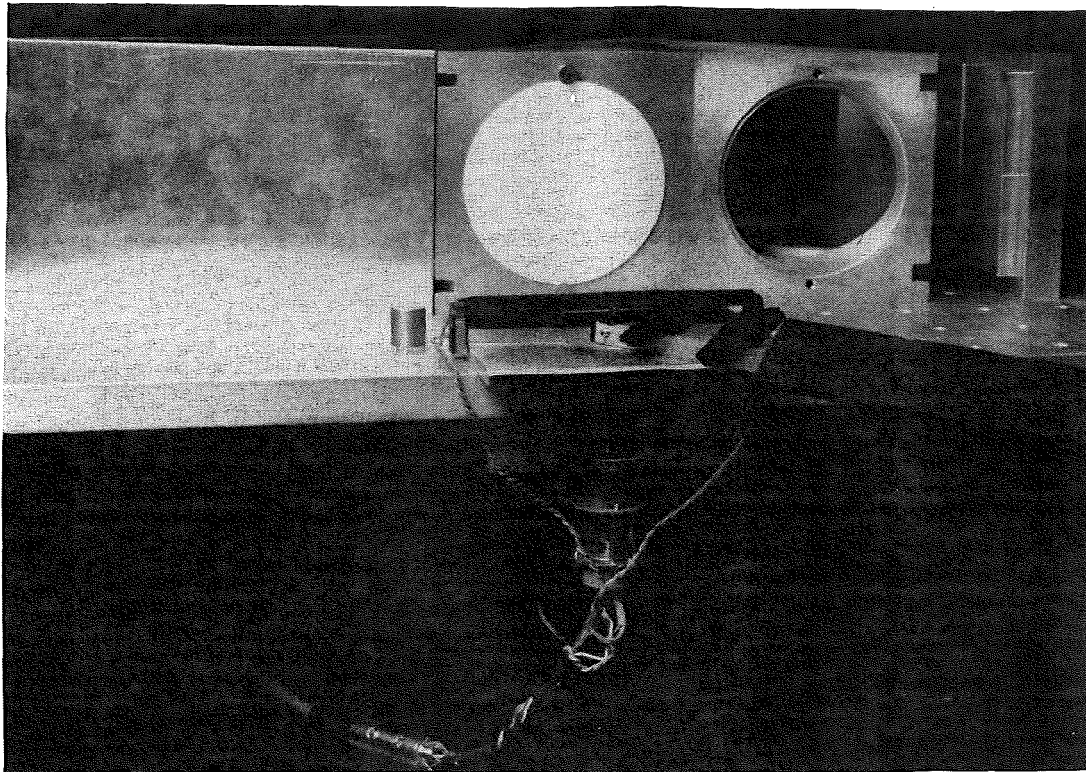


Figure 4.10: A photograph of the rotating arm, it's mount, and the precision dc servo system located below the optical table.

The whole system was designed by the supplier⁵ to work as an integrated system. The motor speed and gearbox ratio were chosen so as to provide for a slow, smooth and well controlled movement of the arm. The arm could rotate 180° in at most about 15 seconds, but rotation times more like 1–2 minutes were most often used. The potentiometer used is a screened conductive plastic device. It was trimmed by the supplier to provide high linearity. The total resistance value was chosen to be 2k Ω and the linearity was $\pm 0.5\%$. Two servo bearings are incorporated, thus providing for low torque rotation and long life. A common shielded cable is used to carry both the motor drive current and the potentiometer voltages to the control electronics contained within the *position controller and interface box* shown in figure 4.4.

4.2.2.3 The Position Controller and Interface Electronics

The electronics was designed to provide for three main functions:

1. Electrical power for the motor, with
 - (a) Direction control
 - (b) Speed control
 - (c) Limits on extent of powered rotational movement
2. Angular position reference voltage
3. Pattern signal level adjustment

The first two functions also required various power supplies. For the sake of convenience these power supplies were constructed and integrated within the whole electronics subsystem. A circuit diagram of the motor electronics is shown in figure 4.11. Control of the direction of rotation for the motor is achieved with the use of a ganged multi-pole rotary switch. Speed control is obtained with a simple high power potentiometer. The limits of rotational movement are set by physical endstops—the rotating arm can move no further than $\pm 90^\circ$. In order to protect the motor, the gears and the electronics, two microswitches are used at the endstops to cut off the motor's power supply, once the rotating arm activates either of them. When a microswitch is activated, it switches a control line to ground, which then deactivates the relay supplying power to the motor.

⁵RS Components Limited.

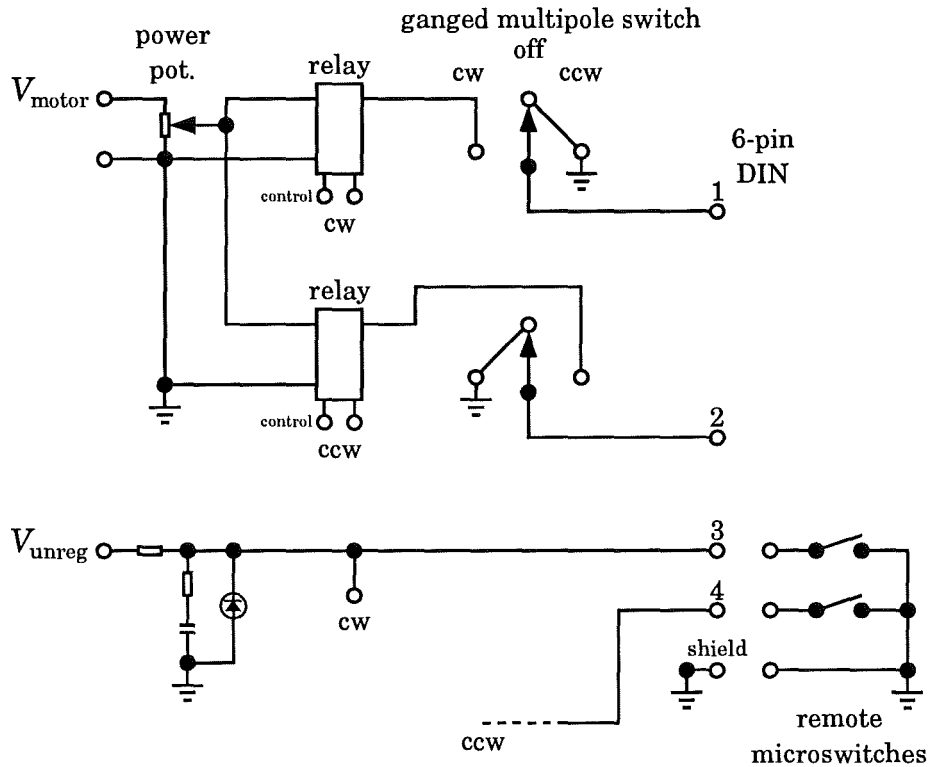


Figure 4.11: The motor control circuit diagram.

Only the microswitch *to* which the rotating arm is moving can shut off the power to the motor. This microswitch control could form the basis of an automated computer controlled positioning system.

The angular position electronics is shown in figure 4.12 and involves the supply of a reference voltage V_{ref} to the precision servo potentiometer. Only 180° of the 340° total electrical rotation available is used. This has a significant bearing on the choice of V_{ref} . Ideally the same V_{ref} as that used by the analogue-to-digital converter (ADC) should be used here, but this immediately means that only about one half of the potential dynamic range is used, (i.e. a 3 dB loss). An internally generated V_{ref} allows the voltage at the precision potentiometer to be adjusted for maximum dynamic range. The argument for using the ADC's V_{ref} is that noise on this V_{ref} and on the input signal to the ADC would be common, (i.e. coherent), and so eliminated in the ADC conversion process. This normally results in an improved dynamic range performance. This is not true for the internally provided V_{ref} . Both arrangements are possible, the

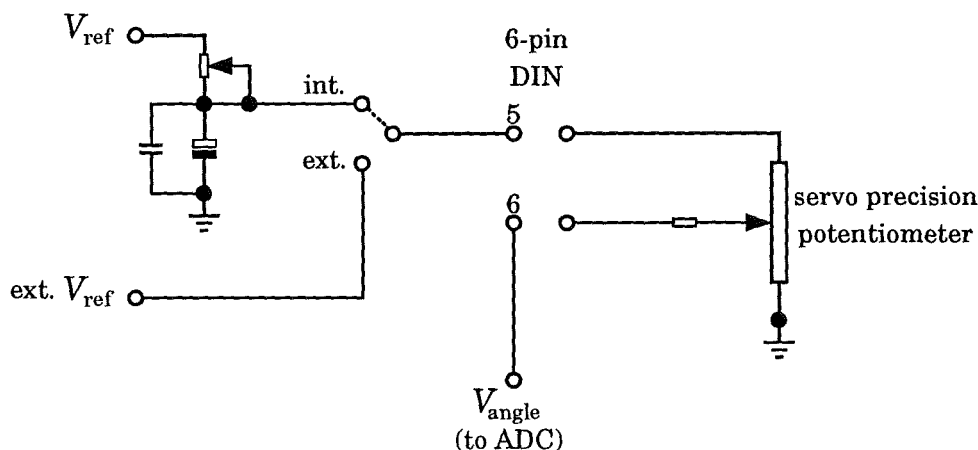


Figure 4.12: A diagram of the angular position measurement circuit.

preferred one being selected by a switch. There are other ways that the dynamic range could be increased. For example the angular position voltage could be allowed to swing positive and negative, thus doubling the dynamic range, and for the pattern signal, a logarithmic amplifier could be incorporated.

Adjustment of the pattern signal level was achieved simply with the use of a potentiometer. This trimming facility was helpful for maximising the available dynamic range for any given pattern measurement.

4.2.3 The Recording and Data Processing Systems

The level of automation for this radiation pattern measurement facility was chosen to include only *data acquisition* and *display*. A greater degree of automation would have involved much more effort and time and was not thought to be necessary for the application intended here. However, the automatic acquisition of data and its real-time display, greatly enhance the speed at which pattern measurements can be made; it allows real-time processing to be accomplished, such as the removal of mechanical hysteresis in the shaft connections via calibration; and it produces data in a form immediately suitable for subsequent data processing, (e.g. direct comparisons with theoretical model results and enhanced graphical display).

Harvey[10, chapter 5] developed the ADC and ADC communication and control hardware. The computer used is an ACORN Archimedes 310⁶, ideally suited to this

⁶ACORN and Archimedes are trademarks of ACORN Computers Limited.

kind of application. The software, (entitled RADPAT), was written in BBC BASIC V and is listed within appendix A. One assembly code procedure was entirely written by Harvey—PROCadcread, and a first draft of this RADPAT code was developed by Leeson⁷. Leeson went on to develop a code specifically for his own situation, (it included the use of a programmable logarithmic amplifier[11]). The development of RADPAT involved a substantial enhancement of Leeson's original code, including the incorporation of an algorithm for measuring and eliminating by calibration, the residual hysteresis in the pivot shaft connections to the rotating arm and to the central shaft of the servo system. The amount of residual hysteresis was of the order of 2° – 3° .

RADPAT uses an array to store up to four patterns at any one time. This allows for the scanning of a reference pattern in both directions, and for the scanning of a modulated pattern in both directions. This set of four patterns can be displayed, printed out, stored, and read back in as a single entity. RADPAT is a menu driven program and is simple to use. The real-time display is in the form of a rectangular pattern plot and a digital readout. The digital readout is useful for monitoring the adjustment of the maximum pattern signal level prior to the measurement of a pattern. The screen patterns can be screen-dumped to a dot-matrix printer for a hardcopy record. The patterns can be stored on disc as **Basic data** files and as **ASCII** files. The **ASCII** file format is provided so that transfer of readable data to a local **Sun Workstation**⁸ village is possible. An RS423 serial link is used make the transfer. It is upon a **SUN Workstation** that the theoretically derived data is generated, and upon which enhanced graphical display is possible.

4.3 The MMW QO Circuit

4.3.1 Circuit Description

4.3.1.1 Components and Configuration

The purpose of the millimetre wave quasi-optical circuit described here is to provide a means for both producing and projecting a quasi-optical beam that has the modulation from an SLM imposed upon it. The circuit imposes the modulation upon a fundamental

⁷The code was named BEAM, was written in August 1991, and was written for the BBC Master Computer. It used the BBC's integrated ADC.

⁸Sun Workstation is a registered trademark of Sun Microsystems Incorporated.

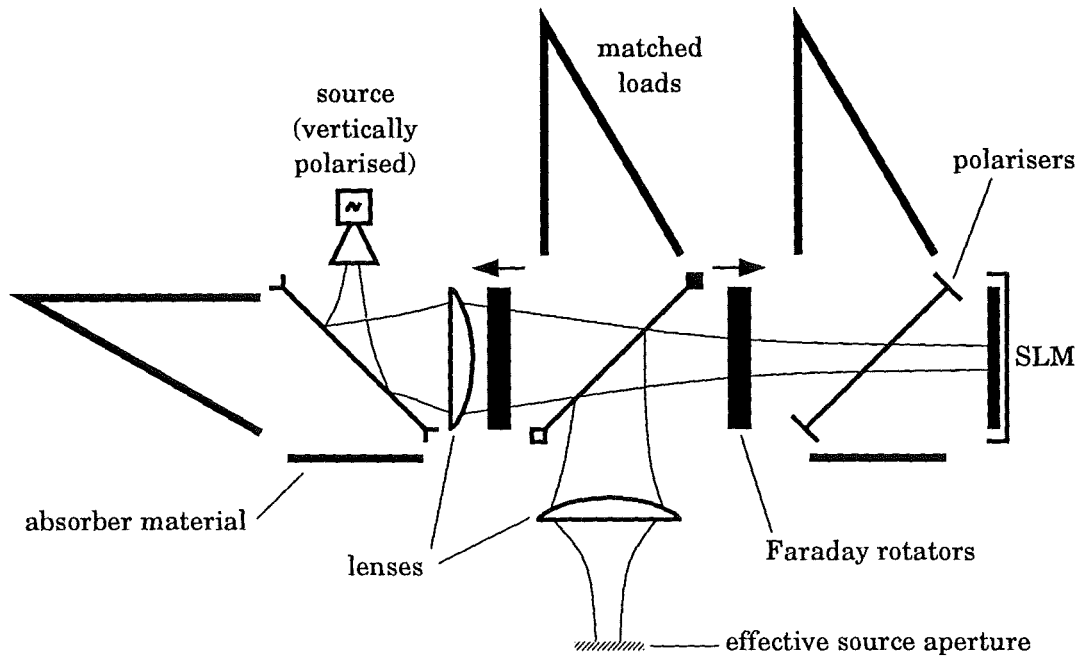


Figure 4.13: The MMW QO generic circuit used to produce and project an SLM modulated beam.

mode beam and then projects the beam into the far-field for the measurement of its radiation pattern. As a part of the projection process, the beam must appear to have a phase centre directly over the pivot position of the radiation pattern measurement system. The effective source aperture at this position must not be too large. It should have a diameter less than about 15 mm. This requirement on the dimension is related to the wavelength λ and the length of the rotating arm. Figure 4.13 depicts the generic circuit used to perform the required function. The source is a mechanically tunable Gunn diode oscillator set to 90.0 GHz[12]. A TK⁹ scalar feedhorn is used to produce a 98% (power) pure fundamental mode beam[13]. The polarisers employ a grid of tungsten wires to accomplish linear polarisation splitting of beams passing through them[10, §4.4]. The tungsten wire used is usually 25 μm in diameter and the spacing is also 25 μm . The lenses were manufactured from PTFE and the phase-matching procedure used to determine the required lens profile is described in reference [12, pages 176–182]. The matched loads exhibited return losses better than 40 dB[14]. The

⁹TK is a trademark of Thomas Keating Limited.

45° Faraday polarisation rotators are described in detail in chapter 6. Essentially they are large ferrite sheets—see section 6.2—that have been quarter-wave matched to free space and have the property that they rotate the plane of polarisation of a linearly polarised incident beam through 45° clockwise about the arrow shown in the symbol in figure 4.13. It is by means of this anisotropic polarisation rotating function in co-operation with a polariser that the beam incident upon the SLM and the beam reflected from the SLM are isolated from one another.

The mechanical construction is modular in nature—see reference [10, chapter 4]—and this means that changes to the circuit layout and function can be made very easily.

In order to understand the way in which the circuit functions, consider the vertically polarised fundamental mode beam produced at the source. This beam has a small effective beam waist at the feedhorn and so rapidly diverges as it propagates towards the first lens. The beam is reflected from the first polariser to the lens. Any cross-polar components produced by the feedhorn pass through the polariser and are absorbed by the millimetre wave absorber material. The first lens re-forms the beam's phase-front in such a way that the emergent beam's phase-front has a large and negative curvature, and slowly converges to a beam-waist at the SLM plane before slowly diverging back toward the second lens. The first Faraday rotator rotates the beam's plane of polarisation so that it almost completely¹⁰ passes through the second polariser. This first Faraday rotator thus quasi-optically isolates the source from the remainder of the circuit and thus the source *sees* a load with a constant and closely matched impedance. The second Faraday rotator rotates the plane of polarisation back to the vertical and then the beam passes through the third polariser. The polarisation of the beam as it encounters the SLM is thus vertical. The reflected beam is essentially vertically polarised—any cross-polar component will be reflected by the third polariser into the millimetre wave absorber material. After once again passing through the Faraday rotator, the beam will emerge with a polarisation state orthogonal to that which it had at the same point in the circuit when it was propagating in its initial direction. The beam is thus reflected by this central polariser out through the second lens. This second lens, identical to the first, re-forms the phase-front so that it emerges with a smaller and negative radius of curvature. The beam now rapidly converges to beam-waist located above the pivot position of the radiation pattern measurement system. The polarisation state of the

¹⁰Except for a small amount absorbed within the ferrite (see section 6.2).

beam as it is now allowed to propagate into the far-field, is at 45° to the vertical.

The spatial distribution of power in the beam is only altered significantly by the SLM. There is some distortion arising from absorption in the lenses and the Faraday rotators, and the level of this distortion is shown within section 4.4.3.

For the circuit configured with the specific configuration shown in figure 4.13, the radiation pattern is measured in the H-plane, and with the polarisation processing shown, it is the 1-dimensional co-polar H-plane pattern that is measured. Cross-polar and E-plane patterns could be measured with suitable modification to the circuit.

4.3.1.2 Variation of the Source Aperture Position

If the effective source aperture produced by the quasi-optical circuit described above does not lie directly above the pivot point of the radiation pattern measurement system, then the measured pattern will have some error superimposed upon it. A correction factor is derived within this section for application to measured patterns. This correction factor relies upon having knowledge of the true position of the effective source aperture relative to the position of the pivot point. If accurate knowledge of the true position of the effective source aperture is not available, then an *estimate* of the error in the pattern may still be able to be determined for various possible positions of the aperture.

The derivation begins by considering the power transmission formula, or as it sometimes called, the communication link formula, viz.

$$P_R = P_T \frac{G_R G_T \lambda^2}{(4\pi r)^2} \quad (4.9)$$

where P_R and P_T are the received and transmitted powers respectively, and G_R and G_T are the gains of the receive antenna and source aperture respectively. The distance between the source and the receiver is r and λ is the free space wavelength. Impedance mismatch is assumed to be negligible, and polarisation mismatch irrelevant to the discussion, (and in any case, constant).

As the receive antenna is always pointing in the same direction along the rotating arm to the pivot point, G_R is assumed to be constant—see section 4.2.2.1. However G_T is a function of angular position θ about the pivot point. As the pattern is being measured in only one plane, the other angular co-ordinate is constant. The gain and the directivity as functions of θ are equivalent, because there is no significant loss

mechanism at the place of the effective source aperture. Therefore

$$D(\theta) = \frac{G(\theta)}{e} = G(\theta) \quad (4.10)$$

If the true position of the source is defined by the distance r_s between the source and the receive antenna, and if the pivot point is at distance r_p from the receive antenna, then from equation 4.9 the radiation pattern $D(\theta)$ is given by

$$D(\theta) = \frac{r^2(\theta) P_R(\theta)}{\kappa} \quad (4.11)$$

where κ is a constant and is given by

$$\kappa = \frac{P_T G_R \lambda^2}{(4\pi)^2} \quad (4.12)$$

Thus

$$\begin{aligned} D(\theta) &= \frac{r^2(\theta)}{r_p^2} \frac{P_R(\theta) r_p^2}{\kappa} \\ &= \frac{r^2(\theta)}{r_p^2} D'(\theta) \end{aligned} \quad (4.13)$$

since $P_R(\theta)$ is the power received on an arc of a circle of radius r_p and thus $D'(\theta)$ is the *measured* directivity pattern. Therefore the required correction factor is $r^2(\theta)/r_p^2$. Figure 4.14 illustrates the relevant geometry. The distance r_s may be greater or smaller than r_p . Either geometry will yield the required relationship. From figure 4.14

$$r^2(\theta) = r_p^2 + (r_p - r_s)^2 - 2r_p(r_p - r_s) \cos \theta \quad (4.14)$$

and dividing through by r_p^2

$$\frac{r^2(\theta)}{r_p^2} = 1 + \delta^2 - 2\delta \cos \theta \quad (4.15)$$

where

$$\delta = \frac{r_p - r_s}{r_p} \quad (4.16)$$

Equation 4.15 is the correction factor that must be applied to $D'(\theta)$ in order to obtain the true pattern $D(\theta)$. For example, it can be seen that if the relative difference in position of the source with respect to the pivot point is less than say 5% then the error in the pattern will be approximately 3% for θ within $\pm 45^\circ$.

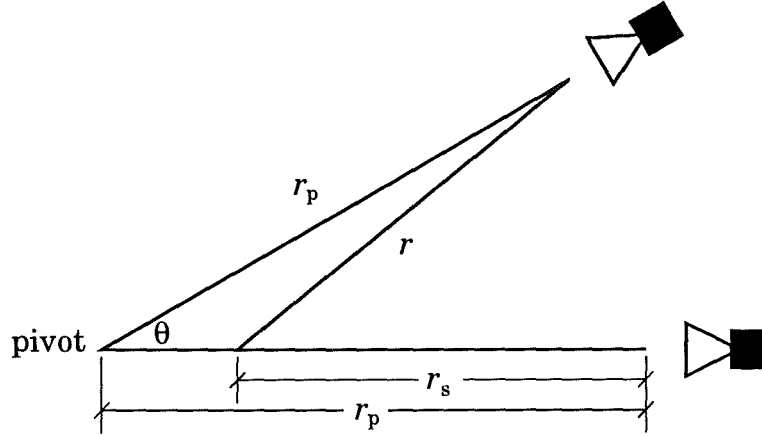


Figure 4.14: The geometry of the pattern measurement set up with the source position not at the pivot point; $r_s < r_p$.

4.3.1.3 Other Issues

Standing Waves within the circuit also have the potential to affect the radiation pattern. Reflection at the SLM plane actually involves reflection from two planes separated by $\lambda/4$. This separation means that the standing wave patterns that can be generated are offset from each other. That is, the reflected, spatially modulated beam will have superimposed upon it a spatially dependent standing wave pattern. Simple standing wave patterns have a period of $\lambda/2$, and so for a $\lambda/4$ separation of the SLM reflection planes, minima in the standing wave pattern from one plane may correspond to maxima from the other plane (i.e. if the simple case approximately applies). Assuming that the reflection surfaces are perfectly conducting, the resultant electric field at the reflection planes is zero for all time. This is true for all practical purposes at millimetre wavelengths. The effect of the different standing wave patterns on the resultant field distribution transmitted through the final lens of the circuit, depends upon the relative positions of the various reflective surfaces within the circuit (i.e. lenses, Faraday rotators and the SLM). In order to minimise the effect of the different standing wave patterns on the radiation pattern, the position of the SLM within the quasi-optical circuit can be varied. Ideally there should be no standing waves within the quasi-optical circuit. They should be minimised and measured and section 4.4.2 provides results from measurements of the standing wave patterns.

Bandwidth considerations have been alluded to within the above discussion on standing waves. The SLM employs a frequency sensitive method of imposing a specific phase distribution upon an incident beam. In addition, the lenses and the Faraday rotator have their surfaces quarter-wave matched to free space. Thus the temporal bandwidth of millimetre wave signals that can be processed through this circuit is limited. If a large bandwidth is required, the circuit could be duplicated a number of times with the frequency sensitive components adjusted for different centre frequencies, and then the various circuits could be multiplexed together. However, for a single circuit the bandwidth will be between 5% and 10%, and at 100 GHz this corresponds to 5–10 GHz, which may well be sufficient for many situations. In fact, a bandwidth of up to 20% may well give satisfactory performance.

Fundamental Mode Purity of the beam incident upon the SLM is important if the comparison of experimental results with the theoretical analysis of chapter 3 is to be meaningful. *Like* must be compared with *like*. If the incident beam is not a purely fundamental mode Gaussian beam, but its mode content is known, then the analytical tools developed within chapter 3 can still be useful. Wylde[13, table 1] shows that the purity of the fundamental mode formed by a corrugated feedhorn is high, at about 98% (power). The next order mode, the first order mode, makes no significant contribution at all. The second order mode makes the next most significant contribution after the fundamental mode, at about 1.45%.

It is likely that the most significant corruption of the almost purely fundamental mode produced by the scalar feedhorn will result from spatially non-uniform absorptions of beam energy by the lenses and the Faraday rotators. Also there will be some mode conversion at each of the apertures which may be significant. About 1% of the beam energy will be lost to higher order modes at each aperture[2, page 39]. Another source of mode conversion is via lost power at the first polariser. At this point in the circuit the beam is rapidly diverging and the vectorial nature of the electric field means that some small fraction of the incident beam energy is lost. This loss is spatially non-uniform, and so may be significant.

4.3.2 QO Beam Parameters

This section describes the quasi-optical beam that propagates through the circuit. The lenses used within the circuit were designed for fundamental mode propagation only, and so the effect of these lenses on multi-mode beams is also assessed.

4.3.2.1 Propagation of the Fundamental Mode Only

A quasi-optical beam is fully characterised by a knowledge of the beam's beam waist size ω_o and the free space wavelength λ . However, if lenses are used to transform the beam's phase-front at some point along the beam, then the output beam has a new beam waist size and the relative positions of the beam waists with respect to the lens, also need to be known. The following description can be viewed in essence as the preliminary analysis of a particular circuit requirement prior to the design of an appropriate lens. It is assumed that the lens is sufficiently far from the beam waists for the beam size ω and the radius of curvature R to not vary significantly over the thickness of the lens, that is the lens is assumed to be *thin*.

To begin with the fundamental mode beam emerging from the scalar feedhorn has an effective beam waist ω_o given by [12, page 172]

$$\omega_o = \left(\frac{20.3}{1 + \frac{0.55}{\lambda^2}} \right)^{\frac{1}{2}} \quad (4.17)$$

where ω_o and λ are in mm, and $\lambda = 3.32$ mm. Thus $\omega_o = 4.40$ mm. Also from reference [12] the position of the beam waist with respect to the feedhorn's aperture is given by

$$z = \frac{46.9}{0.55 + \lambda^2} \quad (4.18)$$

and thus the beam waist is located 4.03 mm from the feedhorn aperture plane, (inside the feedhorn). One of the prime factors to be considered in the design of real quasi-optical circuits, is the aperture size through which beams are to propagate. Lesurf[2, page 39] shows that if the aperture diameter is ≥ 3 times the beam size (radius) at the aperture plane, then 98.9% of the power in a fundamental mode beam is transmitted through the aperture. This corresponds to a loss of < 0.05 dB. The aperture diameter of the optics employed is 80 mm [10, chapter 4]. This means that the maximum beam size at such an aperture—where typically a lens might be mounted—is $\omega_a = 80/3 \approx 26$ mm. Therefore the reduced dimensionless position of this aperture with respect to

the position of the beam waist at the feedhorn, is given by equation 3.23, that is,

$$\hat{z}_o = \left(\frac{\omega_a^2}{\omega_o^2} - 1 \right)^{\frac{1}{2}} \quad (4.19)$$

and by definition

$$\hat{z}_o = \frac{2z_o}{k\omega_o^2} \quad (4.20)$$

Thus $\hat{z}_o = 5.82$ and $z_o = 106$ mm. The radius of curvature R_a of the incident beam's phase-front is given by

$$R_a = \frac{k\omega_a^2}{2\hat{z}_o} \quad (4.21)$$

and thus $R_a = 110$ mm. If the lens is to transform the beam into a pseudo-parallel beam, with a beam waist at the maximum possible distance from the lens aperture (called a *maximum throw* configuration) then this occurs for a beam emerging from the lens with a radius of curvature $\bar{R} = -1$ (\bar{R} is the radius of curvature referred to the beam size at the lens aperture). This corresponds to an emergent radius of curvature $R' = -k\omega_a^2/2 = -638$ mm. For the new beam waist, $\omega'_o = \omega_a/\sqrt{2} = 18.4$ mm and it's position with respect to the lens aperture is $\bar{z} = \frac{1}{2}$ or $z'_o = k\omega_a^2/4 = 319$ mm. The beam is thus fully described by the parameters $(\omega_o, z_o, \omega'_o, z'_o)$. The function of the lens at the (ω_a, R_a) plane would be to transform an incident beam's radius of curvature of 110 mm (divergent) to a transmitted beam with a radius of curvature of -638 mm (convergent). References [12, 10] provide a detailed description of the phase-matching procedure used for the design of the lens¹¹.

Ideally the SLM should be placed at the beam waist of the pseudo-parallel beam and the lens to lens spacing should be $2z'_o$. The beam waist of the feedhorn should be at z_o from the lens. All positions are with respect to the (ω_a, R_a) aperture plane. The planar surface of the plano-convex lens is also normally placed within this plane and the planar surface of the lens should face the feedhorn[10, page 46]. This minimises standing wave phenomena and pattern distortion.

4.3.2.2 Multi-mode Propagation

The PTFE lenses used were designed for quasi-optical circuits that employ only fundamental mode beams. In order to understand the effect of the lens on higher order modes, the procedure used for designing the lenses needs to be understood. A phase-matching

¹¹The lenses actually used were designed by Dr. Graham Smith, and constructed from PTFE.

technique has been used to design the lenses used here. This technique involves equating all of the electrical path lengths (i.e. phase lengths) from an *input* beam to an *output* beam, through the lens; that is the lens profile that provides for equal phase lengths from an input beam waist to an output beam waist, is evaluated. This phase-matching technique incorporates the anomolous phase terms for the fundamental mode input and output beams. These terms are of the form

$$\Phi_{00} = \tan^{-1} \hat{z} \quad (4.22)$$

where Φ_{00} represents the fundamental mode's anomolous phase term. For higher order modes, the anomolous phase terms have the form

$$\Phi_{mn} = (m + n + 1) \tan^{-1} \hat{z} \quad (4.23)$$

It is the significance of these higher order mode anomolous phase terms within the phase-matching design process that needs to be assessed. As a result of their exclusion from the design process—there is no meaningful way to include them for a multi-mode beam in any case—the output radii of curvature for the higher order modes would be unequal and thus the output beam waist positions and sizes for the higher order modes would also be different.

Appendix B works through this particular problem for the specific lenses used, and provides an *estimate* of the significance of this effect on the measured radiation patterns. For modes up to Ψ_{55} , or in one dimension only Ψ_{010} say, the variation in output beam waist position is less than 1%. This corresponds to an effect on the measured radiation patterns of less than 0.1 dB.

4.4 System Evaluation

4.4.1 Dynamic Range and Angular Resolution

The dynamic range achieved with this measurement system is > 30 dB (approaches 40 dB). This is adequate for all practical purposes here. It is limited by source power and the post-pyroelectric detection system, (i.e. not the ADC).

The angular resolution is set to a minimum of 0.5° . If the patterns are scanned sufficiently slowly, the actual resolution obtained is $\sim 0.6^\circ$. Greater resolution is possible but the limit with the mechanical arrangement in it's present form is about 0.2° . It is vibration in the arm that gives rise to this limiting condition.

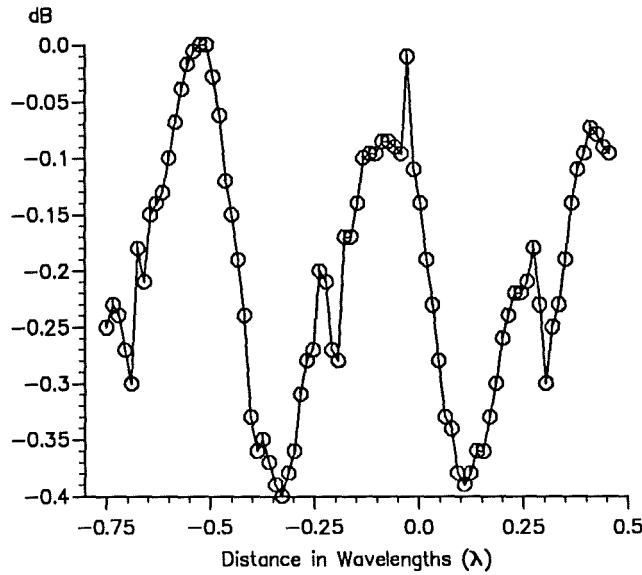


Figure 4.15: The standing wave pattern within the quasi-optical circuit

4.4.2 Standing Waves

Standing waves exist within the quasi-optical circuit. They have been measured by replacing the SLM in the circuit (as shown in figure 4.13) with a plane mirror that can be moved longitudinally along the beam. Power variation was measured in the far-field (on the beam axis) as a function of mirror position. This approach effectively eliminates any standing waves between the pyroelectric detector and the circuit—see section 4.2.2.1. The mirror was moved a total of 4 mm (or 1.2λ); from 2.5 mm beyond the inter-lens beam waist position to 1.5 mm inside this position. Figure 4.15 shows this pattern in decibels against the offset position in wavelengths. The pattern is more complex than that of a transmission line with a single unmatched load, but its period is still $\lambda/2$. There is a maximum variation of 0.4 dB in the pattern. This corresponds to a maximum vswr of around 1.5. This allows for sufficient accuracy in the radiation pattern measurement.

4.4.3 Circuit Imposed Distortions

The quasi-optical circuit imposes distortion upon the fundamental mode beam produced by the scalar feedhorn. The distortion results from the following: spatially non-uniform losses in the circuit; multiple reflections within the lenses and the Fara-

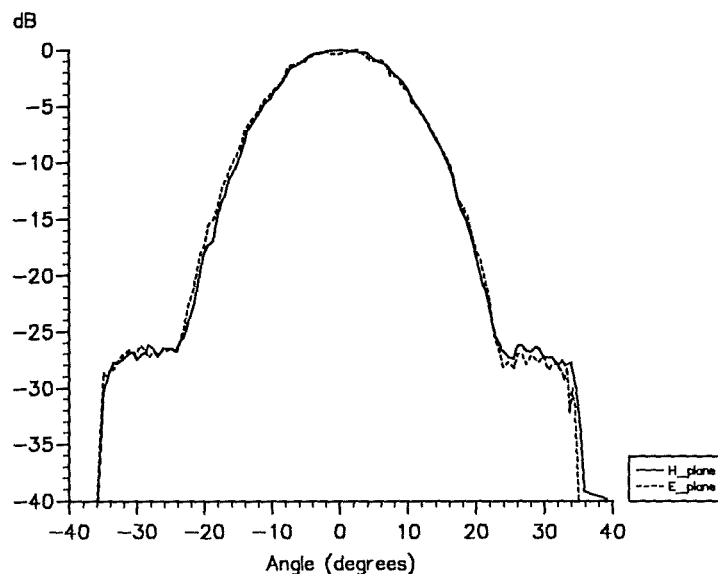


Figure 4.16: The H-plane and E-plane radiation patterns for the scalar feedhorn.

day rotators; multiple reflections between these components; and also from truncation. Figure 4.16 shows the H-plane and E-plane patterns of the scalar feedhorn actually used. The *shoulders* on the main lobe of the pattern at around $\pm 30^\circ$ on both patterns are probably the result of using the feedhorn at a frequency 4.3% away from it's design frequency (i.e. at 90 GHz rather than at 94 GHz).

Figure 4.17 shows the H-plane and E-plane patterns of the beam radiated from the quasi-optical circuit, and having an effective source aperture at the pivot point of the radiation pattern measurement system. The horn's shoulders appear to have been truncated, and particularly so for the E-plane pattern. Both patterns have a small dip at -8° of < 1 dB, and the E-plane pattern is slightly asymmetrical, (cf. -10 dB crossover points).

The distortion of the fundamental mode pattern appears to be minimal. This is especially so if the number of higher order modes that is likely to be of interest is less than about six. This result is adequate for the purposes of the work described here, but should significantly higher-order mode patterns become important in subsequent work, then these distortions would require careful analysis and their origin and stability would need to be determined.

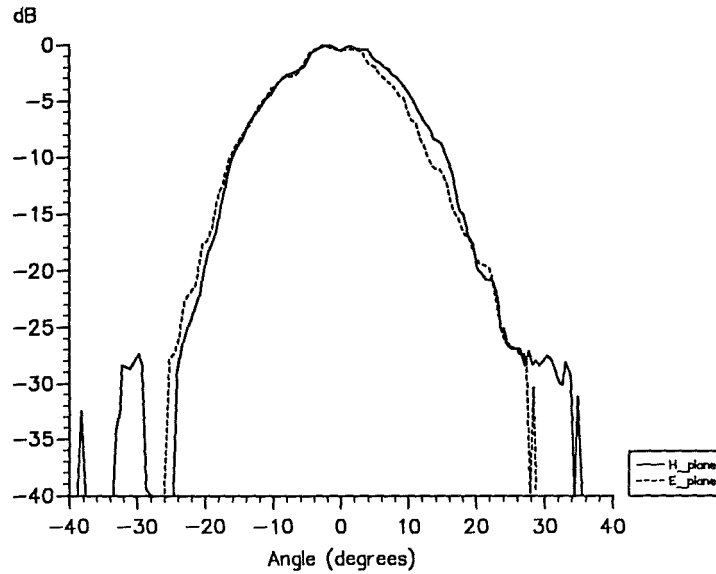


Figure 4.17: The H-plane and E-plane radiation patterns of the radiated quasi-optical beam.

4.4.4 Source Aperture Position

An experiment was performed to verify the position of the output beam waist, that is, of the effective source aperture. The position the scalar feedhorn was varied and the position of the output beam waist was then approximately located (± 5 mm) by suspending a small rectangular piece of millimetre wave absorber material within the beam at about the beam waist and moving this absorber along the beam axis. A null in the received power was looked for, and a radiation pattern was measured. The millimetre wave absorber material was inclined at 45° in order to minimise reflections back into the circuit. From Lesurf[2, page 39] the minimum size for a given level of occultation of the beam can be determined. For an absorber diameter of three times the output beam waist size, 98.9% of the beam can be expected to intercepted by the absorber. Thus if $\omega_o = 4.4$ mm then an appropriate diameter would be say 14 mm. The piece of absorber was 14 mm wide and 20 mm high, though when inclined at 45° presented a 14 mm projected height to the beam.

Figure 4.18 shows an output beam pattern with and without the absorber material suspended at the beam waist. Figure 4.19 compares the output beam pattern with and without the horizontal suspension wire. Note that:

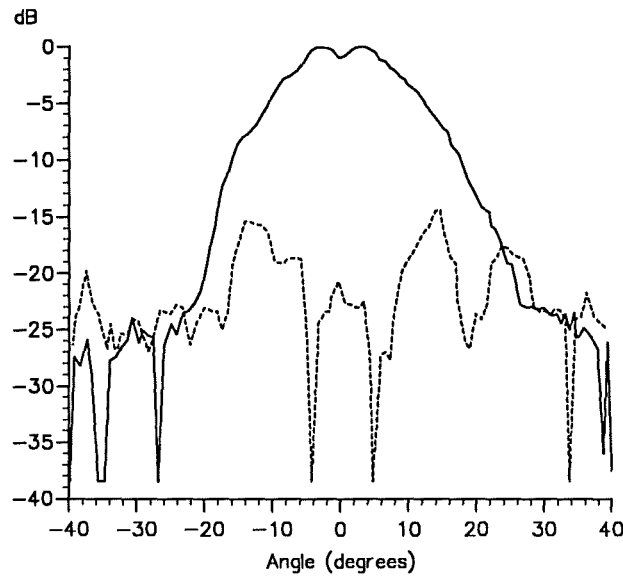


Figure 4.18: Occultation of the beam by a small piece of absorber material at the output beam waist.

1. The output polarisation is at 45° to the horizontal.
2. The pattern distortions result from using a somewhat imperfect planar mirror at the SLM plane.
3. The patterns are of the horn/beam's H-plane.

This result presented here is for the case where the scalar feedhorn's aperture is 98 mm from the lens aperture plane and the position of the output beam waist is 100 mm from the output lens aperture. Thus the effective source aperture is indeed positioned fairly accurately over the pivot point of the radiation pattern measurement system (i.e. within $\pm 5\%$).

References

- [1] J. A. Neff, R. A. Athale and S. H. Lee, "Two-Dimensional Spatial Light Modulators : A Tutorial," *IEEE Proceedings*, vol. 78, no.5, 1990.
- [2] J. C. G. Lesurf, *Millimetre-wave Optics, Devices and Systems*. Adam Hilger, 1990.

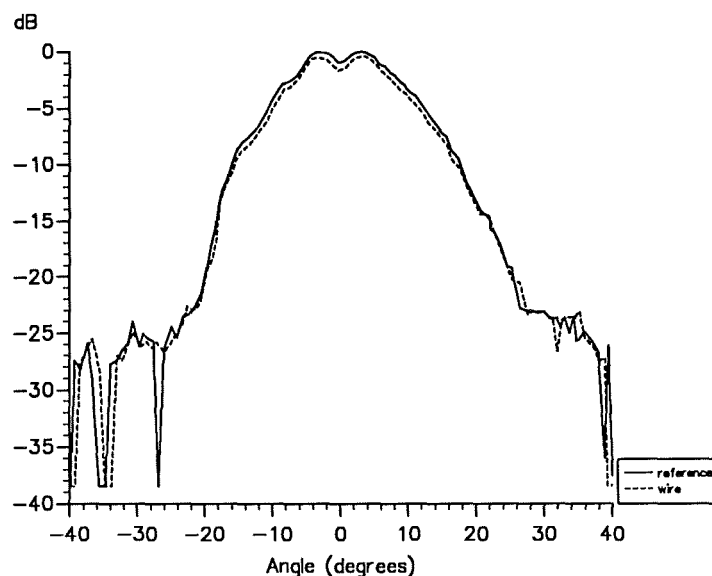


Figure 4.19: The effect of the suspension wire on the beam's radiation pattern.

- [3] S. Jacobsson, A. Lundgren and J. Johansson, "Computer Generated Phase Holograms (Kinoforms) for Millimeter and Submillimeter Wavelengths," *International Journal of Infrared and Millimeter Waves*, vol. 11, pp. 1251–1261, 1990.
- [4] W. H. Kummer and E. S. Gillespie, "Antenna Measurements—1978," *IEEE Proceedings*, vol. 66, no. 4, pp. 483–507, 1978.
- [5] IEEE Antenna Standards Committee, *IEEE Standard Test Procedures for Antennas*. IEEE Std. 149–1979, IEEE Inc., 1979.
- [6] C. A. Balanis, *Antenna Theory, Analysis and Design*. Harper & Row, New York, 1982, chapter 15.
- [7] C. C. Cutler, A. P. King and W. E. Kock, "Microwave Antenna Measurements," *Proceedings of the IRE*, vol. 35, pp. 1462–1471, Dec. 1947.
- [8] A. P. King, "The Radiation Characteristics of Conical Horn Antennas," *Proceedings of the IRE*, vol. 38, pp. 249–251, March 1950.
- [9] E. I. Mueldorf, "The Phase Center of Horn Antennas," *IEEE Trans. Antennas Propagation*, vol. 18, pp. 753–760, Nov. 1970.
- [10] A. R. Harvey, *PhD Thesis*. University of St. Andrews, 1990.

- [11] M. J. Leeson, *PhD Thesis*. In press, University of St. Andrews, 1992.
- [12] G. M. Smith, *PhD Thesis*. University of St. Andrews, 1990.
- [13] R. J. Wylde, "Gaussian beam-mode optics and corrugated feed horns," *IEE Proceedings*, vol. 131, pt. H, no. 4, pp. 258–262, 1984.
- [14] A. R. Harvey, *Private Communication*, 1992.

Chapter 5

A Millimetre Wave Pyroelectric Detector

This chapter contains a verbatim copy of an article written by myself and published within the International Journal of Infrared and Millimeter Waves, volume 12, number 10, pages 1225–1231, 1991.

Abstract

A pyroelectric detector has been built and characterised for operation within W-band. The various characteristics reported include detectivity, responsivity, NEP, polarisation sensitivity, dynamic range, linearity, and reflectivity (vswr). The pyroelectric detector performs well at these wavelengths and as the detector is inexpensive to build, and is robust, it ought to find many opportunities for use within millimetre-wave laboratories.

5.1 Introduction

The pyroelectric detector described here exploits the ferroelectric properties of triglycine sulphate (TGS) within the millimetre-wave region. This material is usually used within the infrared region of the electromagnetic spectrum and for various kinds of detection schemes, from simple detectors through to vidicons and other imaging systems. To this authors knowledge, it's usefulness at wavelengths around 3 mm has not been explored or recorded in the literature.

Hadni[1] has provided a thorough treatment of pyroelectricity and pyroelectric detectors. Hadni states that as early as 1963 high IR detectivities at room temperature had been realised, e.g. $D^* = 3 \times 10^8 \text{ cm Hz}^{1/2} \text{ W}^{-1}$, which compare well with Go-lay's pneumatic detector ($D^* = 3 \times 10^9 \text{ cm Hz}^{1/2} \text{ W}^{-1}$). The theoretical maximum detectivity at room temperature for this material is $D_{\text{ideal}}^* = 2 \times 10^{10} \text{ cm Hz}^{1/2} \text{ W}^{-1}$, and the quoted IR detectivity for the actual device investigated here is $D^* = 1.8 \times 10^8 \text{ cm Hz}^{1/2} \text{ W}^{-1}$. The millimetre-wave detectivity measured and reported here has a maximum of $3 \times 10^6 \text{ cm Hz}^{1/2} \text{ W}^{-1}$ which corresponds to a noise equivalent power (NEP) of around $30 \text{ nW Hz}^{-1/2}$. This sensitivity is sufficient for many circumstances.

5.2 Detector Description

5.2.1 The Pyroelectric Sensor

The actual device being used is a Philips[2] P5219 deuterated L-alanine TGS (DLATGS) pyroelectric infrared detector. The pyroelectric element is combined with an impedance converting amplifier, and both are sealed and encapsulated within a TO-12 package. The window material is polyethylene. There is a recommended single transistor amplifier with a gain of 4.8 that was also used. Philips quote a detectivity of $D^* = 1.80 \times 10^8 \text{ cm Hz}^{1/2} \text{ W}^{-1}$ at a modulation rate of 100 Hz and for a 1 mm diameter element at room temperature.

5.2.2 The Detector Housing

The device was housed within a small aluminium cylindrical block, and was butted up against a 2.34mm diameter waveguide hole, which was about 2mm long. An IR and submillimetre-wave filter was employed between the device and the waveguide. This consisted of one layer of thick black insulating tape and a piece of thin card, the insertion loss of which was measured to be 0.7 dB. The feed horn used was one that produces a Gaussian beam, and was needed in order to optimally couple to the free-space beam. However, there was a mismatch between the horn and the housing that was in addition to any pyroelectric element mismatch. The resulting vswr of 2.2 incorporates both of these mismatch effects.

5.3 Performance

5.3.1 Measurement Approach

The measurements were made at an operating frequency of 91GHz, the source being a GaAs Gunn diode mounted within a W/G 27 block. Measurements were made using a quasi-optical circuit[3] and figure 5.1 shows a diagram of the circuit that was used. A waveguide circuit was also investigated, but the resultant dc earth connection between the oscillator and the detector produced unwanted spikes on the detector's output voltage waveform. No such difficulty exists with the quasi-optical circuit. The quasi-optical circulator[4] enabled the measurement of power reflectivities and also facilitated a simple and reliable measurement procedure. With the ferrite disc in the circuit as shown, power from the source is directly coupled into the pyroelectric detector, and a power reflectivity measurement can be made at the port nominated on the diagram. If the ferrite disc is flipped so that the arrow points towards the source, then the power from the source is coupled to the port where an absolute power measurement can be made. Measurements of absolute power and pyroelectric detector responsivity can thus be made at equivalent reference planes. Absolute power measurements were made with a Boonton power meter, and a feed horn identical with the pyroelectric detector's feed horn was used. Thus the amount of power actually incident at the pyroelectric detector housing's input waveguide can be determined. All responsivity measurements are quoted with respect to this power level, rather than say to the actual power absorbed. The detector's noise voltage was measured with an FFT analyser, a Brüel & Kjær High Resolution Signal Analyser, Type 2033, and it also proved convenient to use this analyser for the output voltage measurements.

5.3.2 Measurement Results

Table 5.1 summarises the performance of the pyroelectric detector as mounted and measured according to the foregoing description. It is readily observed that from a modulation rate of 10 Hz and upwards, the responsivity falls at a rate of 10 dB/decade. The NEP minimum (and D^* maximum) is at around 10 Hz. Figures 5.2–5.5 provide more detail of the detector's performance as a function of modulation rate.

The data given in table 5.2 are of the detector's rf characteristics. The detector was sensitive to polarisation and this seems to be the case because the pyroelectric element

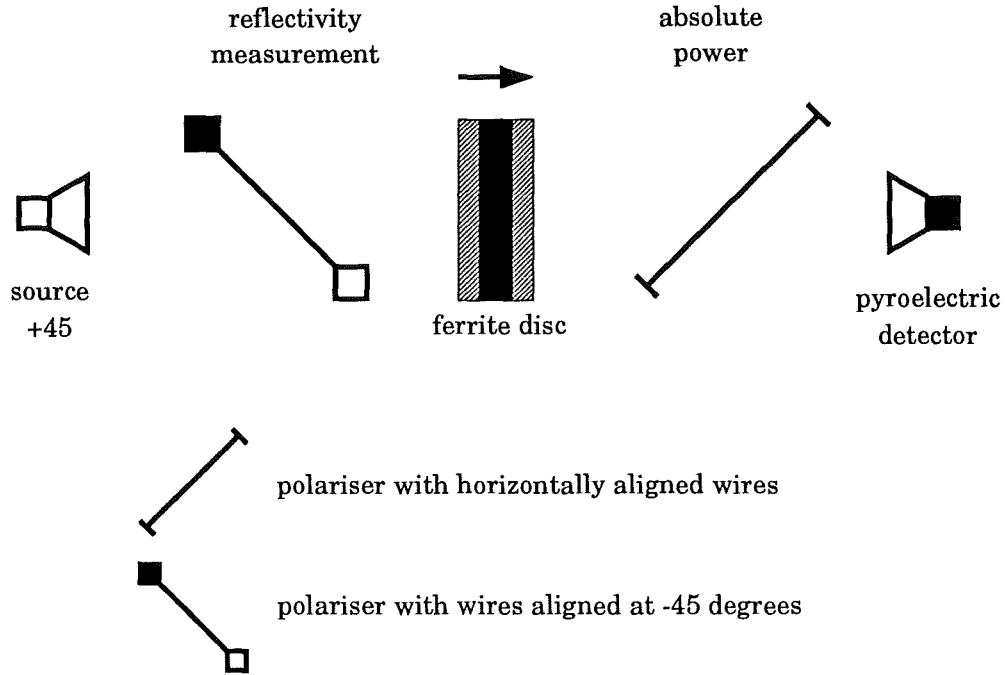


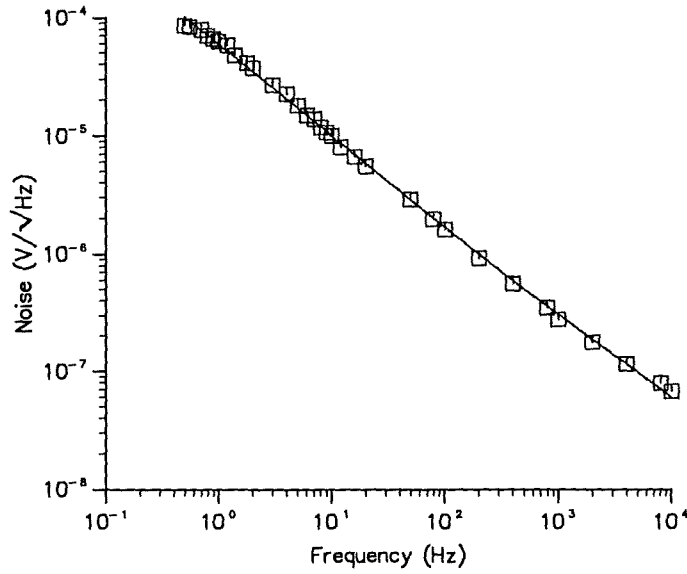
Figure 5.1: A schematic diagram of the quasi-optical circuit used to measure the pyroelectric detector's characteristics. Lenses have been omitted from the diagram in order to maintain clarity.

Freq. (Hz)	e_n ($\mu\text{V Hz}^{-1/2}$)	Responsivity (V W^{-1})	NEP ($\text{nW Hz}^{-1/2}$)	Detectivity, D^* ($\text{cm Hz}^{1/2} \text{W}^{-1} \times 10^6$)
1	62	1140	54	1.6
10	10	321	31	2.9
100	1.6	37	43	2.1
1000	0.28	3.5	80	1.1
10000	0.067	0.23	290	0.30

Table 5.1: These results are for measurements that include the amplifier which has a gain of 4.8.

Incident Beam at 91 GHz	
Reflectivity (W/W)	0.135
VSWR	2.2
Pol. Sensitivity (dB)	< 3

Table 5.2: Mounting characteristics for the pyroelectric detector.

Figure 5.2: Noise voltage, e_n .

within the TO-12 package was not centred precisely. It was off centre by about 0.5 mm. The maximum responsivity occurred for the element in the centre-vertical plane.

The responsivity was measured for varying power levels at modulation rates of 0.55 Hz and 10 Hz. Figure 5.6 shows these results. Power levels from $< 10\mu\text{W}$ to $> 10\text{ mW}$ were explored, and while there is some variation within this range, saturation type phenomena are not observed. The measurement process involved some time delay between measurement of power levels and responsivities, as well as some oscillator bias voltage adjustment. This is undoubtedly a contributing factor to the variation observed. Simultaneous measurement of power level and responsivity is needed to more reliably assess linearity for this detector. Whatever, the detector as mounted has a dynamic

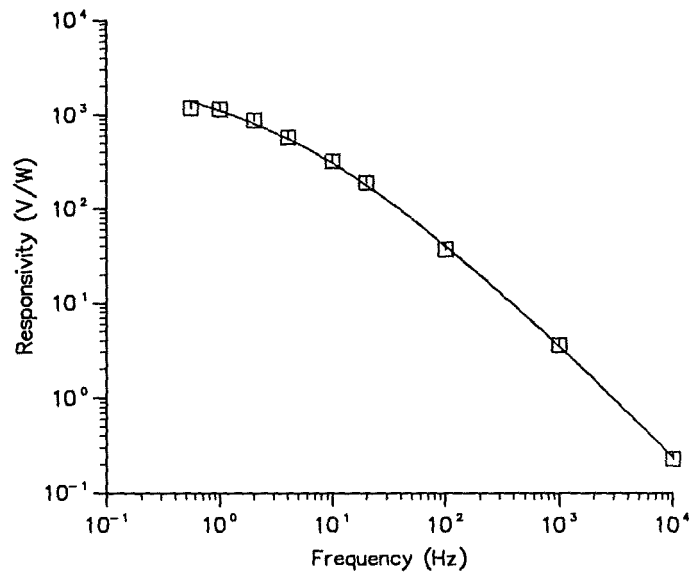


Figure 5.3: Responsivity.

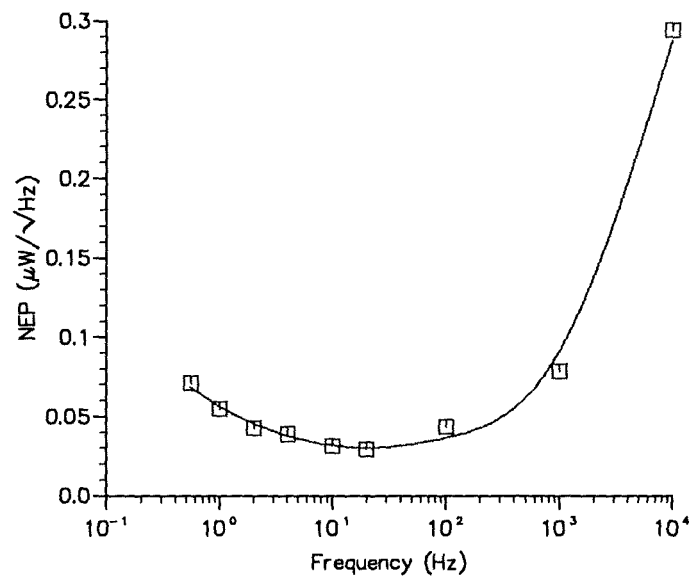


Figure 5.4: Noise equivalent power, NEP.

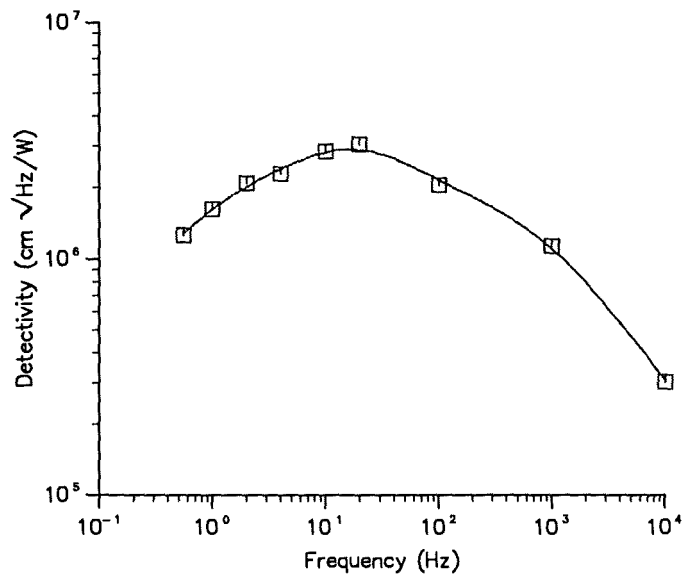
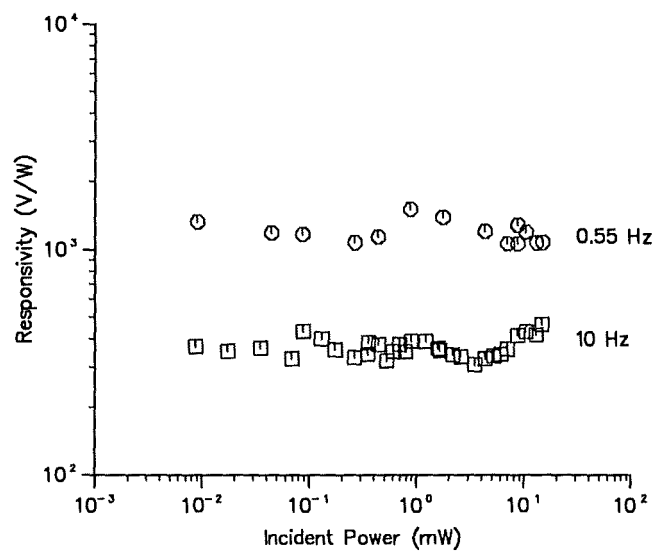
Figure 5.5: Detectivity, D^* .

Figure 5.6: Responsivity variation with incident power level.

range in excess of 50 dB.

5.4 Conclusion

The detector described within this paper is a low-cost, robust component, valuable for use within the millimetre-wave band. Its sensitivity is such that it could be considered to be useful as a general laboratory detector. Like the Golay detector, it can be used at higher frequencies with no difficulty and in fact has been used successfully at 140 GHz for measuring radiation patterns. Planar arrays of the pyroelectric elements could also be worth investigating, though the hygroscopic properties of the DLATGS material would need to be accommodated for, should the elements be used outside of the TO-12 type packaging. Finally, regarding likely improvements in performance, the process of matching the free-space millimetre-wave beam to the pyroelectric element itself could be optimised. Possibly a larger diameter pyroelectric element could be used and impedance matching schemes[5] may be worth some consideration.

Acknowledgements

The pyroelectric device was provided for research by Philips Components Ltd, Southampton, UK. Helpful discussions with Mr. Geoff Baker (Philips), Dr. Jim Lesurf and Dr. Graham Smith are gratefully acknowledged. The modular system used for the measurements was designed by Dr. Andy Harvey.

References

- [1] A. Hadni, *Infrared and Millimeter Waves—Vol. 3*. Editor: K. J. Button, Academic Press, pp. 111–180, 1980, chapter 3.
- [2] Philips Components : *Advance Development Sample Information*. April 1989.
- [3] J. C. G. Lesurf, *Millimetre-wave Optics, Devices and Systems*. Adam Hilger, 1990.
- [4] M. R. Webb, “A MM-Wave Four-Port Quasi-Optical Circulator,” *International Journal of Infrared and Millimeter Waves*, vol. 12, no. 1, pp. 45–63, 1991.
- [5] A. Hadni and X. Gerbaux, “Infrared and Millimeter Wave Absorber Structures for Thermal Detectors,” *Infrared Physics*, vol. 30, no. 6, pp. 465–478, 1990.

Chapter 6

A Millimetre Wave Faraday Rotator

This chapter describes the design and performance of a millimetre wave Faraday rotator. The first section deals with some early work that was done with a small diameter ferrite disc (30 mm). It was later found that large area ferrite sheets (100 mm) could be produced and these have the advantage that their position within a quasi-optical circuit need not be at a focussed waist. This eliminates the need to use two additional lenses wherever a Faraday rotator is required within a given circuit. Finally, the reflection properties of a ferrite sheet have also been modelled and measured, and the last section describes this work.

6.1 A MM-Wave Four-Port Quasi-Optical Circulator

This section contains an almost verbatim copy of an article written by myself and published in the International Journal of Infrared and Millimeter Waves, volume 12, number 1, pages 45–63, 1991.

Abstract

A four-port quasi-optical circulator has been designed, built and tested for operation in the millimetre wave band. The specific circulator reported here was investigated over a 20 GHz bandwidth, centred on 94 GHz. Good performance characteristics were obtained over this bandwidth. Isolations of better than 30 dB

and insertion losses of around 0.5 dB were achieved. The input vswr was found to be less than 1.35 over the whole bandwidth investigated and vswr's of less than 1.1 were achieved for narrower bandwidths. It is possible of course to configure the 4-port circulator as a 3-port circulator, or indeed as 2-port isolator. Further optimization and consequent improvements in performance are almost certainly obtainable.

6.1.1 Introduction

Early work on ferrite based circulators and isolators for operation in the millimetre wave band, goes back at least to the work reported by Meredith and Preece [1] in Benson's book *Millimetre and Submillimetre Waves* (1969). Good performance figures are reported there, and little improvement in these figures has been reported until recently. Wiltse [2] in Button and Wiltse's multi-volume *Infrared and Millimeter Waves* (1981), states that improvement is needed in ferrite and other non-linear devices, around 100 GHz and above, and also in particular, losses associated with these devices need to be reduced. In the same volume (vol. 4) Reedy and Ewell [3] state that passive circuit components are often overlooked, even though they are essential to systems and indeed are often the system performance limiters. He cited as a specific example, the circulator. Again, now in 1987, Brown and Wiltse [4] state that there is *still* great room for continued improvement in components and devices, particularly in extending ferrite and other non-linear devices to frequencies above 100 GHz and in reducing losses in most components. Again Reedy [5] states that above 35 GHz considerable work is required to develop low cost, wide bandwidth, and high isolation components. Currie and Currie [6] state that while ferrite devices are available up to 140 GHz, above 90 GHz, losses and poor performance means these devices are marginally useful. A system tradeoff study [7] comparing two radar systems, one at 35 GHz and the other at 94 GHz yielded, perhaps unexpectedly, marginal performance improvements for the 94 GHz system over the 35 GHz system. The 94 GHz system was crippled by excessive waveguide and waveguide component losses of around 19 dB compared to 8 dB for the 35 GHz system. If these losses were reduced significantly, a different picture entirely would have resulted. In 1988 a high performance, quasi-optical isolator was reported [8, 9], for operation at 35 GHz. This isolator required a magnetic bias field to be applied to the ferrite disc, whereas the device reported here does not. The

device reported here operates at 100 GHz though it does not have associated with it any intrinsic frequency limitation to 100 GHz. The circulator described within this report, has performance characteristics that attempt to address the issues outlined above. In addition, the circulator described herein, is a relatively low-cost device and thus addresses one of the prime difficulties associated with millimetre wave technology, namely the high cost of components, Wiltse [10].

The key component in the circulator is a ferrite disc, which has the particularly useful characteristic that it is able to provide non-reciprocal polarisation rotation of a linearly polarised electromagnetic wave passing through it, under appropriate conditions. This paper describes the circulator, defines the performance parameters used and provides a summary of measurement results.

6.1.2 Circulator Description

6.1.2.1 Topology

The essential elements are depicted in figure 6.1. The symbols used in this figure are those recently proposed by Dr. Jim Lesurf[11]. The forward power transfer paths for the four-port circulator are, port 1 to port 2, 2 to 3, 3 to 4, and 4 to 1. The circulator works in the following manner: Consider a vertically polarised electromagnetic wave entering the circulator at port 1. The wave will pass unimpeded through the first polariser, which has horizontally aligned wires. As the wave passes through the ferrite disc¹, its polarisation state, which is vertical, will be rotated $+45^\circ$ (i.e. clockwise looking along the arrow). The wave's polarisation state is still linear, and is now orthogonal to the second polariser which has wires aligned at -45° , and thus will also pass through the second polariser to appear at port 2. This description of the forward path 1 to 2, applies similarly to the other three forward paths. In order to consider the isolating properties of this circulator, consider the above wave as being reflected at port 2, that is, back into the circulator. No power ought to appear at port 1, but should appear only at port 3. The reflected wave is still orthogonal to the polariser with wires aligned at -45° and so passes through it unimpeded. As the wave once again passes through the ferrite disc, its polarisation state is rotated 45° clockwise looking along the arrow, that is, in the *same* direction as it did when it passed through the ferrite disc going from port 1 to port 2. The wave is now polarised in the same direction as the alignment

¹Refer to section 6.1.2.3 and to appendix 6.1.5 for discussion on the polarisation rotation mechanism.

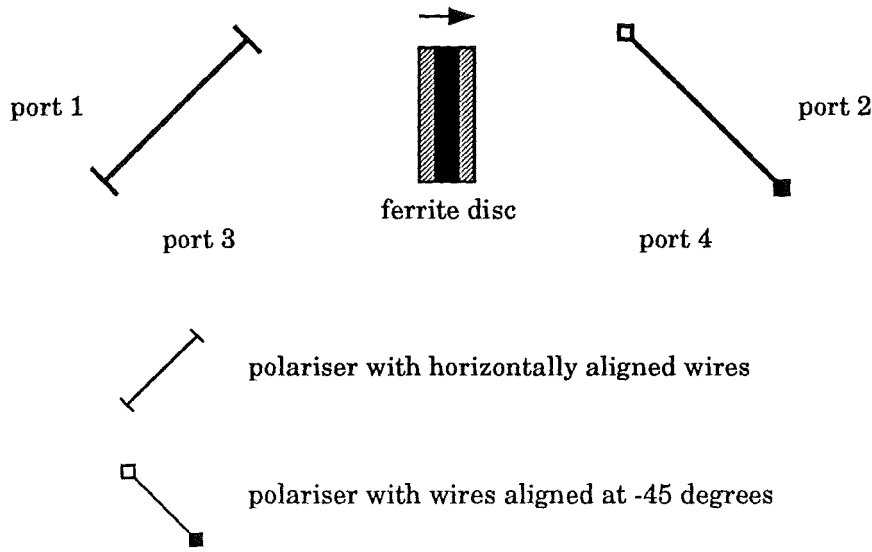


Figure 6.1: A schematic diagram of the circulator.

of the wires (i.e. horizontal) of the next polariser in it's path. Thus the wave is reflected by this polariser and appears at port 3, *not* at port 1. This description applies in a similar way to the other reverse paths. Non-idealities in the system such as reflections from the ferrite surfaces complicate the above picture a little, and are discussed in section 6.1.3.1.

6.1.2.2 Bandwidth

The bandwidth limiting features of this design are those associated with the need to couple energy across material boundaries. The ferrite disc's provision of polarisation rotation is essentially independent of frequency—see appendix 6.1.5—and therefore only the impedance matching of the lenses and the ferrite disc to free space is considered here. The lenses are *blazed* and the ferrite disc is *bloomed*. The *blazing* involves cutting circular, concentric grooves into the lens surfaces the depths of which are a quarter of the geometric mean of the centre wavelengths for the two different media, that is, the depth d is given by

$$d = \frac{\sqrt{\lambda_{\text{air}} \lambda_{\text{lens}}}}{4}$$

The lens material used was HDPE [12]. The *blooming* involves placing two quarter wavelength impedance transforming patches either side of the ferrite disc. These patches

were produced from the material Fluorosint² [15]. The required Fluorosint thickness, t , is given by the equation,

$$t = \frac{\lambda}{4n}$$

where λ is the free space wavelength and n is the refractive index of Fluorosint (see section 6.1.2.3). The tolerance required in the Fluorosint patch thickness is of the order of one micron, for frequencies around 100 GHz, since at this frequency the design centre frequency shifts about 1 GHz for every 5 μ m thickness change in Fluorosint. The refractive index n_f of the ferrite is in fact dual-valued (see appendix 6.1.5) and so the thickness of the blooming layers is based on the arithmetic mean of the two values of refractive index. This aspect of the matching process results in a limitation on the efficacy of the matching itself and ultimately on the isolation performance also. The isolation performance is affected because imperfect matching will result in multiple internal reflections which will tend to depolarise the resultant transmitted beam.

The most useful and practical way to define the circulator bandwidth, is to define it as that frequency range over which the performance of the circulator meets certain, specified levels. Section 6.1.3.2 presents results for a 20 GHz bandwidth, that is, a 20% bandwidth, and over this bandwidth good performance results were achieved.

For optimal performance at any specific frequency, the patches and lenses ought to be designed to suit. An upper limit is probably set by how well the ferrite blooming can be realised. Operation at 300 GHz ought to present no fundamental difficulty. The circulator built here in St. Andrews has been realised using a modular half-cube system that has the advantage of flexibility in terms of topology and frequency of operation.

6.1.2.3 Materials

Ferrite

The ferrite material used in the circulator reported herein, is a Philips ferrite, namely Ferrox dure 330, a strontium hexagonal ferrite[13]. This material has been investigated by Wylde [14]. He reports a mean refractive index figure³ of 3.88 ± 0.03 , and a rotation figure of about 20°/mm. This is close to what one would expect from published data on the ferrite's remanence (0.37T), if this figure is used in the approximate theory typically

²Polypenco Fluorosint is a Trademark of the Polymer Corporation USA and Polypenco Companies.

³The ferrite permeability is not simply a constant but is rather a tensor quantity.

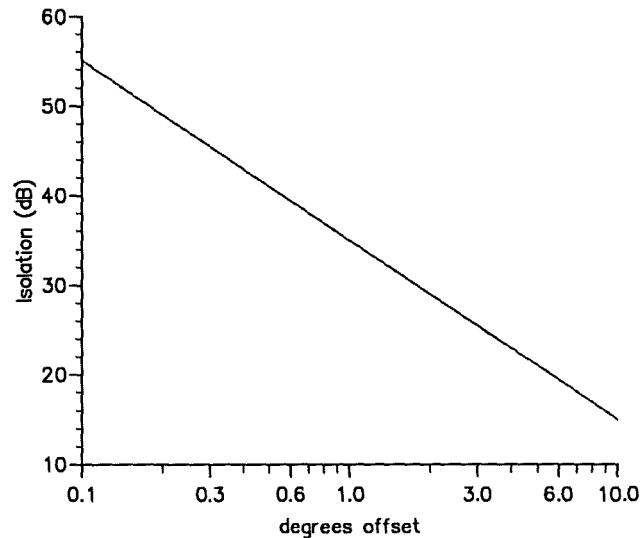


Figure 6.2: Isolation performance as a function of rotation accuracy.

used (see appendix 6.1.5). That is, the approximate theory predicts a rotation figure of about $24^\circ/\text{mm}$. However, a figure of $30^\circ/\text{mm}$ is reported here. It may be significant that care was taken to ensure that the ferrite disc was re-magnetised after the necessary cutting and grinding operations had been completed. A 1 T field was used for this. Also, Wylde's figure applied to measurements at 140 GHz, though the approximate theory would tend to indicate that this should not be significant. The $30^\circ/\text{mm}$ rotation figure corresponds to a saturated magnetisation of about 0.46 T and thus a resonant frequency of about 12.9 GHz. Compare this with 10.4 GHz for the 0.37 T field quoted by the manufacturers. Appendix 6.1.5 describes the property of the ferrite material being exploited here, namely the property that enables it to provide for *Faraday rotation*; (i.e. by nature of its anisotropic gyromagnetism).

An upper limit on the isolation performance is set by the accuracy to which the ferrite's thickness can be realistically specified—neglecting the effects of insertion loss and imperfect matching (the former enhances isolation while the latter degrades isolation performance). Nominally, with a $30^\circ/\text{mm}$ rotation figure, a 1.5 mm thick disc is required. The precise thickness required for 45° rotation is best determined empirically, but it is helpful to know the accuracies in thicknesses necessary to achieve various levels of isolation. The graph in figure 6.2 briefly summarises the required accuracies for a

range of isolations. The results obtained and given in section 6.1.3.2 indicate that the ferrite discs used were providing 45° rotation within about 1° or so. The isolation levels achieved required the entire dynamic range available in order to be measured. Perhaps the actual isolation levels are better but without greater dynamic range, it cannot be known. Certainly greater dynamic range would enable circulators to be designed with known higher isolation levels than those reported here, at least better than 40 dB.

It is interesting and perhaps pertinent to note that the ferrite thickness of 1.5 mm corresponds to about one wavelength in the ferrite at around 100 GHz. This may produce some resonant effect and indeed the results indicate that a small, superimposed resonant absorption might possibly be present, say of about 0.25 dB.

Fluorosint

Fluorosint is a formulation of PTFE alloyed with mica. This formulation was primarily developed in order to gain improved *mechanical* properties compared to those of PTFE alone. However, the near millimetre wavelength optical properties for Fluorosint have been investigated [15], and its refractive index of 1.88 is found to be near ideal for our application here. As reported above, the ferrite has a refractive index of 3.88 thus requiring the matching material to have a refractive index of $\sqrt{3.88} = 1.97$. This figure of 1.97 is sufficiently close to the refractive index of Fluorosint, for all practical purposes. The Fluorosint patches were machined from a rod of the material.

Some measurements have recently been carried out on a similar compound[16], that should prove to be even more suitable, in that its absorption losses are lower than those of Fluorosint.

It is important to note that the Fluorosint patches must lie flat on the ferrite disc surfaces. This can be achieved simply by holding the outer rims of the patches and ferrite disc together, but a more satisfactory and reliable technique is being investigated.

6.1.3 Circulator Performance

6.1.3.1 Definition of Performance Parameters

There are a number of ways in which the performance of the circulator described herein could be defined. Commonly, the kinds of parameter definitions used are those that provide an immediate, intuitive feel for performance level, and by which comparative assessments can quickly be made. For example, one might refer to insertion loss,

isolation and vswr parameters. However these well known terms can have varying shades of meaning or application. Such definitions are therefore at times confusing in that subtle differences in definition, one researcher to another, can be obscured.

I have chosen to describe quantitatively the function of this 4-port circulator by way of a 4×4 power transfer matrix. This matrix contains the sixteen different power ratio measurements that could be made between all of the ports. That is, I will assume the four-port network is *linear*, and will define the power ratios $G_{ij} : i = 1 \dots 4, j = 1 \dots 4$, as the ratio of the power measured at port i , to the power input at port j , the remaining ports being terminated with matched loads. This definition thus includes as an integral part of the circulator parameter definitions, the corresponding performance parameters of the feed horns, lenses and polarisers, as well as the beam coupling efficiency. The circulator exhibits symmetry (not reciprocity), and thus only 4 of the 16 power ratio measurements need to be made to fully characterise the four-port device. Of course relative phase measurements could also be made, but such measurements are not dealt with in this report. The more commonly quoted parameters such as isolation, vswr etc., are embedded within the matrix, and these will be extracted and tabled in the next section. There are four sets of parameters that could be measured, that is G_{i1}, G_{i2}, G_{i3} and G_{i4} . Figure 6.3 shows a helpful symbolic diagram of the circulator. Note that if a matched load, (or a short-circuit), is placed at one or two ports, the network can be considered as a three or two-port network, respectively. Thus the matrix would become either a 3×3 or a 2×2 matrix. The following comments elaborate on these four parameters by describing the physical mechanisms behind the parameter definitions.

Consider the forward path 1 to 2. Power from port 1 can only appear at port 4 via the mechanism of partial reflection from the polariser with wires aligned at -45° . Reflection into port 4 from a wave originating at port 1 will occur if the ferrite disc does not precisely provide $+45^\circ$ of rotation. Reflection into port 4 will also occur if the resultant transmission after multiple reflections within the ferrite disc, are of a significant magnitude. Isolation from port 3 however is more complicated. Figure 6.4 shows a schematic drawing of the ferrite disc with Fluorosint patches either side. Reflections will occur from both ferrite surfaces, B and C. Reflections from the surfaces A and D reduce the amount of net reflection by reflecting power $180^\circ(2 \times \lambda/4)$ out of phase with the reflections from the surfaces B and C, respectively. Net power reflected by the pair

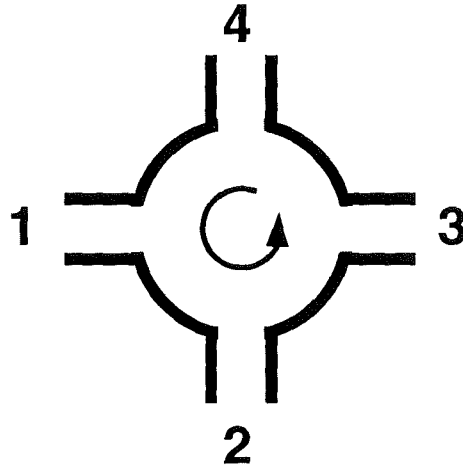


Figure 6.3: A symbol for the circulator, a four-port network.

of surfaces A and B will appear back at port 1, while net reflection from the pair of surfaces C and D will appear at port 3. The wave reflected from the pair of surfaces C and D must travel twice through the ferrite medium, which is lossy, and thus provided the ferrite disc provides almost exactly 45° of rotation, the amount of power appearing back at port 3 will be less than that appearing at port 1. Of course multiple reflections will occur within the ferrite/Fluorosint disc package, but any reflections other than the primary reflections can be shown to be of negligible significance to the discussion here for G_{31} , (i.e. < -30 dB).

Following on from the foregoing discussion, the vswr performance for port 1 will essentially be defined by the amount of power reflected from the pair of surfaces A and B, while the insertion loss will include both pairs of reflections along with ferrite absorption.

6.1.3.2 Measurement Results

There are two sets of measurements presented here along side one another. They correspond to two separate ferrite discs, each with their own pair of Fluorosint patches. There is a difference in thickness between the two ferrite discs of about $30\mu\text{m}$. The Fluorosint patches were nominally designed and machined for quarter-wave matching at 94 GHz, though the required accuracies for optimum performance at the centre frequency, as mentioned in section 6.1.2.2, were not obtained. The need for the high

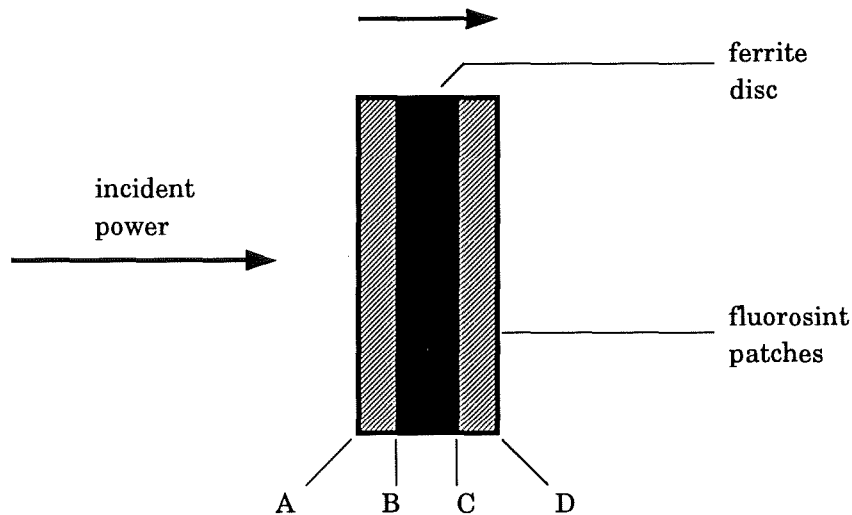


Figure 6.4: The ferrite disc with Fluorosint patches showing reflections from the four surfaces.

degree of accuracy in Fluorosint patch thickness, is knowledge that was gained in hindsight. Optimum frequencies as regards matching, are thus scattered for the four patches (two ferrite discs), over the 20 GHz frequency range explored, and optimal performance characteristics are thus also scattered.

The table in figure 6.5 provides a summary of nominal performance figures for the more commonly quoted parameters⁴.

PARAMETER	FERRITE A	FERRITE B
insertion loss	< 0.49 dB	< 0.55 dB
isolation (G_{41})	> 30 dB	> 24 dB
isolation (G_{31})	> 17 dB	> 16 dB
vswr	< 1.3	< 1.4
bandwidth	20 GHz	20 GHz

Figure 6.5: A table of the more commonly quoted **single-figure** parameters.

⁴Almost all the measurements for the adjacent port isolation, G_{41} , were dynamic range limited. The figures given are minimum isolations in all cases except for 104 GHz, which had significantly less dynamic range than the other frequencies and so is a minimum estimate in this case.

The graphs shown in figures 6.6 to 6.9, present the measurement results for both ferrite discs, as power transfer coefficients; viz. G_{11} , G_{21} , G_{31} and G_{41} . The forward path power transfer coefficient, G_{21} , has a number of component parts. These are the ferrite absorption loss, e , the ferrite reflection losses, $(1 - \Gamma^2)$, and the optics losses, η . The optics losses involve lens reflection losses, lens absorption losses, and beam coupling losses. The optics losses are common to the circulator as well as to the other parts of any given quasi-optical circuit, and therefore it is appropriate to define the circulator's *insertion loss*, L , as the combination of the ferrite's absorption and reflection losses alone. Figures 6.10 to 6.12 show graphs of the various loss components, and figure 6.13 shows a graph of the circulator's insertion loss. A graph of the circulator's vswr performance is given in figure 6.14. Appendix 6.1.6 describes how these various quantities are derived from the power transfer coefficients. Where any of the results have met with dynamic range limitations, this has been pointed out on the graphs.

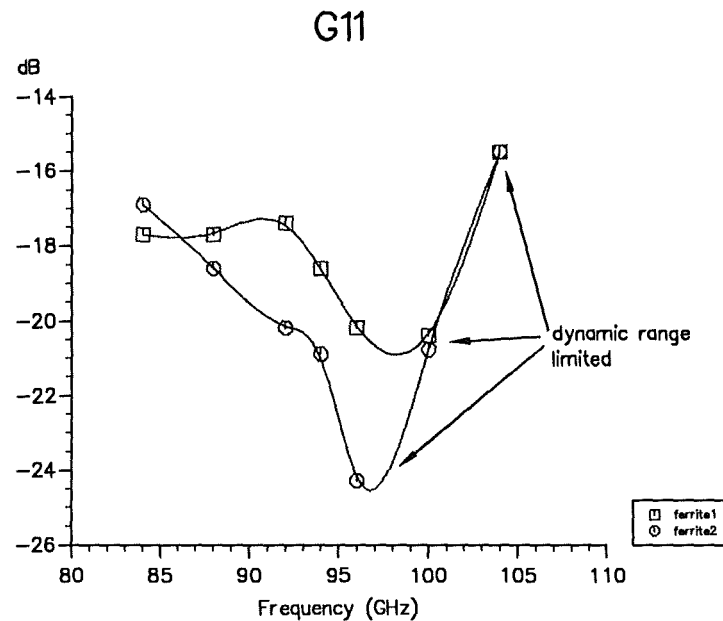


Figure 6.6: G_{11} is reflection coefficient for port 1.

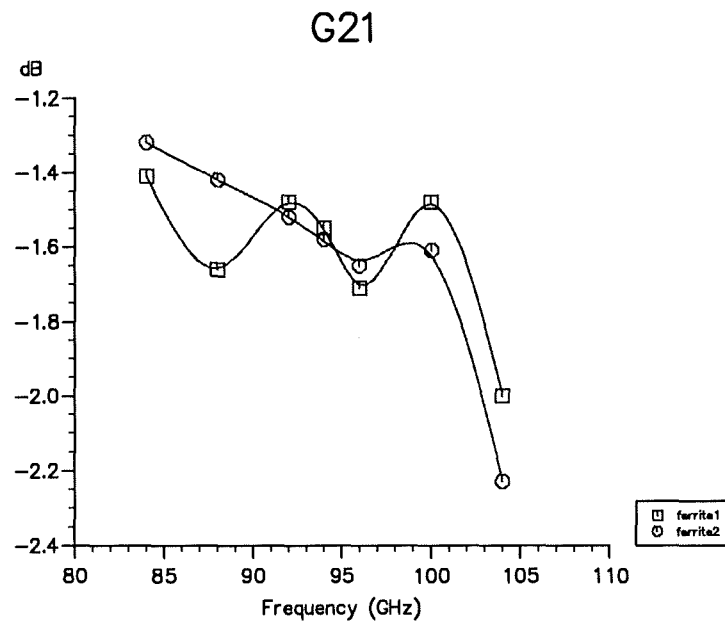


Figure 6.7: G_{21} is the transmission coefficient for power transfer from port 1 to port 2.

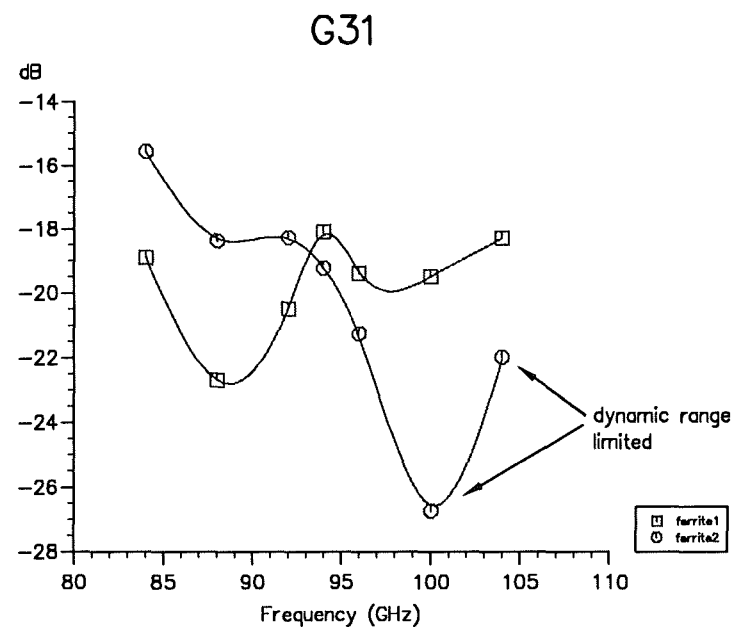


Figure 6.8: G_{31} is the transmission coefficient for power transfer from port 1 to port 3.

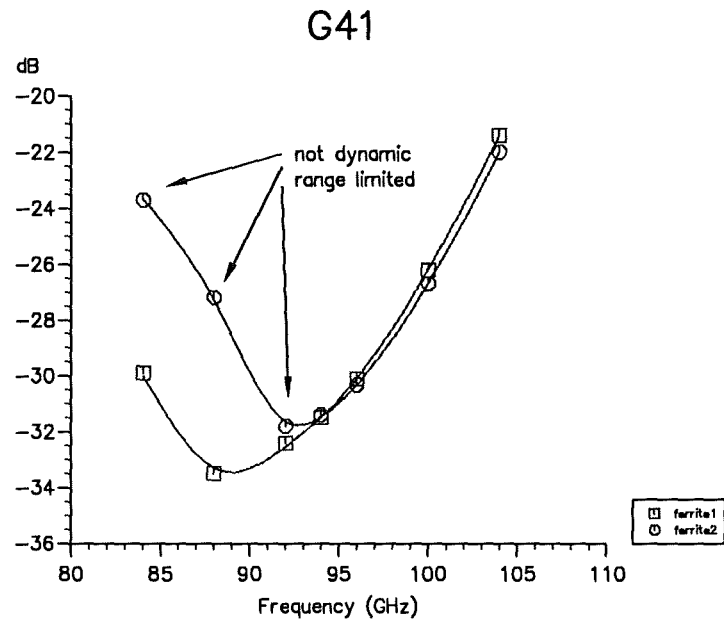


Figure 6.9: G_{41} is the transmission coefficient for power transfer from port 1 to port 4.

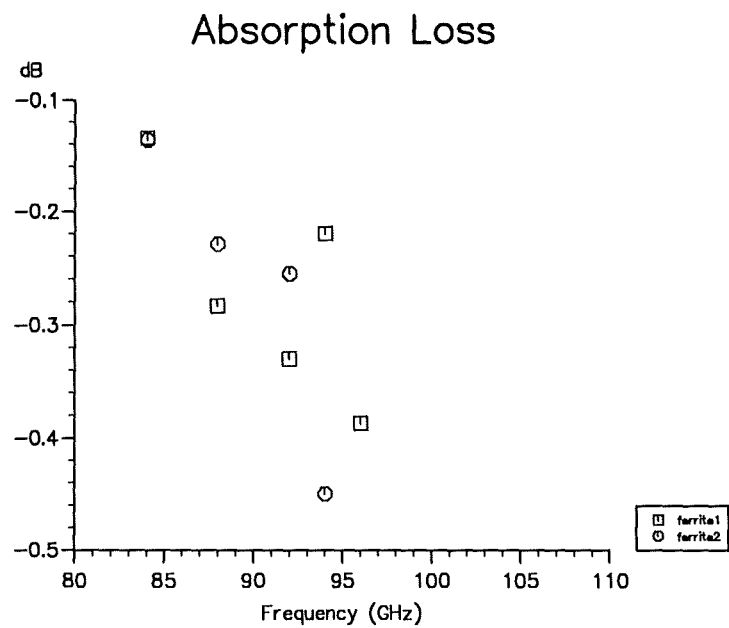
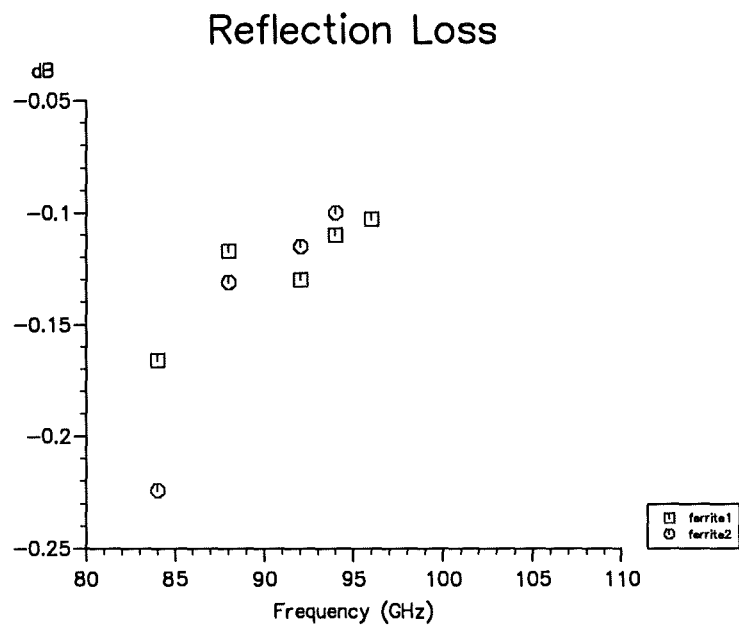
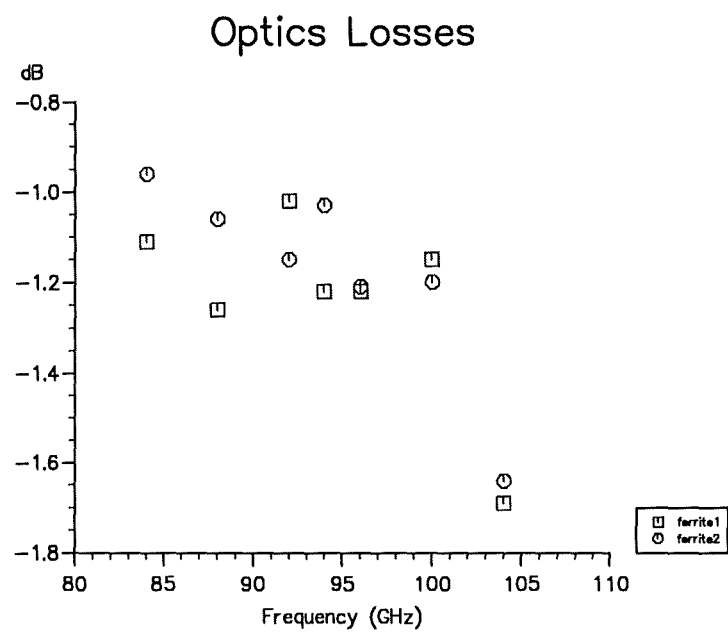


Figure 6.10: Absorption loss, e .

Figure 6.11: Reflection loss, $(1 - \Gamma^2)$.Figure 6.12: Optics losses, η .

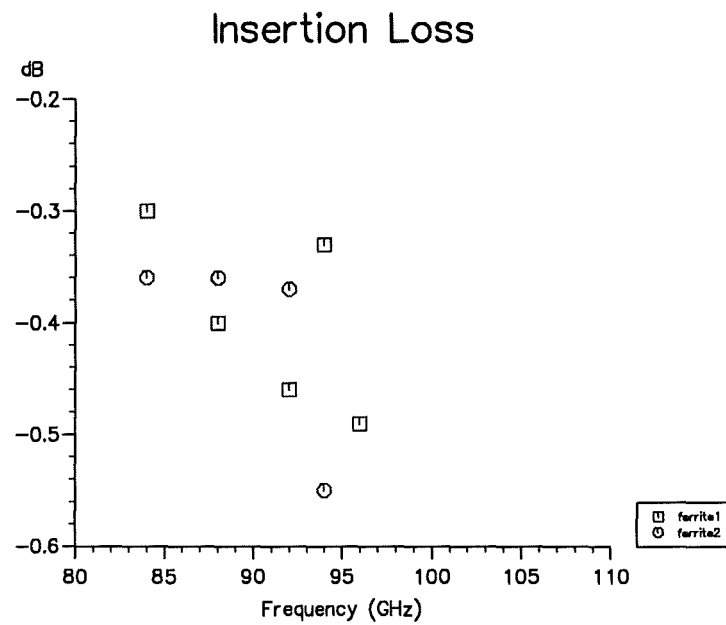
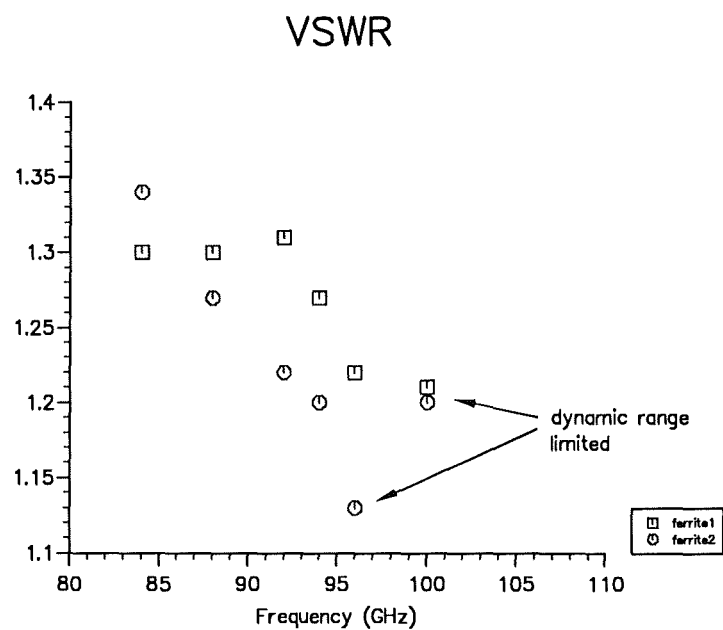
Figure 6.13: Insertion loss, L .

Figure 6.14: Input vswr.

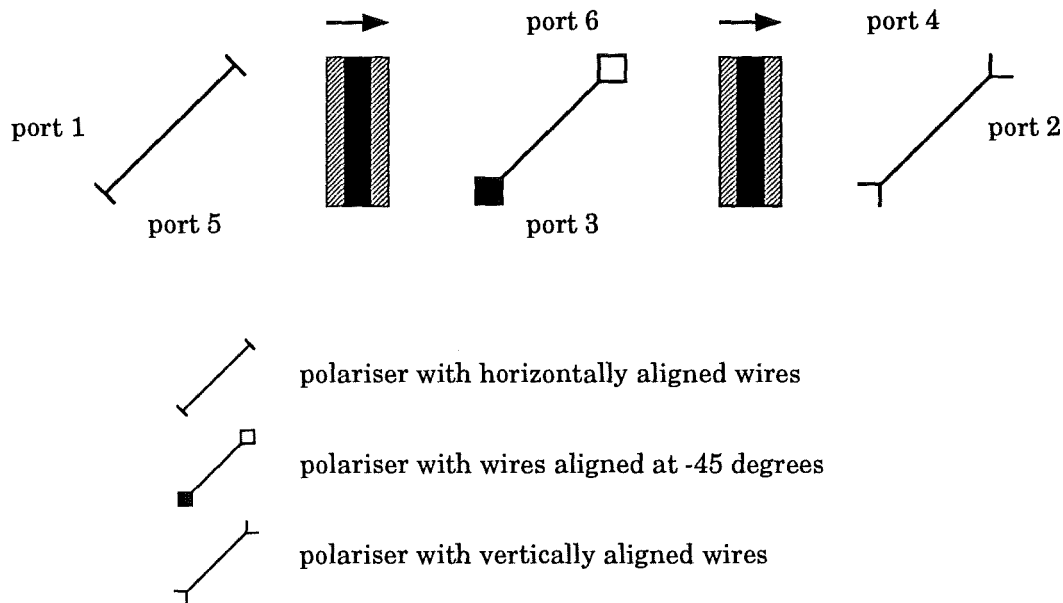


Figure 6.15: A schematic diagram of a six-port circulator.

6.1.4 Conclusion

A four-port quasi-optical circulator has been described herein that performs well over a wide bandwidth in terms of isolation and insertion loss, when compared to waveguide circulators operating within the same frequency range. A straight-forward extension exists for the design of a 6-port circulator, which could for example be used within dual polarisation systems (see figure 6.15).

The circulator described in this report has found application in an extremely sensitive, state-of-the-art, mm-wave noise measurement facility[17]. Within this facility the high 30 dB isolation is required in order to ensure that the oscillator, or other device or system, the noise of which is being measured, is decoupled from a very high Q ($> 10^5$) reference cavity, as well as providing an additional 3 to 4 dB SNR improvement. Figure 6.16 shows a photograph of this noise measurement facility. Of course many other applications exist for these kinds of circulators and isolators, including radar applications.

Optimal performance has not been achieved as yet, though the likely optimal limits

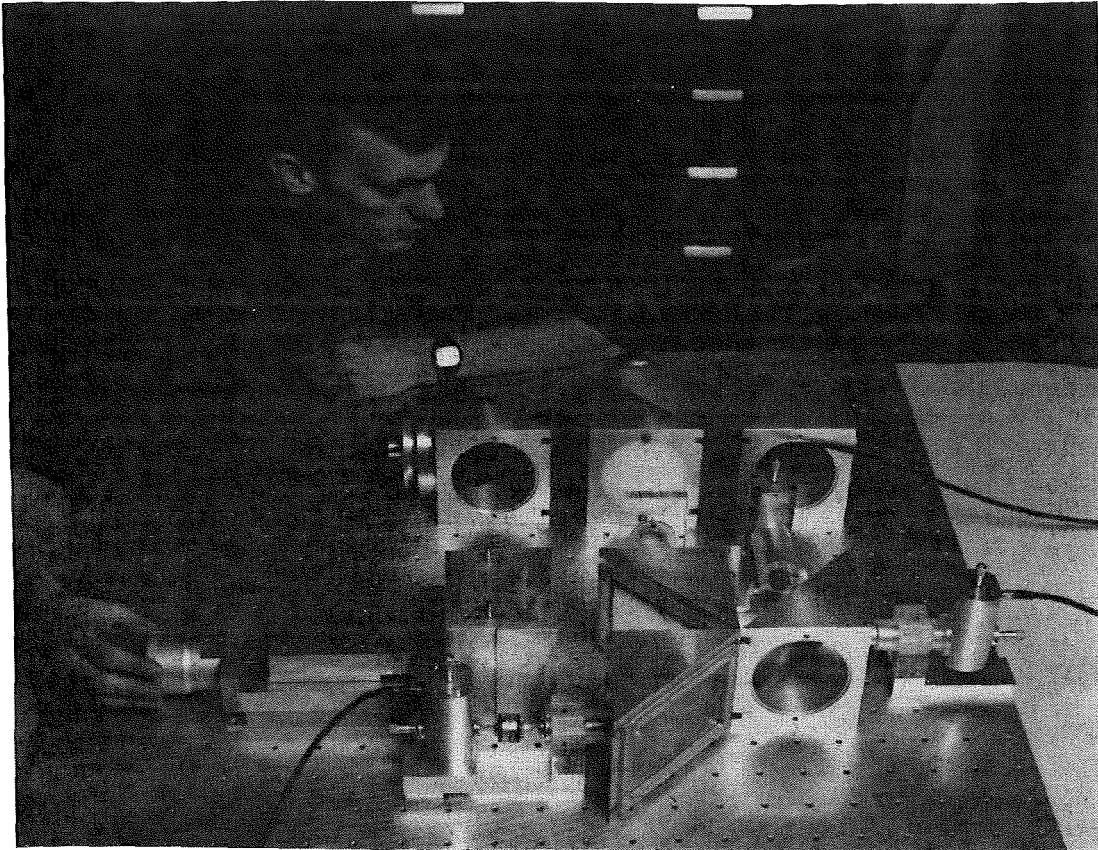


Figure 6.16: A very sensitive mm-wave quasi-optical noise measurement system incorporating the circulator.

can be realistically estimated from the measurements made so far. The key to improved performance is the optimisation of the matching of the ferrite disc to free space. There is room for improvement with closer tolerancing of the Fluorosint patch thicknesses. Also an increased dynamic range capability would allow meaningful, closer tolerancing of the ferrite disc's thickness to be made, with the consequent higher isolations then being possible.

6.1.5 Appendix I

Theoretical Context

Reference [18] gives a good description of microwave propagation in ferrites. Briefly, the macroscopic property of the ferrite material that is relevant to this work, and to the fact that ferrite materials can exhibit Faraday rotation, is the ferrite's anisotropic permeability. The permeability of ferrite material cannot be described by a single number, but rather is described by a tensor.

It can be shown that for a TEM wave propagating within a ferrite medium, in the direction of an applied static magnetic field, that the *natural propagation modes* for the TEM wave are left and right-circularly polarised modes. The permeability for these two modes is different, and thus the propagation constants are different, and net rotation of an incident linearly polarised TEM wave is to be expected. This net rotation is given by the equation

$$\theta = \frac{(\beta_- - \beta_+)\ell}{2}$$

where β_{\pm} are the propagation constants for the left and right-circularly polarised waves, respectively, and ℓ is the ferrite thickness. A practical ferrite medium has finite losses and this significantly influences propagation. Again from reference [18], the propagation constants $\gamma_{\pm} = \alpha_{\pm} + j\beta_{\pm}$ for circularly polarised waves will have unequal attenuation constants. Provided the frequency of the propagating wave is much greater than the resonant frequency of the ferrite material, the Faraday rotation can be shown to be independent of frequency. The resonant frequency (see section 6.1.2.3) is 12.9 GHz, that is, approximately 0.1 of the operating frequency. The rotation in this situation can therefore be taken as essentially independent of frequency and given by

$$\theta = \frac{\ell \sqrt{\epsilon_r} \gamma \mu_0 M_s}{2c}$$

where

ℓ	ferrite thickness
ϵ_r	relative dielectric constant
γ	gyromagnetic ratio
μ_o	permeability of free space
M_s	saturated magnetisation
c	speed of light in free space

A final comment here is necessary. The theory presented by Collin [18] involves the application of a static magnetic field to the ferrite, without which no torque will be produced to cause precession of the electron's angular momentum, (the key to the anisotropy of the ferrite's permeability). In the case of the ferrite disc explored here, no static magnetic field has been applied. The strontium hexagonal ferrite material used here indeed has it's own anisotropic static field. A full theoretical treatment would probably involve a consideration of retarded fields, and it should be noted that the field strength at any particular point within the ferrite disc, is only significantly affected by fields originating from within about one and a half times the disc's thickness away.

6.1.6 Appendix II

Circulator Losses and Reflections

The parameter G_{21} represents the forward path power transfer coefficient for the circulator. It includes three component parts, namely ferrite absorption loss, ferrite reflection losses and optics losses. This latter includes lens reflections and absorptions, and beam coupling efficiencies. The method for extracting these component parts from G_{21} is now described. Let e represent the ferrite absorption loss, $(1 - \Gamma^2)$ represent the reflection losses, and η represent the optics losses. Furthermore, let L represent the insertion loss. Thus

$$\begin{aligned} G_{21} &= \eta e (1 - \Gamma^2) \\ &= \eta L \end{aligned}$$

Now Γ^2 , the power reflection coefficient, has two orthogonal components, a co-polar reflection and a cross-polar reflection, as described in section 6.1.3.1. That is

$$\Gamma^2 = \Gamma_{co}^2 + \Gamma_X^2$$

where Γ_{co}^2 is the reflection component with the same polarisation as the incident beam (reflection from first ferrite surface) and Γ_X^2 is the reflection component with polarisation orthogonal to that of the incident beam, (reflection from the second ferrite surface). Two approximations are now made, before expressing the relevant power transfer coefficients in terms of these orthogonal reflection coefficients. Firstly, any second order terms are considered to contribute negligible effect to the various relationships expressed below, and secondly that with regard to G_{11} and G_{31} , the *ferrite* reflections significantly dominate in determining their magnitude, since the associated optics losses are at least ten times smaller in magnitude. This second approximation is not valid for G_{21} . Thus

$$\begin{aligned} G_{11} &= \Gamma_{co}^2 \\ G_{21} &= \eta e(1 - \Gamma_{co}^2 - \Gamma_X^2) \\ G_{31} &= e^2 \Gamma_X^2 (1 - \Gamma_{co}^2) \end{aligned}$$

and thus

$$L = e(1 - \Gamma_{co}^2 - \Gamma_X^2)$$

Substitution of the equation for G_{11} into the equations for G_{31} and L provides two equations with two unknowns, Γ_X^2 and e :

$$\begin{aligned} L &= e(1 - G_{11} - \Gamma_X^2) \\ G_{31} &= e^2 \Gamma_X^2 (1 - G_{11}) \end{aligned}$$

These two equations are non-linearly related. It can be shown that

$$e = \frac{L + \sqrt{L^2 + 4G_{31}}}{2(1 - G_{11})}$$

Finally, the input vswr at an input port (e.g. port 1) is defined by the co-polar reflection coefficient, Γ_{co} . That is

$$\text{vswr} = \frac{1 + \sqrt{G_{11}}}{1 - \sqrt{G_{11}}}$$

6.2 The Performance of a Large Area Faraday Rotator

This section essentially provides an update on the performance that is able to be obtained from a millimetre wave quasi-optical Faraday rotator when it is being used as an isolator or circulator. The development of these Faraday rotators was carried out

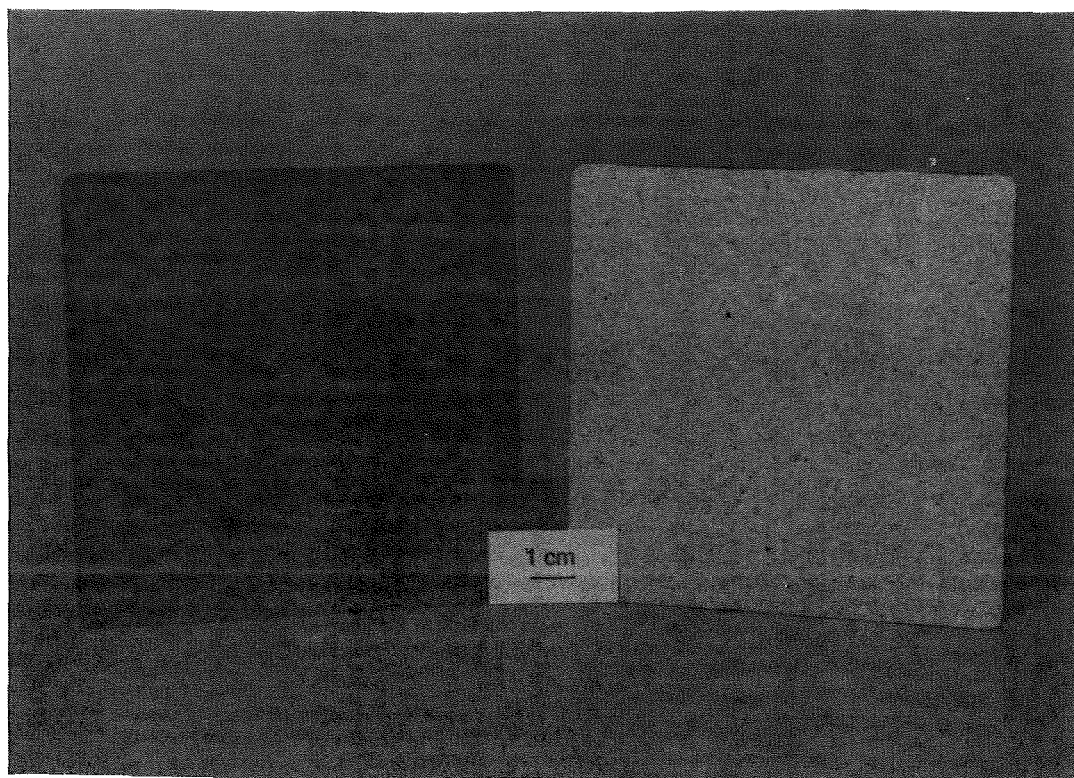


Figure 6.17: A photograph of two 100 mm \times 100 mm ferrite sheets. The right hand sheet has the quarter-wave Fluorosint matching on it.

by both myself and Dr. Graham Smith. The performance results presented here are based on measurements made by Dr. Graham Smith.

The ferrite material used is again Ferroxdure 330, along with an equivalent—that is, the ferrite materials used were permanently magnetised hexagonal strontium ferrites, and the rates of rotation for linearly polarised electromagnetic waves moving through them was $30^\circ/\text{mm}$. For large areas, it has proved more convenient to produce square sheets rather than discs—see figure 6.17. The specific dimensions for the large area ferrite sheets developed are 100 mm \times 100 mm with a thickness of 1.50 mm. Fluorosint was again used for quarter-wave matching the ferrite material to free space. A very thin and dilute layer of Araldite, an epoxy adhesive, was used to fix the Fluorosint sheets to the ferrite sheet. Table 6.1 provides a summary of the measured performance. Isolations of up to 60 dB have been measured, and v_{swr} 's less than 1.1 have also been measured. Quarter-wave matching sheets for operation at 140 GHz have been successfully developed, and matching at even higher frequencies is possible. The larger area means that the power handling capability is also increased. Finally, a difference in

Large Area Faraday Rotator	
Isolation	> 40 dB
Absorption Loss	0.2–0.4 dB
VSWR	1.1–1.3
Bandwidth	20% at 100 GHz

Table 6.1: The performance of a 100 mm \times 100 mm Faraday rotator.

the levels of absorption between **Ferroxdure 330** and its equivalents has been noted, with **Ferroxdure 330** having the lowest absorption. There are some differences between the various ferrite materials, and these differences involve the use of various proprietary additives which aid the sintering process. Among other things, the additives help to minimise flaws (i.e. cracks) in the final sintered materials.

These new large area Faraday rotators are very easy to use as they can be placed anywhere within a quasi-optical circuit. This represents a real advance on the work reported within the previous section.

6.3 The Magnetic Field Strength within a Ferrite Disc

A result is established within this section that was merely asserted within section 6.1.5, namely that the magnetic field strength at any particular point within a permanently magnetised and thin ferrite disc (or sheet), is only significantly affected by fields originating within the local vicinity of that point. The extent of this localisation for a thin disc is about one and a half times the thickness of the disc. This also means that the fringing fields at the edge of a thin ferrite disc are of negligible significance for the Faraday rotation mechanism exploited within this work.

The Theoretical Development

As a lead into this development, consider the simple problem of determining the magnetic field strength within a plane perpendicular to a single magnetic dipole moment. Thus consider the geometry of figure 6.18, where the magnetic dipole moment is assumed to result from two equal and opposite fictitious magnetic poles (or magnetic

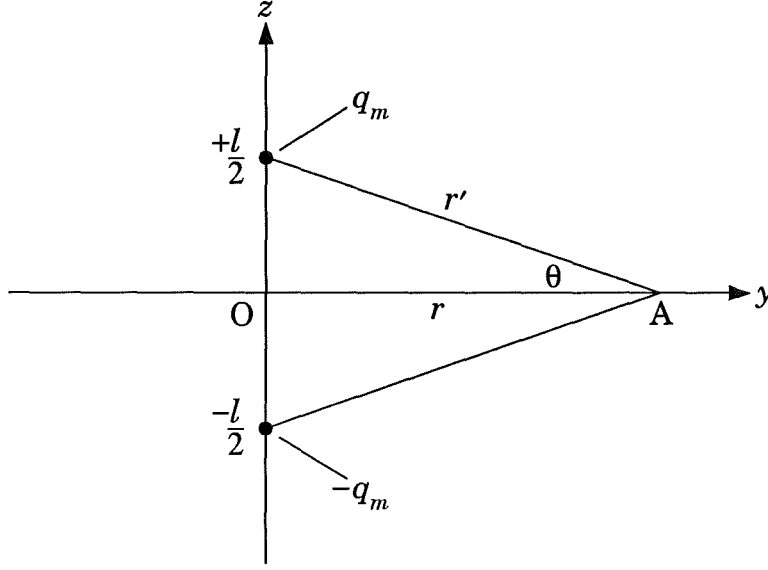


Figure 6.18: The geometry for evaluating the magnetic field strength in a plane perpendicular to a magnetic dipole moment.

charges). The thickness between these poles will later represent the thickness of the ferrite disc. Let \mathbf{m} represent the magnetic dipole moment vector, and let q_m represent the magnitude of the magnetic pole strength (cf. q for electric charge). Thus if ℓ is the distance between the magnetic poles, and $\hat{\mathbf{u}}_z$ the unit vector in the z -direction, then \mathbf{m} is given by

$$\mathbf{m} = q_m \ell \hat{\mathbf{u}}_z \quad (6.1)$$

and it's direction is from the lower negative pole up the z -axis to the positive pole. From figure 6.18, if r' is the distance from either pole to the point A within the plane perpendicular to the dipole, that is the XY-plane, and if r is the distance OA from the origin O to the point A, then

$$r'^2 = r^2 + \frac{\ell^2}{4} \quad (6.2)$$

Let $\hat{\mathbf{r}}'_\pm$ represent the unit vectors in the direction from the poles to the point A. Thus

$$\hat{\mathbf{r}}'_\pm = \hat{\mathbf{u}}_y \cos \theta \mp \hat{\mathbf{u}}_z \sin \theta \quad (6.3)$$

Thus the contribution to the magnetic field strength at A by the positive magnetic pole is

$$\mathbf{B}_+ = \hat{\mathbf{r}}'_+ \frac{\mu_0 q_m}{4\pi} \left(\frac{1}{r'^2} \right)$$

$$\begin{aligned}
&= \hat{\mathbf{r}}'_+ \frac{\mu_o q_m}{4\pi} \left(\frac{1}{r^2 + \frac{\ell^2}{4}} \right) \\
&= \frac{\mu_o q_m}{4\pi \left(r^2 + \frac{\ell^2}{4} \right)} (\hat{\mathbf{u}}_y \cos \theta - \hat{\mathbf{u}}_z \sin \theta)
\end{aligned} \tag{6.4}$$

and similarly for the negative magnetic pole

$$\mathbf{B}_- = \frac{-\mu_o q_m}{4\pi \left(r^2 + \frac{\ell^2}{4} \right)} (\hat{\mathbf{u}}_y \cos \theta + \hat{\mathbf{u}}_z \sin \theta) \tag{6.5}$$

Therefore the total field at A is given by

$$\begin{aligned}
\mathbf{B} &= \mathbf{B}_+ + \mathbf{B}_- \\
&= \frac{-\mu_o q_m \sin \theta}{2\pi \left(r^2 + \frac{\ell^2}{4} \right)} \hat{\mathbf{u}}_z
\end{aligned} \tag{6.6}$$

and substituting in \mathbf{m} from equation 6.1 gives

$$\mathbf{B} = \frac{-\mu_o \mathbf{m} \sin \theta}{2\pi \ell \left(r^2 + \frac{\ell^2}{4} \right)} \tag{6.7}$$

and with

$$\sin \theta = \frac{\ell}{2 \left(r^2 + \frac{\ell^2}{4} \right)^{\frac{1}{2}}} \tag{6.8}$$

\mathbf{B} can be expressed in the following general form

$$\mathbf{B} = \frac{-\mu_o \mathbf{m}}{4\pi \left(r^2 + \frac{\ell^2}{4} \right)^{\frac{3}{2}}} \tag{6.9}$$

If $\ell = 0$ then this result is just the standard result as derived say for example, in reference [19].

Consider now the case where the magnetic field strength is to be evaluated at the origin O, for a large number of magnetic dipole moments distributed evenly and concentrically about O, as depicted within figure 6.19. Let the magnitude of the magnetic dipole moment that makes a contribution to the magnetic field strength at O be

$$|\mathbf{m}| = m = M_A \delta A \tag{6.10}$$

where M_A is the magnetic dipole moment strength per unit area, and δA is an infinitesimally small area on the disc as shown in figure 6.19. If the contributions from each δA

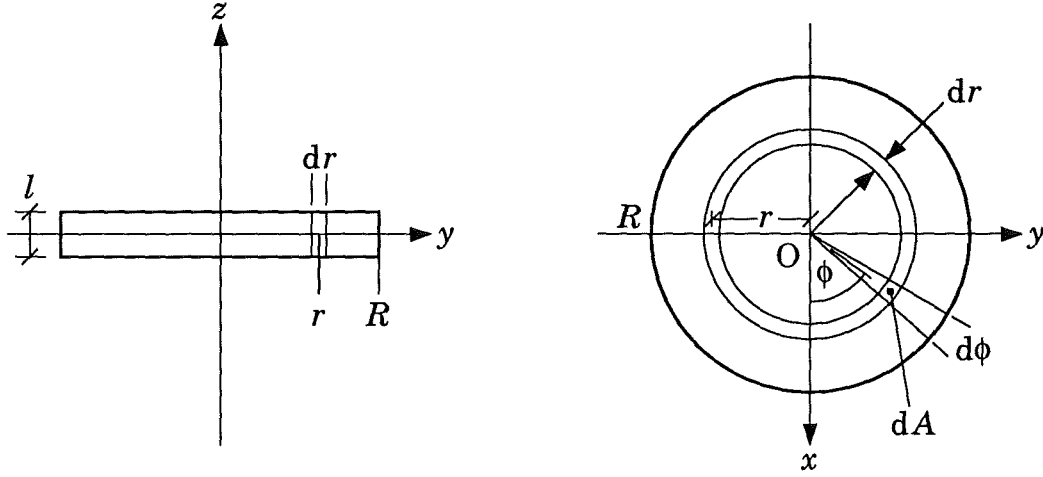


Figure 6.19: The geometry for a ferrite disc.

element are summed, or in the limit integrated, then the magnetic field strength \mathbf{B} at O is given by

$$\begin{aligned}
 \mathbf{B} &= - \int_0^R \int_0^{2\pi} \frac{\mu_o M_A \hat{\mathbf{u}}_z dA}{4\pi \left(r^2 + \frac{\ell^2}{4} \right)^{\frac{3}{2}}} \\
 &= - \hat{\mathbf{u}}_z \frac{\mu_o M_A}{2} \int_0^R \int_0^{2\pi} \frac{dr r d\phi}{4\pi \left(r^2 + \frac{\ell^2}{4} \right)^{\frac{3}{2}}} \\
 &= - \hat{\mathbf{u}}_z \frac{\mu_o M_A}{2} \int_0^R \frac{r dr}{\left(r^2 + \frac{\ell^2}{4} \right)^{\frac{3}{2}}}
 \end{aligned} \tag{6.11}$$

which evaluates to

$$\mathbf{B} = - \hat{\mathbf{u}}_z \mu_o M_v \left(1 - \left(\frac{4R^2}{\ell^2} + 1 \right)^{-\frac{1}{2}} \right) \tag{6.12}$$

where $M_v = M_A/\ell$ and is the magnetic dipole moment strength per unit volume (i.e. the magnetic dipole moment volume density). Note that in the trivial case of $R = 0$, $\mathbf{B} = 0$ and that for $R \rightarrow \infty$, $\mathbf{B} \rightarrow \mathbf{B}_\infty$ where

$$\mathbf{B}_\infty = \frac{- \hat{\mathbf{u}}_z \mu_o M_A}{\ell} \tag{6.13}$$

The issue for which this development was made, can now be stated in the following way: *How small can the radius R of the disc become, before the reduction of \mathbf{B} from*

\mathbf{B}_∞ becomes significant? For example, choose the arbitrary criterion of allowing \mathbf{B} to be reduced by $1/e$, that is, let

$$\mathbf{B} = \left(1 - \frac{1}{e}\right) \mathbf{B}_\infty \quad (6.14)$$

from which it can be shown that

$$\begin{aligned} R &= \frac{\ell}{2} (e^2 - 1)^{\frac{1}{2}} \\ &\approx 1.26\ell \end{aligned} \quad (6.15)$$

Thus it is seen that for a sheet of infinite (or large) extent, and for any point within that sheet, 63% of the magnetic field strength that exists at that point has its origin from only relatively local magnetic dipole moments, that is, from those within a radius of 1.26 times the thickness of the ferrite sheet. Any arbitrary criterion could be used here, but the essential feature of localisation has now been established.

6.4 Reflection Properties in Detail

6.4.1 Introduction

The detailed reflection properties of a ferrite sheet have been both modelled and measured. The modelling work has been done entirely by myself and the measurements were performed by Dr. Graham Smith. While this work is interesting in itself, it should be viewed as a precursor to further modelling involving transmission properties and multiple layer matching structures. By modelling the transmission properties in detail, the levels of depolarisation for given levels of mismatch can be predicted, and broader bandwidth ferrite matching could be achieved with the help of detailed models of multiple layer matching structures.

6.4.2 A Transmission Line Model

6.4.2.1 The Equivalent Circuit

A schematic diagram of the quasi-optical circuit that is to be modelled is given in figure 6.20(a). The equivalent transmission line circuit is given in figure 6.20(b). Both the equivalent source and load impedances are assumed to be equal to the characteristic free space impedance Z_0 , where

$$Z_0 = \sqrt{\frac{\mu_0}{\epsilon_0}} \quad (6.16)$$

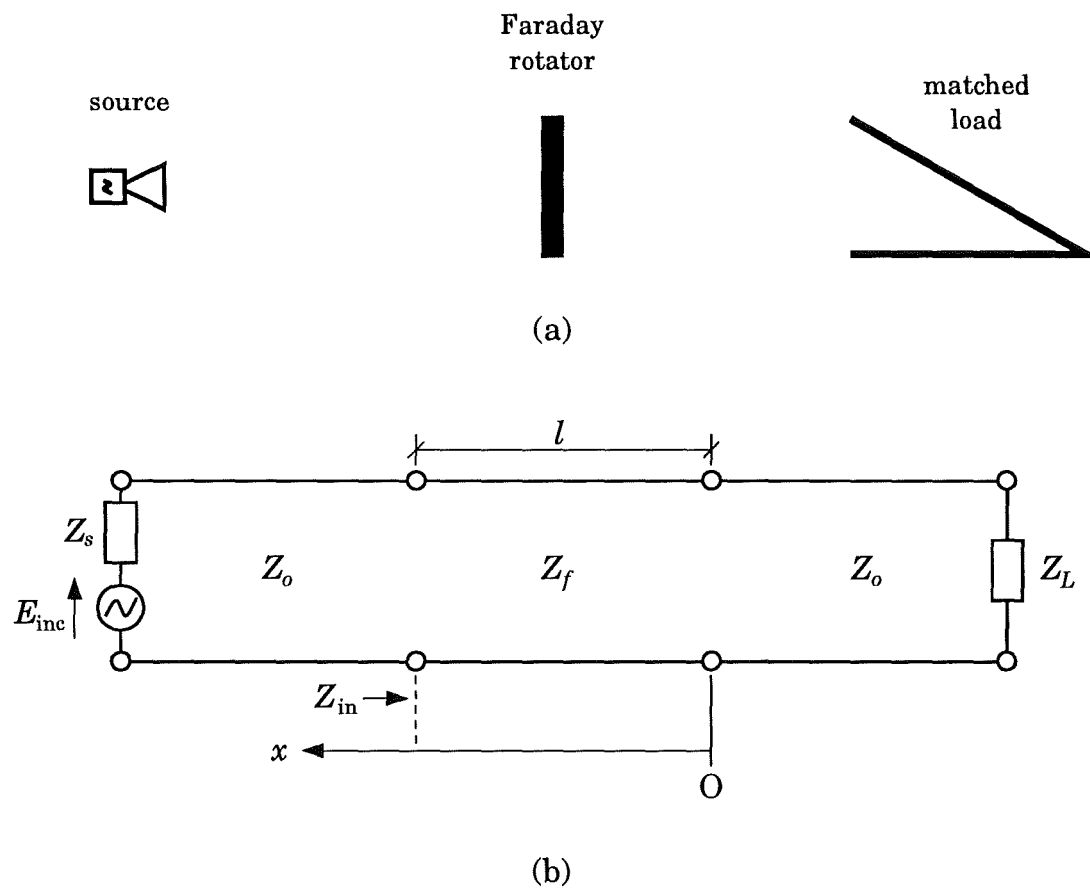


Figure 6.20: (a) A schematic diagram of the quasi-optical circuit; and (b) the equivalent transmission line circuit.

$$\approx 377 \Omega$$

and where $\mu_o = 400\pi \text{ nH m}^{-1}$ and $\epsilon_o = 8.854 \text{ pF m}^{-1}$ are the free space permeability and permittivity respectively. This means that there are no reflections from the load and that reflections from the ferrite sheet are completely absorbed at the source and not reflected back again towards the ferrite sheet. The characteristic impedance of the ferrite material is represented by Z_f , where Z_f is given by

$$Z_f = \sqrt{\frac{\mu}{\epsilon}} \quad (6.17)$$

where μ and ϵ are the complex permeability and permittivity of the ferrite medium respectively, and are given by

$$\mu = \mu_o \mu_r = \mu_o(\mu'_r - j\mu''_r) \quad (6.18)$$

and

$$\epsilon = \epsilon_o \epsilon_r = \epsilon_o \left(\epsilon'_r - j \left(\epsilon''_r + \frac{\sigma}{\omega \epsilon_o} \right) \right) \quad (6.19)$$

Magnetic and dielectric hysteresis losses are represented in the above by the terms μ''_r and ϵ''_r respectively and conduction losses are represented by the $\sigma/\omega\epsilon_o$ term where σ is the conductivity in U m^{-1} and ω is the frequency in rad s^{-1} . If the losses are primarily conduction losses⁵, then $\mu''_r = 0$ and $\epsilon''_r = 0$ and thus the characteristic impedance of the ferrite material is given by⁶

$$\begin{aligned} Z_f &= Z_o \sqrt{\frac{\mu'_r}{\epsilon'_r}} \left(1 - j \frac{\sigma}{\omega \epsilon_o \epsilon'_r} \right)^{-\frac{1}{2}} \\ &= Z_o \sqrt{\frac{\mu'_r}{2\epsilon'_r}} \left\{ \left[\left(1 + \left(\frac{\sigma}{\omega \epsilon_o \epsilon'_r} \right)^2 \right)^{\frac{1}{2}} + 1 \right]^{\frac{1}{2}} + j \left[\left(1 + \left(\frac{\sigma}{\omega \epsilon_o \epsilon'_r} \right)^2 \right)^{\frac{1}{2}} - 1 \right]^{\frac{1}{2}} \right\} \\ &= X_f + jY_f \end{aligned} \quad (6.20)$$

⁵This assumption seems to work well, but supplementary experimental evidence would be required to properly justify it. The likely alternatives are for the losses to be either predominantly magnetic or possibly some mix of magnetic and conduction losses. Dielectric hysteresis losses are unlikely to be involved at all.

⁶Note that the principal square root of a complex number z is given by [20, §3.7.27]

$$z^{\frac{1}{2}} = \left(\frac{1}{2}(r+x) \right)^{\frac{1}{2}} \pm j \left(\frac{1}{2}(r-x) \right)^{\frac{1}{2}}$$

The ferrite material is considered to be a good dielectric material[21, pages 445–449], that is

$$\frac{\sigma}{\omega\epsilon_o\epsilon'_r} \ll 1 \quad (6.21)$$

and so only the first term of the Binomial expansion of the equation for X_f will be needed in order to provide sufficient accuracy. Therefore

$$X_f \simeq Z_o \sqrt{\frac{\mu'_r}{\epsilon'_r}} \left(1 + \frac{1}{8} \left(\frac{\sigma}{\omega\epsilon_o\epsilon'_r} \right)^2 \right) \quad (6.22)$$

and

$$Y_f \simeq Z_o \sqrt{\frac{\mu'_r}{\epsilon'_r}} \frac{\sigma}{2\omega\epsilon_o\epsilon'_r} \quad (6.23)$$

The complex propagation constant γ is defined by the wave equation[22]

$$\nabla^2 \mathbf{E} = \gamma^2 \mathbf{E} \quad (6.24)$$

and where

$$\gamma^2 = -\omega^2 \mu \epsilon \quad (6.25)$$

Again, assuming that there are only conduction losses, and with c representing the speed of light in free space, γ becomes

$$\begin{aligned} \gamma &= j \frac{\omega}{c} \sqrt{\mu'_r \epsilon'_r} \left(1 - j \frac{\sigma}{\omega\epsilon_o\epsilon'_r} \right)^{\frac{1}{2}} \\ &= \frac{\omega}{c} \sqrt{\frac{\mu'_r \epsilon'_r}{2}} \left\{ \left[\left(1 + \left(\frac{\sigma}{\omega\epsilon_o\epsilon'_r} \right)^2 \right)^{\frac{1}{2}} - 1 \right]^{\frac{1}{2}} + j \left[\left(1 + \left(\frac{\sigma}{\omega\epsilon_o\epsilon'_r} \right)^2 \right)^{\frac{1}{2}} + 1 \right]^{\frac{1}{2}} \right\} \\ &= \alpha + j\beta \end{aligned} \quad (6.26)$$

where α is an attenuation constant with units of Nepers per metre (N m^{-1}) and β is a phase constant with units of radians per metre (rad m^{-1}). If the same condition 6.21 is used, then

$$\alpha \simeq \frac{Z_o \sigma}{2} \sqrt{\frac{\mu'_r}{\epsilon'_r}} \quad (6.27)$$

and

$$\beta \simeq \frac{\omega \sqrt{\mu'_r \epsilon'_r}}{c} \left(1 + \frac{1}{8} \left(\frac{\sigma}{\omega\epsilon_o\epsilon'_r} \right)^2 \right) \quad (6.28)$$

The resultant input impedance Z_{in} at the first surface of the ferrite sheet depends upon Z_o , Z_f , γ and ℓ , where ℓ is the thickness of the ferrite sheet, or equivalently, the

length of the transmission line segment having characteristic impedance Z_f . Thus Z_{in} is given by [21, page 406]

$$Z_{in} = Z_f \frac{Z_o + Z_f \tanh \gamma \ell}{Z_f + Z_o \tanh \gamma \ell} \quad (6.29)$$

Thus the field reflectivity ρ at the first ferrite surface is given by

$$\rho = \frac{Z_{in} - Z_o}{Z_{in} + Z_o} \quad (6.30)$$

and the power reflectivity, or reflectance \mathcal{R} is

$$\mathcal{R}_{in} = \rho^2 \quad (6.31)$$

There are three parameters that must be known in order to evaluate \mathcal{R} as a function of frequency. They are

1. The refractive index n_f of the ferrite material, where $n_f = \sqrt{\mu'_r \epsilon'_r}$ and $\mu'_r = 1$ for this ferrite material in its unmagnetised state.
2. The thickness ℓ of the ferrite sheet.
3. The attenuation constant α_ℓ as measured for a linearly polarised electromagnetic wave. This is needed in order to calculate the conductivity σ . From equation 6.27 $\sigma = 2\alpha_\ell n_f / Z_o$.

A FORTRAN program called FE1 (see appendix C) has been produced based upon the foregoing development. It models the reflection properties of an unmagnetised ferrite sheet. Results from this model are provided within section 6.4.3.

6.4.2.2 Polarisation Duality

A magnetised ferrite sheet, with the direction of magnetisation being in the direction of propagation, has a dual-valued permeability. The two values correspond to the two mutually orthogonal circular polarisation modes. The polarisation modes are defined as follows: if the electric field vector of a circularly polarised electromagnetic wave is rotating *clockwise* about its propagation axis as it *approaches* an observer, then the mode is called left-hand circular (LHC) or negative circular polarisation [21, pages 495–497], and *vice versa* for RHC or positive circular polarisation⁷.

⁷This definition is the IEEE definition and is opposite to the classical optics definition.

For the case where the magnetic losses are assumed to be negligible, the dual-valued permeability $\mu'_{r\pm}$ is given by reference [18, page 291]

$$\mu'_{r\pm} = 1 + \frac{\omega_m}{\omega_m \mp \omega} \quad (6.32)$$

where ω_m is the frequency of gyromagnetic resonance. This gyromagnetic resonance frequency is dependent upon the magnetic field strength B_s in the material, which for the fully and permanently magnetised ferrite material considered here, is the saturated magnetisation level. Thus ω_m is given by

$$\omega_m = \Upsilon B_s \quad (6.33)$$

where Υ is the gyromagnetic ratio and is equal to the ratio of the electronic charge and the mass of an electron, that is, $\Upsilon = 175.9 \text{ GC kg}^{-1}$. Hence Z_f , γ and Z_{in} are dual-valued quantities, and thus the reflectance is also dual-valued. All of the same equations apply, but μ'_r must be replaced by $\mu'_{r\pm}$. Two additional parameters are required to be known in order to evaluate \mathcal{R}_{\pm} . The magnetic field strength B_s must be known, and the frequency at which the attenuation factor α_ℓ (linearly polarised) was measured. This frequency must be known in order to evaluate the conductivity σ . From equation 6.27 the following relationship can be found

$$\frac{\alpha_-}{\alpha_+} = \sqrt{\frac{\mu'_{r-}}{\mu'_{r+}}} \quad (6.34)$$

It can be shown that

$$\alpha_\ell = \alpha_+ + \alpha_- \quad (6.35)$$

and so

$$\alpha_+ = \frac{\alpha_\ell}{1 + \frac{\alpha_-}{\alpha_+}} \quad (6.36)$$

$$= \frac{\alpha_\ell}{1 + \sqrt{\frac{\mu'_{r-}}{\mu'_{r+}}}} \quad (6.37)$$

which can be used within equation 6.27 to calculate the conductivity σ .

The dual-valued reflectance \mathcal{R}_{\pm} is of course for the RHC and LHC polarisation modes. However, for a linearly polarised incident electromagnetic wave—which is what is most commonly used in practise—the linear co-polar and cross-polar (X-polar) reflectances \mathcal{R}_{co} , \mathcal{R}_{X} are of more interest. Also, in general the resultant reflected wave

will be elliptically polarised, and therefore the degree of ellipticity and the tilt of the major axis of the ellipse are quantities that are of interest. The following development provides the required transformation equations.

Let \mathbf{E}_i represent the incident electric field vector, which is also a phasor quantity with the $e^{j\omega t}$ term suppressed. In addition, let \mathbf{E}_i be orientated along the x -axis so that

$$\mathbf{E}_i = \hat{\mathbf{x}}E \quad (6.38)$$

where $\hat{\mathbf{x}}$ is the unit vector in the x -direction and E is the incident electric field phasor. This linearly polarised electromagnetic wave can be represented as a summation of the two mutually orthogonal circularly polarised modes in the following way

$$\mathbf{E}_i = \frac{1}{2}\mathbf{E}_{i+} + \frac{1}{2}\mathbf{E}_{i-} \quad (6.39)$$

where

$$\begin{aligned} \mathbf{E}_{i+} &= \hat{\mathbf{x}}E + \hat{\mathbf{y}}Ee^{-j\frac{\pi}{2}} \\ &= \hat{\mathbf{x}}E + \hat{\mathbf{y}}jE \end{aligned} \quad (6.40)$$

and

$$\begin{aligned} \mathbf{E}_{i-} &= \hat{\mathbf{x}}E + \hat{\mathbf{y}}Ee^{j\frac{\pi}{2}} \\ &= \hat{\mathbf{x}}E - \hat{\mathbf{y}}jE \end{aligned} \quad (6.41)$$

The dual-valued reflectivity ρ_{\pm} can now be used with \mathbf{E}_i in this form. Hence, if the reflected wave is represented by $\mathbf{E}_{r\pm}$, then

$$\mathbf{E}_{r+} = \rho_+ \frac{\mathbf{E}_{i+}}{2} \quad (6.42)$$

$$= \hat{\mathbf{x}}\rho_+E - \hat{\mathbf{y}}j\rho_+E \quad (6.43)$$

and

$$\mathbf{E}_{r-} = \rho_- \frac{\mathbf{E}_{i-}}{2} \quad (6.44)$$

$$= \hat{\mathbf{x}}\rho_-E + \hat{\mathbf{y}}j\rho_-E \quad (6.45)$$

Thus the total reflected field is

$$\mathbf{E}_r = \hat{\mathbf{x}} \left(\frac{\rho_- + \rho_+}{2} \right) E + \hat{\mathbf{y}}j \left(\frac{\rho_- - \rho_+}{2} \right) E \quad (6.46)$$

The co-polar and X-polar reflectivities are thus given as

$$\rho_{\text{co}} = \frac{E_{rx}}{E} = \frac{\rho_- + \rho_+}{2} \quad (6.47)$$

and

$$\rho_{\text{X}} = \frac{E_{ry}}{E} = \frac{\rho_- - \rho_+}{2} \quad (6.48)$$

Note that ρ_{\pm} are complex quantities (e.g. $\rho_+ = \rho_{u+} + \rho_{v-}$) and so

$$|\rho_{\text{co}}| = \frac{1}{2} \left((\rho_{u-} + \rho_{u+})^2 + (\rho_{v-} + \rho_{v+})^2 \right)^{\frac{1}{2}} \quad (6.49)$$

and

$$|\rho_{\text{X}}| = \frac{1}{2} \left((\rho_{u-} - \rho_{u+})^2 + (\rho_{v-} - \rho_{v+})^2 \right)^{\frac{1}{2}} \quad (6.50)$$

The resultant reflected electric field vector \mathbf{E}_r in general traces out an ellipse. Two parameters are needed to define the polarisation state of an electromagnetic wave, provided that it is not only partially polarised, and various representations are possible. The Poincaré Sphere representation has been chosen here for its elegance and utility. The two parameters are τ , the tilt angle of the major axis of the ellipse with reference to the x -direction, and ε , an angular measure of the ellipticity of the ellipse. These two parameters are related to the phase δ between the x and y components of \mathbf{E}_r , and to ξ , the arctangent of the ratio of the magnitudes of the x and y components of \mathbf{E}_r . Thus the phase angle δ is given by

$$\delta = \tan^{-1} \left(\frac{\rho_{u-} - \rho_{u+}}{\rho_{v+} - \rho_{v-}} \right) - \tan^{-1} \left(\frac{\rho_{v-} + \rho_{v+}}{\rho_{u-} + \rho_{u+}} \right) \quad , -180^\circ \leq \delta \leq 180^\circ \quad (6.51)$$

and

$$\xi = \tan^{-1} \left(\frac{\rho_{\text{X}}}{\rho_{\text{co}}} \right) \quad , 0^\circ \leq \xi \leq 90^\circ \quad (6.52)$$

The relationship between (δ, ξ) and (τ, ε) involves spherical trigonometric geometry. The relationship is simply stated here—see reference [21, page 500], from which

$$\tan 2\tau = \tan 2\xi \cos \delta \quad , 0^\circ \leq \tau \leq 180^\circ \quad (6.53)$$

and

$$\sin 2\varepsilon = \sin 2\xi \sin \delta \quad , -45^\circ \leq \varepsilon \leq 45^\circ \quad (6.54)$$

Note also that the axial ratio (AR), which is the ratio of the major to minor axis components, is given by

$$\text{AR} = \cot \varepsilon \quad , 1 \leq \text{AR} \leq \infty \quad (6.55)$$

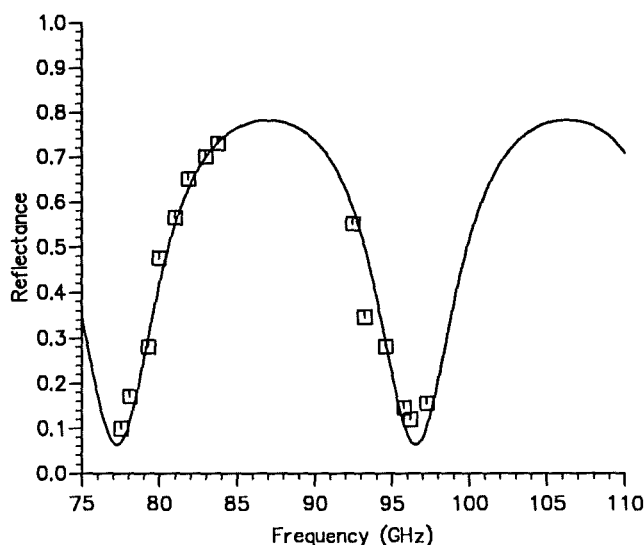


Figure 6.21: The reflectance as a function of frequency for an unmagnetised ferrite sheet of thickness 1.49 mm ($n_f = 5.21$).

A FORTRAN program called FE2 (see appendix D) has been produced, that is based upon all of the foregoing development. FE2 models the reflection properties of a polarisation active ferrite sheet, and results from this model are given within the next section.

6.4.3 Ferrite Reflectances

6.4.3.1 Unmagnetised Ferrite Sheet

Measurements⁸ were made for two ferrite sheets having slightly different thicknesses (1.49 mm and 1.54 mm). The attenuation constant α_ℓ has been measured for the ferrite material and is 800 dB m^{-1} . A Fabry-Perot based analysis of the measurement data yielded a refractive index n_f of 5.21 and this value provided the best fit of the FE1 model results to the measurement data. Figures 6.21 and 6.22 show these results and it is seen that there is good agreement between the measurements and the FE1 model results.

⁸All measurements were made by Dr. Graham Smith. The measurements were made on a complex impedance nulling bridge developed by Dr. Andy Harvey[23].

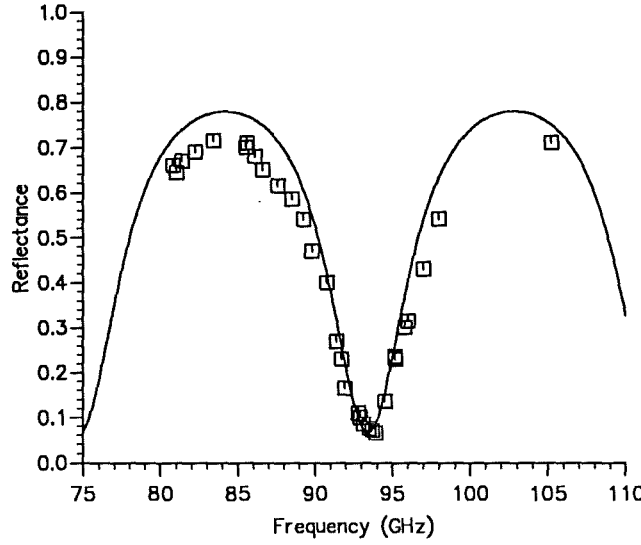


Figure 6.22: The reflectance as a function of frequency for an unmagnetised ferrite sheet of thickness 1.54 mm ($n_f = 5.21$).

6.4.3.2 Magnetised Ferrite Sheet

Measurements of reflectance were made for one magnetised ferrite sheet (of thickness 1.54 mm) using mutually orthogonal circularly polarised incident electromagnetic waves. The attenuation constant α_ℓ was set to 800 dB m^{-1} , and this time it was found that a refractive index of 4.80 provided the best fit. (Recall that different ferrite materials are involved, namely Ferroxidure 330 and various equivalents.) Figure 6.23 shows these measurements along with the FE2 model results. Figure 6.24 has FE2 model results of the previous figure but now with the FE1 model result for the same ferrite sheet (i.e. in its unmagnetised state) superimposed upon it. Note how the reflectances for the circularly polarised modes have *split* to either side of this curve. This is as would be expected from the form of the dual-valued permeability given in equation 6.32; (i.e. where $\mu'_{r\pm}$ has two values split either side of unity).

Some measurements were made on a magnetised ferrite sheet with a refractive index of 5.21 and of thickness 1.57 mm and this time with a linearly polarised incident electromagnetic wave. The attenuation constant is again taken to be 800 dB m^{-1} and the frequency at which this was measured is taken as 94 GHz, though it is in fact approximately constant for the whole bandwidth being considered. The satu-

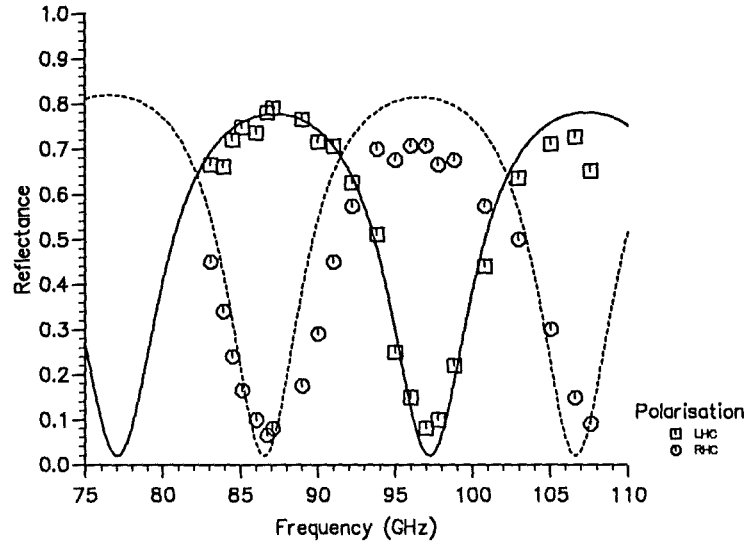


Figure 6.23: The reflectance as a function of frequency for a magnetised ferrite sheet, in terms of circularly polarised modes ($n_f = 4.80$, $\ell = 1.54$ mm).

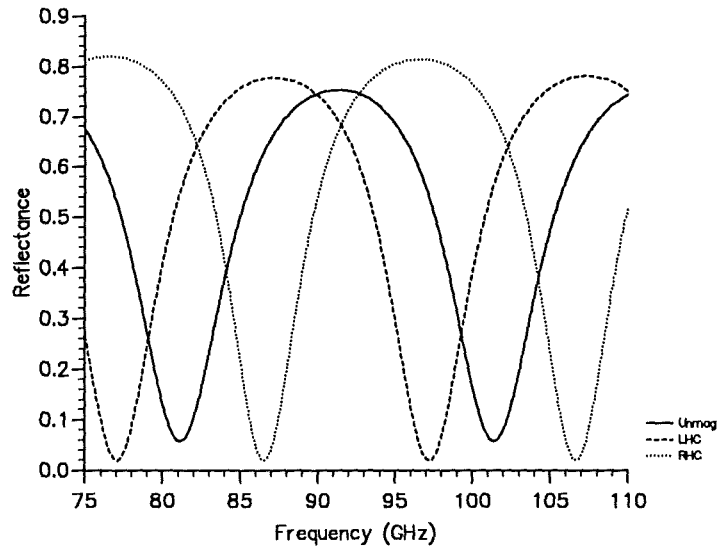


Figure 6.24: The reflectance of a magnetised ferrite sheet compared with that of the same ferrite sheet in an unmagnetised state ($n_f = 4.80$, $\ell = 1.54$ mm).

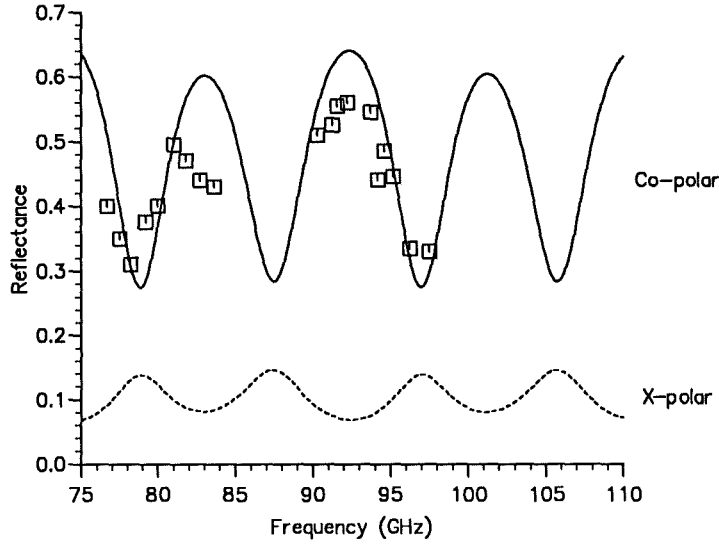


Figure 6.25: The reflectance as a function of frequency for a magnetised ferrite sheet in terms of orthogonal linear polarisation states ($n_f = 5.21$, $\ell = 1.57$ mm).

rated magnetisation[13] is taken as 0.334 T. Figure 6.25 shows these results along with the FE2 model results. Figure 6.26 shows the FE2 model results of the resultant polarisation state of the reflected wave as a function of frequency, in terms of the Poincaré parameters, the tilt angle τ , and ε the angle specifying the amount of power in the angle orthogonal to τ . The rotational sense of the ellipse is given by the sign of ε ($+$ \Rightarrow LH, $-$ \Rightarrow RH).

References

- [1] R. Meredith and G. H. Preece, *Millimetre and Submillimetre Waves*. Editor: F. A. Benson, ILIFFE BOOKS LTD, pp. 393–395, 1969, chapter 20.
- [2] J. C. Wiltse, *Infrared and Millimeter Waves—Volume 4*. Editors: K. J. Button and J. C. Wiltse, Academic Press, p. 10, 1981, chapter 1.
- [3] E. K. Reedy and G. W. Ewell, *Infrared and Millimeter Waves—Volume 4*. Editor: K. J. Button and J. C. Wiltse, Academic Press, pp. 34–35, 1981, chapter 2.

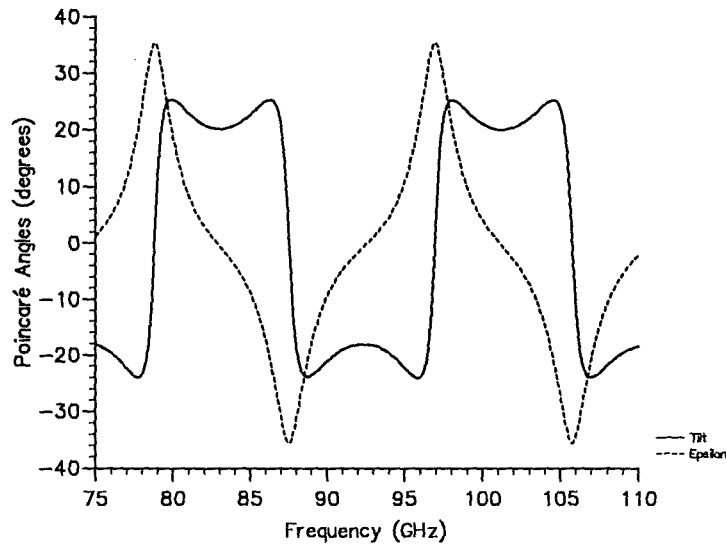


Figure 6.26: The polarisation state as a function of frequency for a magnetised ferrite sheet ($n_f = 5.21$, $\ell = 1.57$ mm).

- [4] C. E. Brown and J. C. Wiltse, *Principles and Applications of Millimeter-Wave Radar*. Editors: N. C. Currie and C. E. Brown, Artech House, p. 11, 1987, chapter 1.
- [5] E. K. Reedy, *Principles and Applications of Millimeter-Wave Radar*. Editors: N. C. Currie and C. E. Brown, Artech House, p. 39, 1987, chapter 2.
- [6] C. H. Currie and N. C. Currie, *Principles and Applications of Millimeter-Wave Radar*. Editors: N. C. Currie and C. E. Brown, Artech House, p. 784, 1987, chapter 17.
- [7] N. C. Currie, S. W. Parker and R. B. Efurud, "MMW System Tradeoffs," *IEEE National Radar Conference*, p. 1, 1988.
- [8] J. B. Horton, "Selected Technology Summaries for Microwave Theory and Techniques—1988," *IEEE Microwave Theory Tech.*, vol. 37, no. 6, pp. 1048–1050, 1989.
- [9] G. F. Dionne, J. A. Weiss, G. A. Allen and W. D. Fitzgerald, "Quasi-Optical Ferrite Rotator for Millimeter Waves," *IEEE Microwave Theory Tech. Conference, Symposium Digest*, pp. 127–130, 1988.

- [10] J. C. Wiltse, "Trends in Millimeter-Wave Applications," *Southcon '83*, Electronics Show and Convention, p.4, 1983.
- [11] J. C. G. Lesurf *Millimetre-wave Optics, Devices & Systems*. Adam Hilger, p. 237, 1990.
- [12] J. R. Birch, J. D. Dromey and J. C. G. Lesurf, "The Optical Constants of Some Low-loss Polymers Between 4 and 40 cm^{-1} ," *Infrared Physics*, vol. 21 pp. 225–228, 1981.
- [13] **PHILIPS** *Permanent Magnets, 1989 : Supplement to Data Handbook C16*. pp. 16–17.
- [14] R. Wylde, *Ph.D. Thesis, Chapter 4*. Queen Mary College, 1985.
- [15] J. R. Birch and J. C. G. Lesurf, "The Near Millimetre Wavelength Optical Constants of Fluorosint," *Infrared Physics*, vol. 27, no. 6 pp. 423–424, 1987.
- [16] J. R. Birch and M. R. Webb, *Data to be published*.
- [17] G. M. Smith and J. C. G. Lesurf, "A Highly Sensitive Millimeter Wave Quasi-Optical FM Noise Measurement System," *IEEE Trans. Microwave Theory Tech.*, vol. 39, pp. 2229–2236, 1991.
- [18] R. E. Collin *Foundations for Microwave Engineering*. McGraw-Hill, pp. 286–299, 1966.
- [19] S. Ramo, J. R. Whinnery and T. van Duzer, *Fields and Waves in Communication Electronics*. John Wiley and Sons, Inc., 1965, pp. 122–124.
- [20] M. Abramowitz and I. A. Stegun, *Handbook of Mathematical Functions*. Ninth Printing of the Dover Edition (first published in 1965), Dover Publications Inc., New York, 1965.
- [21] J. D. Kraus, *Electromagnetics*. Third Edition, McGraw-Hill Book Company, 1984.
- [22] E. C. Jordan and K. G. Balmain, *Electromagnetic Waves and Radiating Systems*. Second Edition, Prentice-Hall Inc., 1968, pp. 123–129.
- [23] A. R. Harvey, *PhD Thesis*. University of St. Andrews, 1990.

Chapter 7

SLM Pattern Evaluation

The first section of this chapter evaluates one specific SLM configuration both theoretically and experimentally. The theoretical techniques that have been applied could be used for more general configurations either in an analytical manner as is done here, or numerically. The second section experimentally evaluates a number of other SLM configurations. Both the theoretical and the experimental techniques developed within this thesis are seen here to be valuable tools in the analysis of the important generic spatial signal processing device, the MMW QO SLM.

7.1 An SLM Pattern Model and Measurement

The specific SLM being modelled here is the simple case of an SLM with a single $\lambda/4$ step as depicted in figure 4.3(b). This is one of the SLM2 stepped mirrors described in section 4.1.2. The origin of the coordinate system of the model developed here is at the centre of the SLM with the x -axis being horizontal, the y -axis being vertical and the z -axis being along the axis of propagation. As the SLM is operating in reflection mode, the $\lambda/4$ step imposes a π radian phase change upon exactly half of the beam. With the sharp discontinuity, it is expected that an infinite number of modes will be produced at the SLM plane.¹ With the SLM in this form, the modelling problem is effectively reduced to a one-dimensional problem.

¹There are really two mirror planes at the SLM, but for the pupose of modelling the SLM function, the SLM is viewed as existing in only one of the mirror planes.

7.1.1 Gaussian Beam-Mode Model

Recall from section 3.2.2 that if Ψ_r represents the beam reflected from the SLM and if ψ_m represents the individual Gaussian beam-modes, then Ψ_r can be written as

$$\Psi_r = \sum_m A_m \psi_m \quad m = 0, 1, 2, 3, \dots \quad (7.1)$$

where only one dimension is being considered, and A_m are the mode coefficients. Also, it was shown that these mode coefficients can be found by evaluating the following expression

$$A_m = \langle \Psi_r | \psi_m \rangle \quad (7.2)$$

For the specific SLM being modelled here, Ψ_r can be written directly in the form

$$\Psi_r = \begin{cases} \psi_o & x > 0 \\ -\psi_o & x < 0 \end{cases} \quad (7.3)$$

This anti-symmetric SLM is unable to produce even modes. A simple graphical analysis of the cross-correlation integral in equation 7.2 shows that there is no net result for the integral for ψ_m when m is even. In addition, the anti-symmetry means that the two half-planes make equal contributions to the integral, and thus equation 7.2 can be written as

$$A_m = 2 \int_0^\infty \psi_o \psi_m^* dx \quad m = 1, 3, 5, \dots \quad (7.4)$$

Recall the form of ψ_o and ψ_m from equations 3.21 and 3.28 and note from section 4.3 that the SLM has been positioned in a beam waist plane and thus we can use the following characteristics of this plane in the analysis, viz.

$$\hat{z} = 0 \quad (7.5)$$

and

$$R \rightarrow \infty \quad (7.6)$$

Thus, substituting the above into equation 7.4 yields

$$A_m = 2 \sqrt{\frac{2}{\pi}} \frac{1}{\omega} \frac{1}{\sqrt{2^m m!}} \int_0^\infty \mathcal{H}_m \left(\frac{\sqrt{2} x}{\omega} \right) e^{-\frac{2x^2}{\omega^2}} dx \quad (7.7)$$

Make the following substitutions

$$\begin{aligned} t &= \frac{\sqrt{2} x}{\omega} \\ \Rightarrow dx &= \frac{\omega}{\sqrt{2}} dt \end{aligned} \quad (7.8)$$

m	1	3	5	7	9
A_m	0.798	-0.326	0.219	-0.169	0.139
A_m^2	0.637	0.106	0.0477	0.0284	0.0193

Table 7.1: The first five mode coefficients.

and

$$m = 2p + 1 \quad p = 0, 1, 2, 3, \dots \quad (7.9)$$

Equation 7.7 thus becomes

$$A_{2p+1} = \frac{2}{\sqrt{\pi}} \frac{1}{\sqrt{2^{2p+1}(2p+1)!}} \int_0^\infty \mathcal{H}_{2p+1}(t) e^{-t^2} dt \quad (7.10)$$

With reference to a book of integrals[1, §2.20.3(4)] a solution for a generalised form of this integral can be found. In this particular case it reduces to the following result

$$\int_0^\infty \mathcal{H}_{2p+1}(t) e^{-t^2} dt = (-1)^p 2^{2p} \left(\frac{1}{2}\right)_p \quad (7.11)$$

where

$$(a)_p = a(a+1)(a+2)\dots(a+p-1) \quad p > 0 \quad (7.12)$$

and

$$(a)_0 = 1 \quad (7.13)$$

Therefore the mode coefficients can be evaluated with the following formula

$$A_m = A_{2p+1} = \frac{(-1)^p 2^{2p+1} \left(\frac{1}{2}\right)_p}{\sqrt{\pi} 2^{2p+1} (2p+1)!} \quad (7.14)$$

Table 7.1 lists the first five coefficients in this series. Recall from section 3.2.3 that the number of modes to include in the expansion for Ψ , where Ψ is that part of Ψ_r that is able to pass essentially unaffected and unimpeded through the aperture, is related to the Fresnel number N for the optics. Now

$$\begin{aligned} a &= 44 \text{ mm} \\ \lambda &= 3.33 \text{ mm} \\ f &= 319 \text{ mm} \end{aligned}$$

and thus

$$N = 0.91 \quad (7.15)$$

Fox and Li[2, figure 15], show that the power losses for the first three modes are approximately 0.14%, 2.2% and 15%. The power loss for the third-order mode is likely to be between 30% and 60%. The next mode of interest is the fifth-order mode and the power loss for this mode is likely to be so great that it's inclusion in the expansion will make no significant difference. This is especially so considering that the power in this mode is less than 5% anyway, (i.e. $|A_5|^2 = 0.0477$). Therefore a reasonable approximation would be to include only the first and third-order modes, and in the first instance to neglect the actual truncation losses at the aperture. Thus Ψ can be written as

$$\Psi = A_1\psi_1 + A_3\psi_3 \quad (7.16)$$

Let the far-field form of Ψ be represented by Ψ_f , and note that for Ψ_f , $\hat{z} \rightarrow \infty$ and $R \rightarrow \infty$. The far-field pattern Ψ_f produced by the optical circuit described in section 4.3 is an *image* of Ψ_r at the SLM plane. This image has been formed through a double Fourier process (i.e. via the lens and via radiation into the far-field). Recall from section 3.3 that this means that Ψ_f has the same form² as Ψ_r in the SLM plane, excepting for aperture effects. If equation 7.16 is written out fully, then this equivalence is readily seen. Taking these features into account, Ψ_f can be written as follows

$$\Psi_f(x) = \sqrt{\frac{2}{\pi}} \frac{1}{\sqrt{\omega}} e^{-\frac{x^2}{\omega^2}} \left[A_1 \frac{\sqrt{2}x}{\omega} + A_3 \frac{1}{48} \left(8 \left(\frac{\sqrt{2}x}{\omega} \right)^3 - 12 \left(\frac{\sqrt{2}x}{\omega} \right) \right) \right] \quad (7.17)$$

Note that $\Psi_f(x, y)$, for $y = 0$, is as follows

$$\Psi_f(x, 0) = \frac{2}{\pi\omega} e^{-\frac{x^2}{\omega^2}} \left[A_1 \frac{\sqrt{2}x}{\omega} + A_3 \frac{1}{48} \left(8 \left(\frac{\sqrt{2}x}{\omega} \right)^3 - 12 \left(\frac{\sqrt{2}x}{\omega} \right) \right) \right] \quad (7.18)$$

It is desirable to express Ψ_f as a function of an angle θ . Recall that for $\hat{z} \rightarrow \infty$

$$\omega = \omega_o \sqrt{1 + \hat{z}^2} \quad (7.19)$$

$$\approx \omega_o \hat{z} \quad (7.20)$$

and so substituting for \hat{z} ,

$$\omega = \frac{2z}{k\omega_o} \quad (7.21)$$

which means that in the far-field there is a constant divergence angle, (i.e. an asymptote). If θ_o marks the $1/e$ level in a beam-mode in the far-field, then

$$\omega = z \tan \theta_o \quad (7.22)$$

²In fact Ψ_f is reversed in sign but otherwise has the same form.

or

$$\theta_o = \tan^{-1} \frac{\omega}{z} \quad (7.23)$$

$$= \tan^{-1} \left(\frac{2}{k\omega_o} \right) \quad (7.24)$$

and for *any* point in the xz plane at a distance z ,

$$x = z \tan \theta \quad (7.25)$$

Thus the factor (x/ω) can be written as

$$\left(\frac{x}{\omega} \right) = \frac{k\omega_o \tan \theta}{2} \quad (7.26)$$

Substituting for (x/ω) and using the analytic forms for A_1 and A_3 , Ψ_f can be written as follows

$$\Psi_f(\theta) = e^{-\left(\frac{k\omega_o \tan \theta}{2}\right)^2} \left[\frac{k\omega_o \tan \theta}{\sqrt{\pi}} - \frac{1}{\sqrt{3\pi}} \left(\frac{1}{6} \left(\frac{k\omega_o \tan \theta}{\sqrt{2}} \right)^3 - \frac{1}{4} \left(\frac{k\omega_o \tan \theta}{\sqrt{2}} \right) \right) \right] \quad (7.27)$$

where the $2/(\pi\omega)$ factor has been dropped because it is independent of θ . This analytic formula has been coded into FORTRAN and this code appears in appendix E. Figure 7.1 shows a scaled graph of Ψ_f as a function of the angle θ , (a scale factor of 2 was used). Note that this pattern is a one-dimensional pattern-cut in the xz plane, and that the parameter ω_o is the focussed beam waist in the Fourier transform plane of the lens—see the circuit in figure 4.13. At this point in the circuit the beam waist should be that of the feedhorns, which is 4.4 mm.

7.1.2 Comparison with Measurement

The radiation patterns measured were intensity patterns, and are shown along with the model results in figure 7.2. (Note the use of a decibel scale.) The polarisation of the beam incident upon the SLM was vertical and co-linear with the length of the $\lambda/4$ step. The radiation pattern was measured in the horizontal plane, that is, in the H-plane. A model incorporating only the first-order mode, and a model incorporating the first, third and fifth-order modes were developed and their results are also shown. The dashed curve is for the model that incorporates only the first and third-order modes. A beam waist of 4.4 mm has been used. Compare this graph with that of figure 7.3, where a beam waist of 5.0 mm has been used. Agreement between the model result and the measurement pattern is better for the larger beam waist. A number

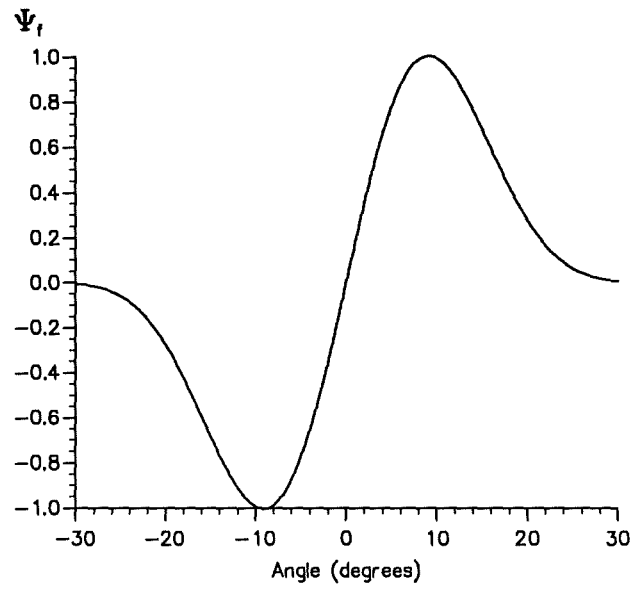


Figure 7.1: The resultant field pattern Ψ_f in the far-field, where only the coefficients A_1 and A_3 have been used. A beamwaist of 4.4 mm was used for this pattern.

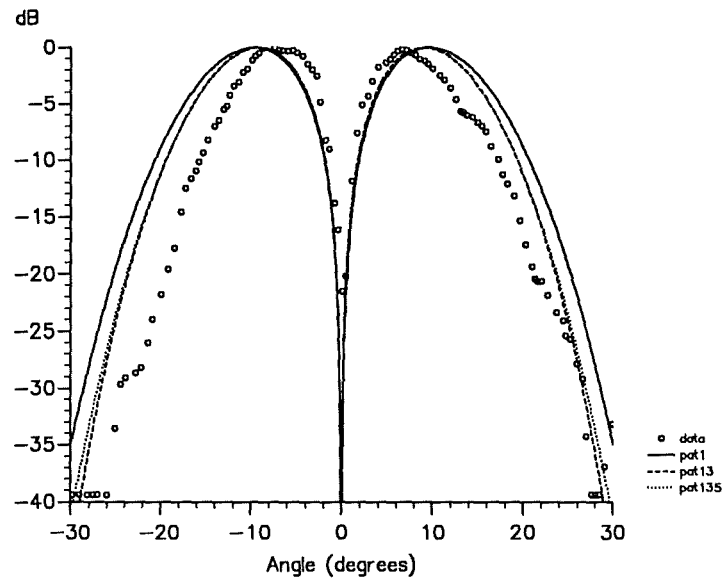


Figure 7.2: The measured and modelled radiation patterns (H-plane). A beam waist of 4.4 mm was used for this pattern.

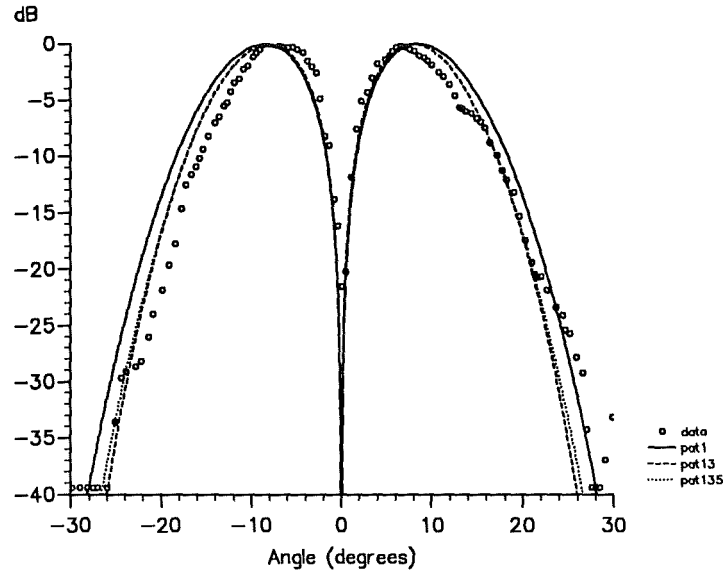


Figure 7.3: The measured and modelled radiation patterns (H-plane). A beam waist of 5.0 mm was used for this pattern.

of possibilities have been considered regarding the discrepancy between the model and the measurement results. The possibilities that have been considered are:

1. An insufficient number of modes has been used.
2. The pattern has not been measured sufficiently “far” in the far-field.
3. The lens position in the optics is incorrect.
4. The beam waist sizes for the higher order modes are different to those expected because the lens was designed for fundamental modes, (i.e. Φ_m was neglected in the lens design).
5. There was an error in the original value used for ω_o for the feed horn.
6. The lens design is somewhat in error, (i.e. it has an insufficiently strong focussing action).
7. The position of the beam waist is not over the pivot point.

The first four possibilities can be readily eliminated. (1)The effect of including the fifth-order mode has negligible impact on the pattern form. (2)If θ_o is calculated for

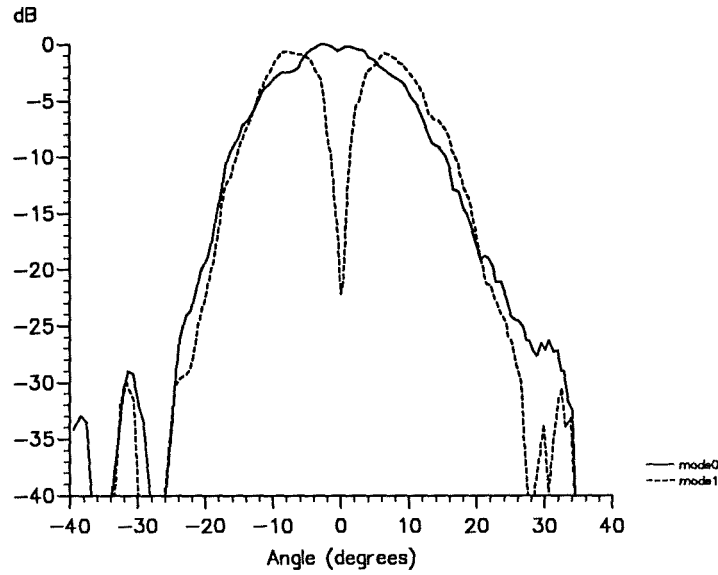


Figure 7.4: The SLM modulated beam with the unmodulated fundamental mode beam.

$\hat{z} \rightarrow \infty$ and for $\hat{z} \approx 16$, then the angles are 13.43° and 13.45° respectively, and so insufficient to account for the observed difference. (3) If the lens were positioned at a position other than at $\hat{z} = 1$, then the beam's radius of curvature incident upon the lens would be less than the maximum, and the focussing action of the lens would be correspondingly stronger. That is, the resultant far-field pattern would be still further spread out, which in fact is the opposite of what is being looked for. (4) Appendix B has shown that the effect of excluding Φ_m in the lens design is of negligible significance for this particular optical circuit. These next two considerations provide something of a puzzle. (5) Figure 4.16 shows the radiation pattern of the feed horn. The $1/e^2$ power levels (i.e. the -8.68 dB level) give a beam widths of $+14.7^\circ$ and -13.7° which is about 6% greater than expected for a beam waist of 4.4 mm—see (2) above. (6) Figure 7.4 shows the measured radiation pattern of the of the beam radiated from the circuit when there is a plane mirror in the SLM plane, together with the modulated beam. The beam widths of the fundamental mode beam in this case are $+13.7^\circ$ and -15.8° which is about 10% greater than expected for a beam waist of 4.4 mm. From these last two considerations, the beam waist at the aperture would seem, if anything, to be a little smaller than 4.4 mm. The final consideration (7) may offer some explanation. If the lens is focussing the beam to a beam waist at a position closer to the lens than the pivot point, then the measured pattern will appear to be slightly narrower than

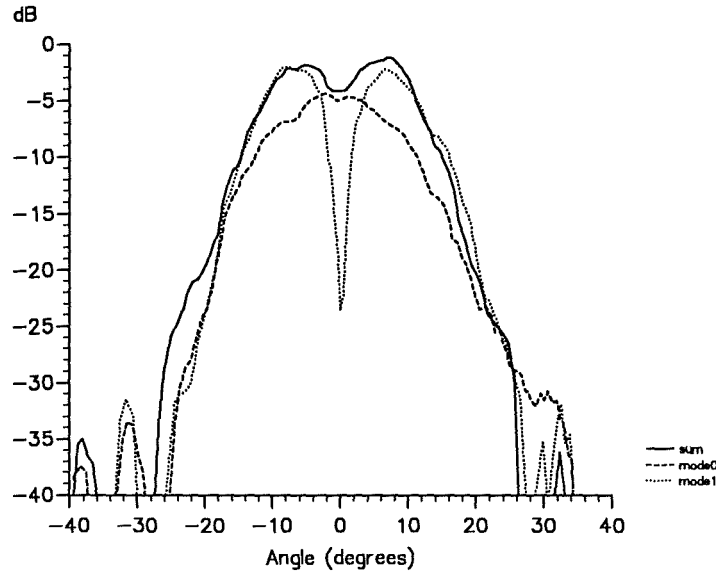


Figure 7.5: The two beams and their sum as used for the phase pattern measurement.

it in fact should. However section 4.3.1.2 shows that this effect is probably too small to adequately account for the actual measured pattern. Nevertheless, the model has shown substantial agreement with measurements and it would therefore be worth some effort to attempt to account for the small discrepancy in future models.

Note that the patterns shown in figure 7.4 are on the same scale, from which it is seen that the SLM modulated pattern is about 0.6 dB down on the fundamental mode beam. This shows that there is no significant loss mechanism other than mode truncation at the lens aperture.

The anti-phase nature of the pattern, as shown in figure 7.1, has been demonstrated to exist within the experiment also. The MMW QO circuit schematically shown in figure 4.13 was modified so that separate and orthogonal beams were launched out of the exit lens. One beam was the beam modulated by the SLM as normal, and the other beam was produced by removing the first Faraday rotator and allowing half of the beam incident upon the 45° polariser to be reflected towards a roof mirror (i.e. replacing the matched load). Thus, this second beam was an unmodulated beam, (i.e. a fundamental mode beam). Figure 7.5 shows separate measurements of the two beams and their summed resultant. The pyroelectric detector measures power, (i.e. not field) and was aligned so that for the two orthogonal polarisations, the detector had approximately equal responsivities. The phase of the fundamental mode beam was

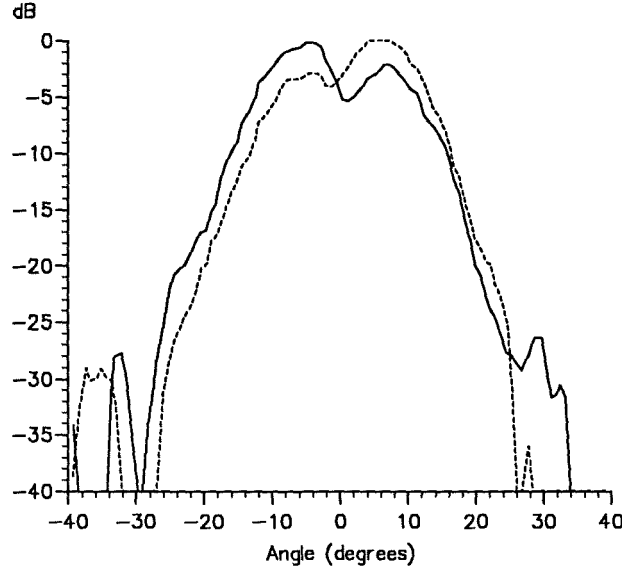


Figure 7.6: The summed patterns with a phase difference for the fundamental mode beam from one pattern to the other being a half-wavelength.

stepped at 0.2 mm (or $\lambda/16$) intervals for over more than a half-wavelength. Figure 7.6 shows two radiation patterns. The phase difference for the fundamental mode beam from one pattern to the other was $\lambda/2$. These two patterns represent two limiting cases. Figure 7.7 shows these two patterns together with the in-between stepped patterns. As the phase of the fundamental mode beam was stepped, the two lobes were observed to move in opposite directions. This indicates that one lobe was becoming progressively more in-phase with the fundamental mode beam, while at the same time the other lobe was becoming progressively more out-of-phase with the fundamental mode beam. This is just the sort of behaviour that would be expected if the two lobes were in anti-phase. This set of patterns demonstrates that the pattern lobes are indeed, in anti-phase. This technique could be used in a more refined, quantitative sense to generate actual phase patterns, should that ever be desirable.

7.2 Other SLM Configurations

A number of other SLM configurations have been experimentally investigated. There are some interesting features of the patterns produced by these SLM configurations that should be noted. Three categories of patterns are presented here and they include:

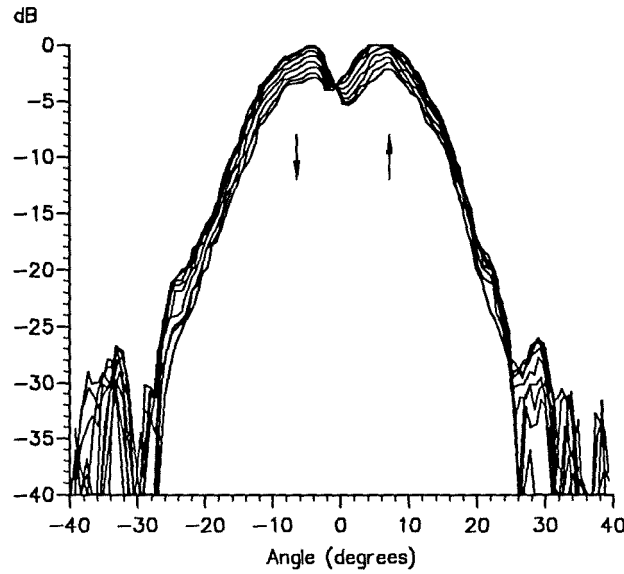


Figure 7.7: The series of stepped patterns.

patterns in other planes for the same SLM configuration modelled in the previous section; patterns from higher-order SLM configurations; and the pattern from an SLM with a half-wavelength step.

7.2.1 An SLM with a Single $\lambda/4$ Step

The E-plane pattern of the SLM with a single $\lambda/4$ step modelled in the previous section, and with the incident polarisation orthogonal to the line of the $\lambda/4$ step, is shown in figure 7.8. As expected for an axially symmetric incident beam, this pattern is essentially identical to the H-plane pattern shown in the previous section, where there the polarisation was co-linear with the length of the step. Note also that the E-plane pattern for this SLM configuration with the polarisation co-linear with the step was also measured, and a null pattern was recorded. More precisely, the pattern had a maximum approximately 20 dB below the unmodulated beam's maximum.

7.2.2 Higher Order SLM Configurations

The step in the SLM configurations used here are all $\lambda/4$ steps, (i.e. they result in the imposition of π radian spatial phase shifts). The first of these is the SLM2(c)—see figure 4.3—which seems to largely produce the second-order mode pattern (an even

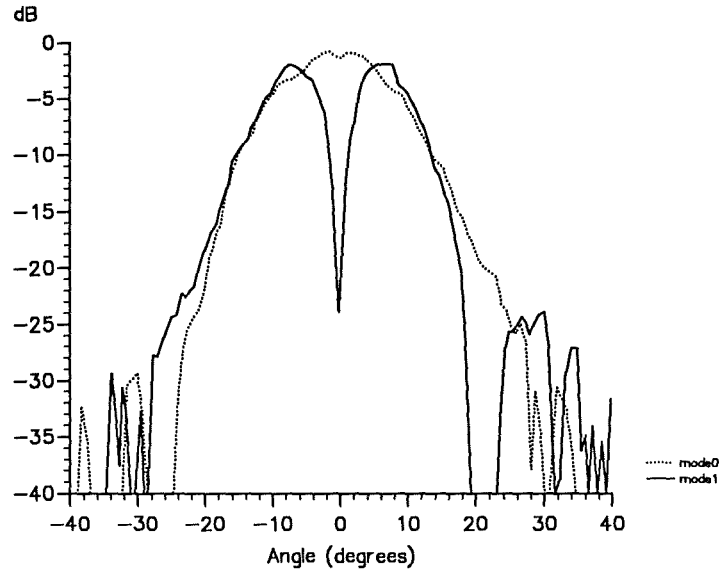


Figure 7.8: E-plane pattern with incident polarisation orthogonal to the length of the $\lambda/4$ step.

pattern) as shown in figure 7.9. The two nulls are clearly evident, though not as deep as for the the previous SLM configuration. The centre lobe has slightly less height compared to the outer two lobes which is what would be expected for the second-order Gaussian-Hermite function. It is likely that the finite aperture size is mostly responsible for the observed null filling.

Figure 7.10 shows the pattern for the SLM2(d) configuration. It seems to produce a significant amount of the third-order mode. The centre null is particularly deep at approximately the -25 dB level. However the outer lobes are lower rather than higher compared to the two inner lobes, as would have been expected from the third-order Gaussian-Hermite function. Possibly this pattern is revealing the effects of some truncation of this third-order mode.

The SLM1 was set into a quasi-mode11 configuration, that is, with offset $\lambda/4$ steps running in both the x and the y directions. This configuration would be expected to produce four lobes with nulls along both axes. Figure 7.11 shows the H-plane pattern for this configuration as effectively a null pattern. Also, there was some evidence found for the existence of four lobes. The SLM was tilted ($\approx 3.5^\circ$) out of being perpendicular to the beam's axis, and so the reflected beam was also tilted. This enabled a qualitative inspection to be made of the radiation pattern out of the principal planes. The resultant

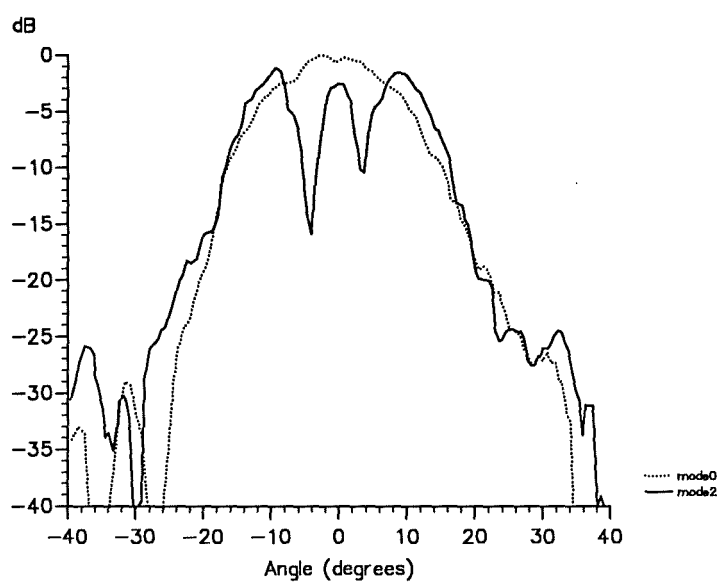


Figure 7.9: The H-plane radiation pattern produced with the SLM2(c).

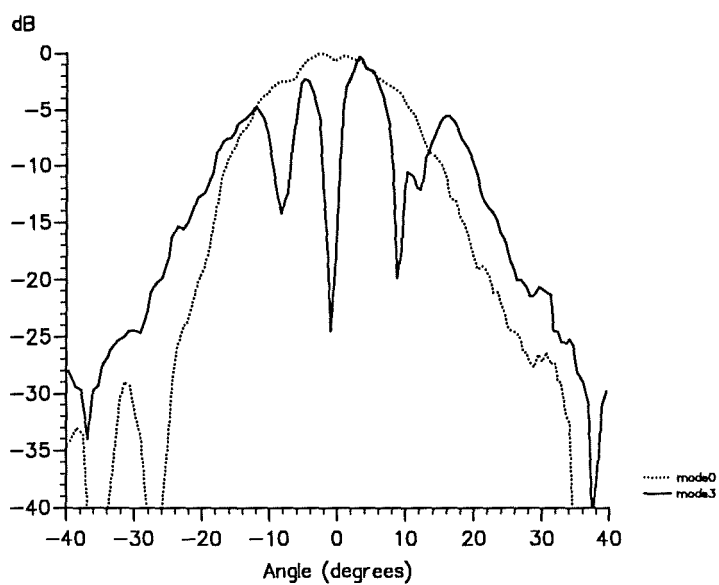


Figure 7.10: The H-plane radiation pattern produced with the SLM2(d).

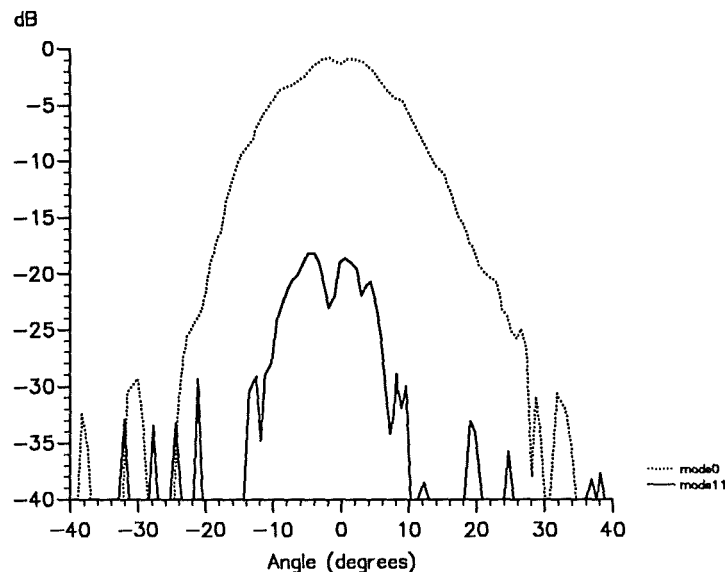


Figure 7.11: The H-plane radiation pattern produced with the SLM1 in the quasi-model11 configuration.

pattern shown in figure 7.12 indeed shows two separate lobes. There were also two lobes observed with the SLM tilted the other way, and thus four lobes in total were observed, as expected.

7.2.3 An SLM with a Single $\lambda/2$ Step

The SLM1 was set up to have a single step running the full height of the SLM, and with a depth of $\lambda/2$. Thus the phase imposition would be expected to be 2π radians. For such a configuration, no change in the beam's pattern would be expected. Figure 7.13 shows both the original unmodulated and the phase-modulated beam's radiation patterns. The patterns are nearly identical, as expected.

The results presented within this section all tend to indicate that the behaviour of the MMW QO SLM can be intuitively determined with a reasonable degree of confidence. The idea of treating the stepped portions of the SLM as sources of spatial phase impositions, is seen to be essentially valid. The previous section has already shown quantitatively that this is so, but these patterns give some grounds for generalising the idea.

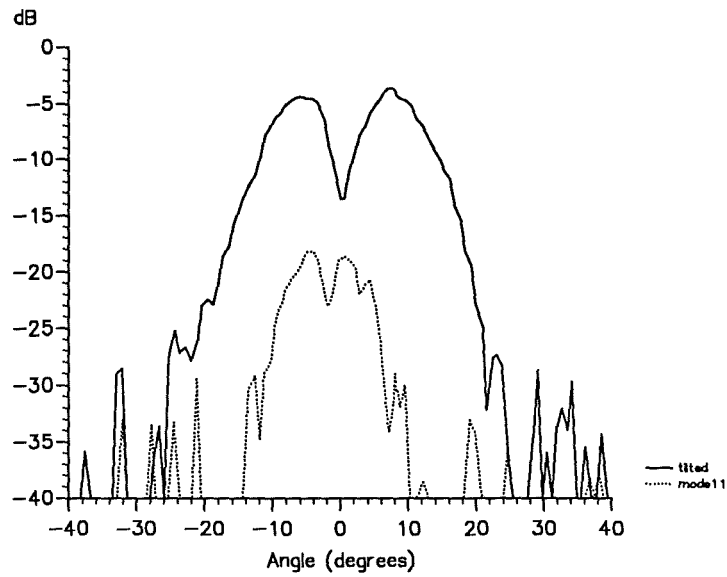


Figure 7.12: Evidence for the existence of four lobes present out of the principal planes.

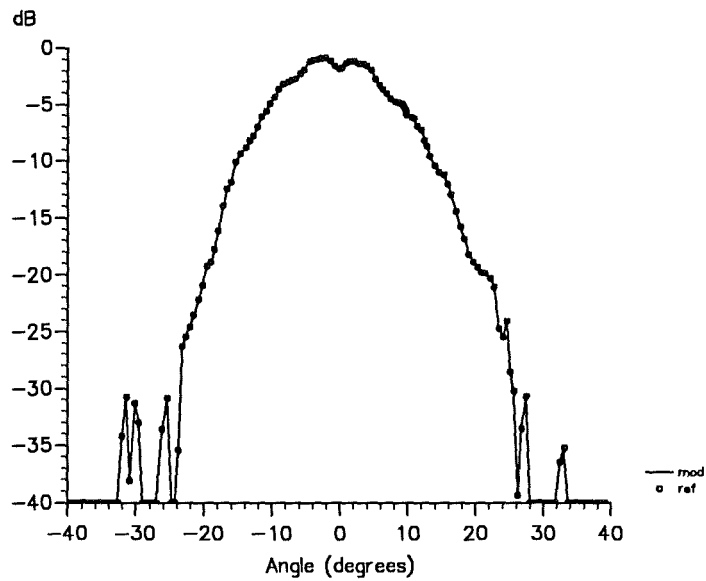


Figure 7.13: The radiation pattern of the SLM with a single $\lambda/2$ step.

References

- [1] A. P. Prudnikov, Yu. A. Brychkov and O. I. Marichev, *Integrals and Series—Volume 2: Special Functions*. Gordon and Breach Science Publishers, 1986.,
- [2] A. G. Fox and T. Li, “Resonant Modes in a Maser Interferometer,” *The Bell System Technical Journal*, pp. 453–488, March 1961.

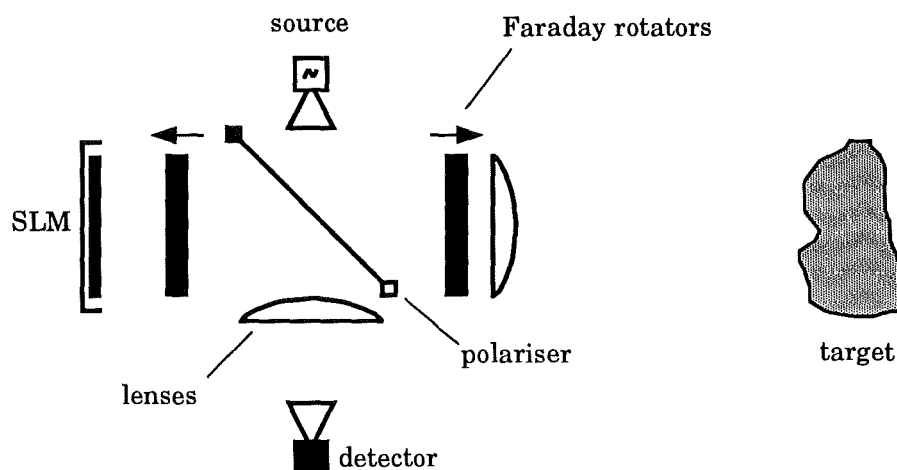
Epilogue

Signal Processing

The next stage for this work should probably begin with an experimental program to evaluate the potential for modal analysis using MMW QO SLMs. One possible simple approach to this is shown in the figure over the page. The SLM is used in conjunction with the detector feed horn and lens to filter specific modes (or mode sets), from a reflected beam of arbitrary mode content. The detector feed horn and lens constitute a fundamental mode filter. Following this, the application of spatial filter theory to MMW radar should be investigated. Partial coherence theory will be significant, for it will provide a means for dealing with atmospheric corruption of the spatial coherence of a beam used in a radar.

Beams

Another possibility worth some investigation, is the suitability or otherwise of MMW QO SLMs for beam-forming and beam-shaping. Adaptive control of these processes would also be of interest. Multiple beams applications could also be investigated. One specific application could involve enhancing car radar to include a low-cost beam scanning/switching facility as this would enable a certain degree of Look-left and Look-right, which may well have some advantage. In time, when detection itself becomes less costly, multiple beams could be processed in parallel with a minimum of hardware (i.e. both optics and electronics).



Devices

The Faraday rotator work could move on to look at incorporating multiple layer matching structures that would increase their bandwidth. In addition, a systematic evaluation of ferrite materials could well provide some new possibilities including for instance, the exploitation of some of the non-linear properties of ferrites.

The pyroelectric detector work could be taken further in at least two respects. Firstly, an order of magnitude increase in sensitivity is still likely to be achievable. Secondly, the development of a focal plane array could be undertaken. Such a low-cost device would undoubtedly be useful for example, in the development and evaluation of complex SLM filter functions.

In many ways this new area of research and development has barely got off the ground. The door has been opened, but that is all.

Appendix A

RADPAT : A Radiation Pattern Measurement Program

Program Listing

```
REM    >:meas_pat.radpat.radpat.txt
REM
REM    RADPAT is a BASIC data capture program that
REM    monitors the angular position of the radiation
REM    pattern measurement facility's receiver, and
REM    records both the angle and signal level in an
REM    interactively determined manner.
REM
REM    Written by Michael R. Webb, during October 1991,
REM    and modified during December 1991 and January 1992.
REM    Based on codes previously developed by Mike Leeson
REM    and Andy Harvey.
REM
REM    9/1/92
REM
REM    PROGRAM DESCRIPTION
REM
REM    The main array for the measured data is: pattern(3,1,400).
REM    This allows a record of 4 scans, the 2 pattern variables
REM    (angle and signal), and 400 points per scan.
REM
REM
REM
REM
REM    Main program begins here:
REM
DIM pattern(3,1,400)
quit$="false"
PROCinitialise
REPEAT
PROCmenu
UNTIL quit$="true"
```

```

PROCquit
END
REM   Main program ends here.
:
:
DEF PROCinitialise
MODE 12                      :REM (80 X 32) text
@%=&01000505                 :REM PRINT format statement
VDU 23 1 0 0 0 0 0 0 0 0    :REM cursor off
PROCtext_window("top")      :REM defines text window
VDU 24, 0;0;1279;832;        :REM defines graphics window
GCOL 4+128                   :REM background colour to blue
COLOUR 4+128                 :REM also blue background for text
CLS : CLG
TIME=0
delay=3                      :REM delay for adc routine, in centi-seconds.
COLOUR 9,2
COLOUR 11,4
COLOUR 13,6
red%=1 : magenta%=5
white%=7 : black%=0
blue%=4 : yellow%=3
green%=9 : cyan%=13 : REM Uses COLOUR reassignments above.
this_scan%=0
old_av%=100
t_ang=-90 : t_pwr=-40
sense$=""
PROCadc_read
A%=1                        :REM adc module number
angle_ch%=2 : B%=2          :REM channel for angle voltage
signal_ch%=3                :REM channel for signal voltage
no_avs%=100 : C%=100        :REM number of reads
PRINT "Check connections to adc module number ONE :" : PRINT
PRINT "channel for angle voltage      2"
PRINT "channel for detector voltage   3" : PRINT
INPUT "Modify ?"
x$=GET$ : CLS
IF ((x$="Y") OR (x$="y")) THEN PROCset_adc : x$="n"
PRINT TAB(0,0)"Calibrate ?" ;
x$=GET$ : CLS
IF ((x$="Y") OR (x$="y")) THEN
PROCcalibrate
ELSE
PRINT "Stored calibration data being used."
PROCcaldata
finish=TIME+100
REPEAT UNTIL TIME>finish
ENDIF
REM The following define the positions for the angle and signal
REM variables in the pattern array.
ANG%=0 : SIG%=1
REM The following presets the range and resolution variables.
angres=0.5
angstep=INT(10*angres)
ang_range=40 : x_factor%=9 : x_scale%=20
title$="untitled"
address$=":meas_pat"

```

```

PROCbox
ENDPROC
:
:
DEF PROCText_window(where$)
CASE where$ OF
  WHEN "top" : VDU 28,0,5,79,0
  WHEN "trim" : VDU 28,0,25,10,15
ENDCASE
ENDPROC
:
:
DEF PROCadcread
REM This procedure was written entirely by Andy Harvey, and contains
REM some code that is not actually used within this program.
FRED%=&03000000 :REM base address of FRED in slot
ROM_address%=&33C0000 :REM base address of podule ROM in slot 0
int_status_address%=&3000 :REM IRQ and FIQ status bits within ROM
bus_VIA%=FRED%
podule_VIA%=&33C2000
REM ***** assign VIA register addresses *****
port_B%=0
port_A%=4*&01 :REM port A
B_dir%=4*&02 :REM port B dirn. reg.
A_dir%=4*&03 :REM port A dirn. reg.
timer2_low%=4*8
timer2_high%=4*9
ACR%=4*&0B :REM Aux Control Reg
PCR%=4*&0C :REM Peripheral Control Reg
IntFR%=4*&0D :REM interrupt Flag Register
Inter%=4*&0E :REM Interrupt Enable Register
counter_base%=4*&20
DAC%=4*&30
ADC_base%=4*&40
Pcol=7:Lcol=7:Rcol=7:Bcol=7:Ccol=7:gain=-1
array_size%=600
DIM result%(array_size%)
resultH%=0:resultL%=0
status%=0
DIM program% &1000 :REM Unsure of required size here.
FOR opt%=8 TO 10 STEP 2 :REM range check, then range check and report errors
P%=program%
L%=P% + &1000
REM The following that is enclosed within '[ .. ]' is assembly code.
[
  OPT opt%
  .start_adc :entry;R0=ADC No.,R1=channel number,R11=FRED%
  \ensure select_flag is set to >7 after crate power up
  STMFD R13!,{R2-R4,R11,R14} \exit;nothing
  ADD R11,R11,#ADC_base% \modification '\'' 12-04-91
  ADD R11,R11,R0, ASL #3 \ADC addresses are at increments of 8
  ADR R3,select_flag \get selected channel
  LDR R4,[R3] \and
  CMP R4,R1 \if different from new one
  STRNEB R1,[R11,#4] \write channel No. to ADC
  STRNE R1,[R3] \store new channel
  STRB R1,[R11] \start conversion

```

```

LDMFD R13!,{R2-R4,R11,R14}
MOVS PC,R14
.select_flag                                \\flag for channel number
EQU 0 &FF
\
.read_adc                                  \entry;R0=adcNo;R11=FRED%
STMFD R13!,{R1,R2,R11,R14}                \exit;R0=conversion
ADD R11,R11,#ADC_base%
ADD R11,R11,R0, ASL #3
.read_adc_status
LDRB R0,[R11,#4]                           \read status bit - only bit 0 is valid
TST R0,#1                                   \status bit goes low when conversion complete
BNE read_adc_status
LDRB R0,[R11]                               \get hi byte
LDRB R1,[R11]                               \get lo byte
STRB R0,[R11]                               \start_adc
ADD R0,R1,R0, ASL #8                        \
TST R0,#&8000                               \is it -ve
ORRNE R0,R0,#&FF0000
ORRNE R0,R0,#&FF000000                      \if so convert to 32 bit 2's complement int.
RSB R0,R0,#0                                \make answer -ve because adc input is inverted
\ now check to see if these are the biggest or smallest readings so far
\ ADR R1,min_adc
\ LDR R2,[R1]                               \get previous min value
\ CMP R0,R2
\ STRLT R0,[R1]                             \replace it if new one is smaller
\ LDR R2,[R1,#4]                             \get previous max value
\ CMP R0,R2
\ STRGT R0,[R1,#4]                           \replace it if new one is larger
LDMFD R13!,{R1,R2,R11,R14}
MOVS PC,R14
.min_adc
EQU 0                                       \address for min reading
.max_adc
EQU 0                                       \address for max reading
\
\selects channel, starts and reads the adc from USR mode R2 times and returns
\the sum of R2 reads in R0
\ a min and max value are updated at each adc_read
.read_adc_USR                             \entry;R0=adc No.,R1=channel No.,R2=number
STMFD R13!,{R2-R12}                       \exit;R0=32 bit 2's compliment result
MOV R11,#FRED%                             \enter SVC mode so can talk to FRED
MOV R3,#0                                   \zero accumulator register
MOV R4,R0                                   \save channel number
SWI "OS_EnterOS"
BL start_adc
.read_adc_USR_loop
MOV R0,R4                                  \get channel number back for read_adc
SWI "OS_IntOff"
\ BL start_adc
BL read_adc
SWI "OS_IntOn"
ADD R3,R3,R0
SUBS R2,R2,#1                              \decrement no of samples counter
BGT read_adc_USR_loop                     \if not finished then loop
MOV R0,R3                                  \stick accumulated result in R3
TEQP PC,#0                                \return to user mode

```

```

MOVNV R0,R0
LDMFD R13!,{R2-R12}
MOVVS PC,R14                                \return from subroutine
]
NEXT opt%
ENDPROC
:
:
DEF PROCset_adc
INPUT "adc module number?"                "A%"
INPUT "angle voltage channel?"            "angle_ch% : B%=angle_ch%"
INPUT "detector voltage channel?"        "signal_ch% : CLS"
ENDPROC
:
:
DEF PROCcalibrate
REPEAT
ok$="true"
PRINT "Check all connections."
PRINT "Move the arm to a calibration position and then press SPACEBAR"
REPEAT UNTIL GET=32
calpos1%=FNtalk_adc(delay) : CLS
PRINT "By convention, beam centre is zero degrees." : PRINT
INPUT "Enter calibration angle, <return> for default: "calang1 : CLS
IF (calang1=0) THEN
IF (calpos1%<500) THEN
calang1=-81.53
ELSE
calang1=81.53
ENDIF
ENDIF
PRINT "Move the arm to another calibration position and then press SPACEBAR"
REPEAT UNTIL GET=32
calpos2%=FNtalk_adc(delay) : CLS
INPUT "Enter calibration angle, <return> for default: "calang2 : CLS
IF (calang2=0) THEN
IF (calpos2%<500) THEN
calang2=-81.53
ELSE
calang2=81.53
ENDIF
ENDIF
PRINT "Move the arm directly to a third calibration position"
PRINT "and then press SPACEBAR"
REPEAT UNTIL GET=32
calpos3%=FNtalk_adc(delay) : CLS
PRINT "Move the arm well past it's current position, and then"
PRINT "move it back again to precisely the same position."
PRINT "When this is done, press SPACEBAR"
REPEAT UNTIL GET=32
calpos4%=FNtalk_adc(delay) : CLS
hyst%=calpos4%-calpos3%
calpos2%=calpos2%-hyst%
IF calpos1%<>calpos2% THEN
g = (calang2 - calang1)/(calpos2% - calpos1%)
ELSE
PRINT "Something is wrong. The angle voltage didn't change! - re-calibrate."

```

```

finish=TIME+200
REPEAT UNTIL TIME>finish
CLS
ok$="false"
ENDIF
IF ok$="true" THEN
  IF g<>0 THEN
    c = calang2 -(g*calpos2%)
  ELSE
    PRINT "Identical calibration angles were mistakenly given - re-calibrate."
    ok$="false"
    finish=TIME+150
    REPEAT UNTIL TIME>finish
    CLS
  ENDIF
ENDIF
UNTIL ok$="true"
IF calpos2%<calpos1% THEN
  cal_sense$="cw"
ELSE
  cal_sense$="ccw"
ENDIF
X=OPENOUT("cal_data")
PRINT#X,calpos1%,calpos2%,hyst%,calang1,calang2,g,c,cal_sense$
CLOSE#X
ENDPROC

:
:
DEF PROCcaldata
X=OPENIN(":meas_pat.radpat.cal_data")
INPUT#X,calpos1%,calpos2%,hyst%,calang1,calang2,g,c,cal_sense$
CLOSE#X
ENDPROC

:
:
DEF Fntalk_adc(delay)
REM The delay here is to allow the adc channel switching, time to
REM settle down before reading begins at the new channel. Ideally
REM this should be taken care of within the assembly language
REM routine, and thus be transparent to the user of this routine.
REM This however is a workable fix.
adc_val=USR(read_adc_USR) : REM The result from this first read is
:                          : REM ignored. It switches channel if B%
:                          : REM has changed since last called.
wait$=INKEY$(delay) : REM Delay mechanism provides 'delay' centi-seconds.
adc_val=(USR(read_adc_USR))/C%
=adc_val
:
:
DEF PROCbox
GCOL 7      : REM white
CLG
MOVE 190,80
DRAW 190,800
DRAW 1270,800
DRAW 1270,80
DRAW 190,80

```

```

FOR i%=-2 TO 2
MOVE FNscreenx(x_scale%i%),80
DRAW FNscreenx(x_scale%i%),800
NEXT i%
FOR i%=1 TO 4
MOVE 190,FNscreeny(-10*i%)
DRAW 1270,FNscreeny(-10*i%)
NEXT i%
VDU 5
FOR i%=-3 TO 3
MOVE (FNscreenx(x_scale%i%)-70),60
PRINT x_scale%i%
NEXT i%
MOVE 700,30 : PRINT"Angle"
FOR i%=0 TO 4
MOVE 90,(FNscreeny(-10*i%)+16)
PRINT -10*i%
NEXT i%
MOVE 70,816 :PRINT"dB"
VDU 4
ENDPROC
:
:
DEF FNscreenx(a)
=INT(730 + x_factor%*a)
:
:
DEF FNscreeny(a)
=INT(800 + 18*a)
:
:
DEF PROCmenu
CLS
PRINT TAB(0,0) "(L)oad (O)utput (P)rint (C)lear (D)irectory"
PRINT TAB(0,2) "(S)can (R)ange & Resolution (A)verages (Q)uit"
VDU 5
@%=&01000405
GCOL 0,7
MOVE 0,700 : PRINT"Averages"
GCOL 0,4
MOVE 0,650 : PRINTold_av%
GCOL 0,7
MOVE 0,650 : PRINTno_avs%
@%=&01000505
VDU 4
centre%=44 - 0.5*LEN(title$)
PRINT TAB(centre%,5);title$;
PROCtext_window("trim")
PRINT TAB(0,0)"Angle";
PRINT TAB(0,5)"dB";
PROCtext_window("top")
ans$=""
REPEAT
PROCtrim
ans$=INKEY$(20)
UNTIL ans$<>""
IF ans$="S" OR ans$="s" THEN PROCscan

```



```

IF ans$="L" OR ans$="l" THEN PROCtake
IF ans$="O" OR ans$="o" THEN PROCgive
IF ans$="P" OR ans$="p" THEN PROCprint_graph
IF ans$="C" OR ans$="c" THEN PROCflush
IF ans$="Q" OR ans$="q" THEN quit$="true"
IF ans$="R" OR ans$="r" THEN PROClimits
IF ans$="A" OR ans$="a" THEN PROCaverage
IF ans$="D" OR ans$="d" THEN PROCdefault
ENDPROC
:
:
DEF PROCscan
PRINT TAB(0,4)"Scan";
count%=0
old_ang=ang_range
REM Determine direction of scanning arm.
dira%=FNtalk_adc(delay)
IF ((this_scan% MOD 2)=0) THEN
  GCOL red%
  COLOUR red%
ELSE
  GCOL yellow%
  COLOUR yellow%
ENDIF
REM Look for start angle.
ang=FNangle(FNtalk_adc(delay))
IF (ABS(ang)>ang_range) THEN
  esc$=""
  REPEAT
    ang=FNangle(FNtalk_adc(delay))
    PROCtrim
    esc$=INKEY$(20)
  UNTIL ((ABS(ang)<=ang_range) OR esc$<>"")
  IF (esc$="") THEN
    dirb%=FNtalk_adc(delay) : REM Direction of scanning arm set here.
    IF dirb%<dira% THEN
      sense$="cw"
    ELSE
      sense$="ccw"
    ENDIF
    title$="modified"
    hyst_rmv$=""
    SOUND 1,-15,118,7
    REM Read in desired pattern data.
    REPEAT
      IF cal_sense$=sense$ THEN
        REPEAT
          ang=FNangle((FNtalk_adc(delay))-hyst%)
          PROCtrim
          UNTIL (ABS(ang-old_ang)>angres)
        ELSE
          REPEAT
            ang=FNangle(FNtalk_adc(delay))
            PROCtrim
            UNTIL (ABS(ang-old_ang)>angres)
          ENDIF
        IF cal_sense$=sense$ THEN

```

```

    ang=FNangle((FNtalk_adc(delay))-hyst%)
    B%=signal_ch%
    signal=FNpower(FNtalk_adc(delay))
    B%=angle_ch%
ELSE
    ang=FNangle(FNtalk_adc(delay))
    B%=signal_ch%
    signal=FNpower(FNtalk_adc(delay))
    B%=angle_ch%
ENDIF
old_ang=ang : count%=count%+1
IF count%=1 THEN
    MOVE FNscreenx(ang),FNscreeny(signal)
ELSE
    DRAW FNscreenx(ang),FNscreeny(signal)
ENDIF
REM Store pattern points in array.
pattern(this_scan%,ANG%,count%)=ang
pattern(this_scan%,SIG%,count%)=signal
UNTIL ((ABS(ang)>=(ang_range+2)) OR (count%>400))
pattern(this_scan%,ANG%,0)=count%
pattern(this_scan%,SIG%,0)=no_avs%
SOUND 1,-15,100,7
GCOL white%
COLOUR white%
IF this_scan%<>3 THEN
    this_scan%=this_scan%+1
    PRINT TAB(0,4)"    ";
ELSE
    this_scan%=0 : CLS
    PRINT "Do you wish to output these patterns to disc?"
    x$=GET$
    IF ((x$="Y") OR (x$="y")) THEN
        PROCgive
    ELSE
        CLS
        PRINT "Warning : Further scans will cause loss of data."
        finish=TIME+200
        REPEAT UNTIL TIME>finish
    ENDIF
ENDIF
sense$=""
ELSE
    GCOL white%
    COLOUR white%
ENDIF
ELSE
    CLS
    PRINT "ERROR : The detector is already within the scan range."
    PRINT "      Move detector arm or change range."
    finish=TIME+200
    REPEAT UNTIL TIME>finish
    GCOL white% : COLOUR white%
ENDIF
ENDPROC
:
:
```

```

DEF PROCtrim
@%=&01020104
PROCtext_window("trim")
VDU 23 1 0 0 0 0 0 0 0 0 :REM cursor off
REM This procedure is at present somewhat unsatisfactory in that
REM it incorporates the hysteresis calibration factor only during
REM scanning, ie. not during the menu idling. This ought to be
REM corrected.
IF sense$=cal_sense$ THEN
  t_ang=FNangle((FNtalk_adc(delay))-hyst%)
  B%=signal_ch%
  t_pwr=FNpower(FNtalk_adc(delay))
  B%=angle_ch%
ELSE
  t_ang=FNangle(FNtalk_adc(delay))
  B%=signal_ch%
  t_pwr=FNpower(FNtalk_adc(delay))
  B%=angle_ch%
ENDIF
PRINT TAB(0,2)t_ang;" ";
PRINT TAB(0,7)t_pwr;" ";
@%=&01000505
PROCtext_window("top")
ENDPROC
:
:
DEF FNangle(x)
=x*g +c
:
:
DEF FNpower(u)
IF u<=0.4096 THEN TP=-40 ELSE TP=10*LOG(u/4096)
=TP
:
:
DEF PROCtake
REPEAT
  ok$="no"
  INPUT TAB(0,4)"filename ";name$
  IF ASC(name$)=-1 THEN ENDPROC
  old_av%=no_avs%
  PRINT TAB(0,4)"
  file$=address$+"."+name$
  SYS "OS_File",5,file$ TO found% :REM Checks for valid filename.
  IF found%=1 THEN ok$="yes"
UNTIL ok$="yes"
X=OPENIN file$
INPUT#X,title$
INPUT#X,x_f%,x_s%
IF ((x_f%<>x_factor%) OR (x_s%<>x_scale%)) THEN
  x_scale%=x_s% : x_factor%=x_f%
PROCbox
ENDIF
FOR scan_no%=0 TO 3
  INPUT#X,no_points%,avs%
  pattern(scan_no%,ANG%,0)=no_points% : pattern(scan_no%,SIG%,0)=avs%
  IF no_points%<>0 THEN

```

```

    FOR t%=1 TO no_points%
        INPUT#X,pattern(scan_no%,0,t%),pattern(scan_no%,1,t%)
    NEXT t%
ENDIF
NEXT scan_no%
CLOSE#X
no_avs%=pattern(0,SIG%,0)
PROCdraw : REM Draw the stored patterns.
ENDPROC
:
:
DEF PROCdraw
    FOR scan_no%=0 TO 3
        IF ((scan_no% MOD 2)=0) THEN
            GCOL red%
        ELSE
            GCOL yellow%
        ENDIF
        no_points%=pattern(scan_no%,0,0)
        MOVE FNscreenx(pattern(scan_no%,0,1)),FNscreeny(pattern(scan_no%,1,1))
        FOR t%=2 TO no_points%
            DRAW FNscreenx(pattern(scan_no%,0,t%)),FNscreeny(pattern(scan_no%,1,t%))
        NEXT t%
    NEXT scan_no%
    GCOL white%
ENDPROC
:
:
DEF PROCgive
    CLS
    VDU 23 1 1 0 0 0 0 0 0 0 :REM cursor on
    both$="no"
    PRINT "(a)scii or (d)ata or (b)oth ?"
    x$=GET$ : CLS
    IF ((x$="a") OR (x$="A")) THEN PROCascii
    IF ((x$="b") OR (x$="B")) THEN both$="yes"
    IF both$="no" THEN
        IF ((x$<>"d") AND (x$<>"D")) THEN ENDPROC
    ENDIF
    REPEAT
        ok$="no"
        CLS
        PRINT TAB(0,0)"data file"
        INPUT TAB(0,4)"filename ";name$
        IF ASC(name$)=-1 THEN ENDPROC
        PRINT TAB(0,4)"
        INPUT TAB(0,4)"Title ";title$
        CLS : centre%=44 - 0.5*LEN(title$)
        PRINT TAB(centre%,5);title$;
        file$=address$+"."+name$
        dir_name$=name$
        REPEAT
            L%=LEN(dir_name$)
            ch$=MID$(dir_name$,L%,1)
            dir_name$=LEFT$(dir_name$)
        UNTIL (ch$=".") OR (L%<1)
        IF L%<1 THEN

```

```

chk_name$=address$
ELSE
  chk_name$=address$+"."+dir_name$
ENDIF
SYS "OS_File",5,chk_name$ TO found%
IF found%=2 THEN ok$="yes"
IF ((L%<1) AND (LEN(name$)>10)) OR ((LEN(name$)-L%)>10) THEN
  COLOUR magenta%+128
  COLOUR green%
  CLS
  title$=""
  PRINT TAB(3,3) "INVALID FILENAME"
  finish=TIME+100
  REPEAT UNTIL TIME>finish
  COLOUR blue%+128
  COLOUR white%
  ENDPROC
ENDIF
UNTIL ok$="yes" :REM Valid directory path
X=OPENOUT file$
PRINT#X,title$
PRINT#X,x_factor%,x_scale%
FOR scan_no%=0 TO 3
  PRINT#X,pattern(scan_no%,ANG%,0),pattern(scan_no%,SIG%,0)
  no_points%=pattern(scan_no%,0,0)
  IF no_points%<>0 THEN
    FOR t%=1 TO no_points%
      PRINT#X,pattern(scan_no%,0,t%),pattern(scan_no%,1,t%)
    NEXT t%
  ENDIF
NEXT scan_no%
CLOSE#X
IF both$="yes" THEN PROCascii
VDU 23 1 0 0 0 0 0 0 0 :REM cursor off
ENDPROC
:
:
DEF PROCascii
REPEAT
  ok$="no"
  CLS
  PRINT TAB(0,0)"ascii file"
  INPUT TAB(0,4)"filename ";name$
  IF ASC(name$)=-1 THEN ENDPROC
  PRINT TAB(0,4)"
  IF both$="no" THEN
    INPUT TAB(0,4)"Title ";title$
    CLS : centre%=44 - 0.5*LEN(title$)
    PRINT TAB(centre%,5);title$;
  ENDIF
  file$=address$+"."+name$
  dir_name$=name$
  REPEAT
    L%=LEN(dir_name$)
    ch$=MID$(dir_name$,L%,1)
    dir_name$=LEFT$(dir_name$)
  UNTIL (ch$=".") OR (L%<1)

```

```

IF (L%<1) THEN
  chk_name$=address$
ELSE
  chk_name$=address$+"."+dir_name$
ENDIF
SYS "OS_File",5,chk_name$ TO found%
IF found%=2 THEN ok$="yes"
IF ((L%<1) AND (LEN(name$)>10)) OR ((LEN(name$)-L%)>10) THEN
  COLOUR magenta%+128
  COLOUR green%
  CLS
  title$=""
  PRINT TAB(3,3) "INVALID FILENAME"
  finish=TIME+100
  REPEAT UNTIL TIME>finish
  COLOUR blue%+128
  COLOUR white%
  ENDPROC
ENDIF
UNTIL ok$="yes"
X=OPENOUT file$
BPUT#X,title$
BPUT#X,STR$(x_factor%);
BPUT#X," ";
BPUT#X,STR$(x_scale%)
FOR scan_no%=0 TO 3
  BPUT#X,STR$(pattern(scan_no%,0,0));
  BPUT#X," ";
  BPUT#X,STR$(pattern(scan_no%,1,0))
  no_points%=pattern(scan_no%,0,0)
  IF no_points%<>0 THEN
    FOR t%=1 TO no_points%
      BPUT#X,STR$(pattern(scan_no%,0,t%));
      BPUT#X," ";
      BPUT#X,STR$(pattern(scan_no%,1,t%))
    NEXT t%
  ENDIF
NEXT scan_no%
CLOSE#X
OSCLI("settype "+address$+"."+name$+" Text")
ENDPROC
:
:
DEF PROCprint_graph
CLS
PRINT TAB(32,3)TIME$
centre%=44 - 0.5*LEN(title$)
PRINT TAB(centre%,5);title$;
VDU 26
*qprint
PROCtext_window("top")      :REM re-defines text window
VDU 24, 0;0;1279;832;       :REM re-defines graphics window
ENDPROC
:
:
DEF PROCflush
PRINT TAB(0,4)"Clear";

```

```

pattern()=0
PRINT TAB(0,4)"      ";
title$="untitled"
old_av%=100 : no_avs%=100 : C%=100
this_scan%=0 : hyst_rmv$=""
PROCbox
ENDPROC
:
:
:
DEF PROClimits
CLS
PRINT "Changing these parameters will mean losing current data."
PRINT : PRINT "Are you sure ?"
chk$=GET$
IF ((chk$="Y") OR (chk$="y")) THEN
VDU 23 1 1 0 0 0 0 0 0 :REM cursor on
REPEAT
ok$="true"
CLS
INPUT "Angular resolution [0.5 deg min]      "angres
IF angres<0.5 THEN
ok$="false"
ELSE
angstep = INT(10*angres)
ENDIF
IF ok$="true" THEN
PRINT
PRINT "Enter the required maximum angular"
INPUT "deviation from beam centre:          "ang_range
IF ABS(ang_range)>85 THEN
ok$="false"
ELSE
ang_range = ABS(ang_range)
title$="untitled"
x_factor%=6 : x_scale%=30
IF ang_range<=60 THEN x_factor%=9 : x_scale%=20
IF ang_range<=30 THEN x_factor%=18 : x_scale%=10
CLS
ENDIF
ENDIF
UNTIL ok$="true"
VDU 23 1 0 0 0 0 0 0 0 :REM cursor off
PROCbox
PROCflush
ENDIF
ENDPROC
:
:
DEF PROCcoverage
IF this_scan%=0 THEN
old_av%=no_avs%
INPUT TAB(0,4)"Number of Averages = "no_avs%
IF no_avs% <1 THEN no_avs%=1
IF no_avs% >1000 THEN no_avs%=1000
C%=no_avs% : REM C% is passed to the adc_read code.
ELSE

```

```
CLS
PRINT "The number of averages can only be altered "
PRINT "at the start of a new set of four patterns."
finish=TIME+150
REPEAT UNTIL TIME>finish
CLS
ENDIF
ENDPROC
:
:
DEF PROCdefault
REPEAT
  ok$="no"
  INPUT TAB(0,4)"Default directory address ? "address$
  IF (ASC(address$)<>-1) THEN
    SYS "OS_File",5,address$ TO found%
    IF found%=2 THEN ok$="yes"
  ELSE
    address$=":meas_pat"
    ok$="yes"
  ENDIF
UNTIL ok$="yes"
ENDPROC
:
:
DEF PROCquit
VDU 26
CLS:CLG
MODE 128
VDU 23 1 1 0 0 0 0 0 0 0 :REM cursor on
ENDPROC
```


Appendix B

Multi-mode Propagation Through a Lens

In order to understand the significance of the higher order mode anomolous phase terms, consider figure B.1. Following Harvey's analysis[10, section 3.5.1], the key phase-matching equation is

$$r^2 = \frac{2}{k \left(\frac{n_r}{R_d} + \frac{1}{R'} \right)} ((n_r - 1)kz_L + \epsilon) \quad (\text{B.1})$$

where ϵ is the sum of the anomolous phase terms, that is

$$\begin{aligned} \epsilon = \tan^{-1} \left(\frac{2(n_r z + t - z_L)}{n_r k \omega_o^2} \right) + \tan^{-1} \left(\frac{2(z' - t + z_L)}{k \omega_o'^2} \right) - \\ \tan^{-1} \left(\frac{2(n_r z + t)}{n_r k \omega_o^2} \right) - \tan^{-1} \left(\frac{2(z' - t)}{k \omega_o'^2} \right) \end{aligned} \quad (\text{B.2})$$

and where k is the free space propagation constant and $z_L(r)$ is the lens profile, that is

$$k = \frac{2\pi}{\lambda} \quad (\text{B.3})$$

$$z_L = z_L(r) \quad (\text{B.4})$$

R_d is the input beam's radius of curvature within the lens dielectric and over the thickness of the lens, and R' is the output beam's radius of curvature in free space over the thickness of the lens. Thus R_d and R' are functions of position and so

$$R_d = R_d(n_r z + t - z_L) \quad (\text{B.5})$$

$$R' = R'(z' + z_L) \quad (\text{B.6})$$

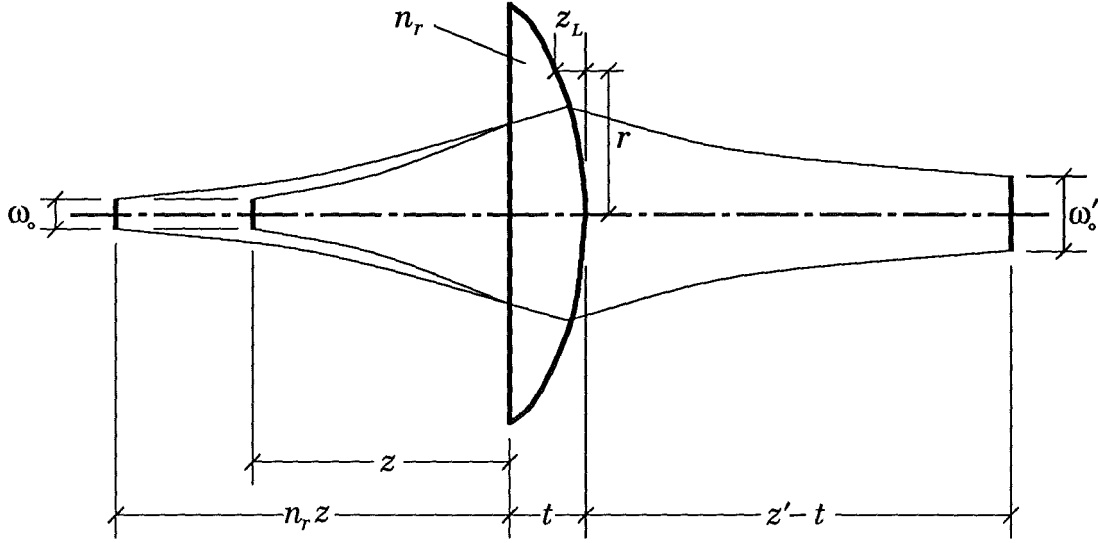


Figure B.1: A schematic diagram of a quasi-optical lens with the relevant design parameters shown.

Within this development it will be assumed that the lens is *thin*, and thus R_d and R' are considered to be essentially constant. This assumption breaks down for lenses close to the beam waist (i.e. $\hat{z}_0 \sim 1$). The following table lists some of the parameters relevant to this specific situation:

λ	=	3.32 mm
n_r	=	1.43
ω_0	=	4.4 mm
ω_a	=	26 mm
ω'_0	=	18.4 mm
z	=	106 mm
z'	=	297 mm
t	=	22 mm
R_a	=	110 mm
R_d	=	$n_r R_a$
R'	=	638 mm

For a beam of order (m, n) , *epsilon* in equation B.1 must be prefixed with the factor $(m + n + 1)$. The significance of the $(m + n + 1)\epsilon$ term can be assessed by

comparing it's magnitude with the main phase term in equation B.1, $(n_r - 1)kz_L$. Table B.1 summarises the magnitude of these phase terms for a number of higher order modes. This comparison is performed for one representative phase path, namely the path that passes through the lens at $r = \omega_a = 26$ mm. For this path, $z_L = 8.4$ mm. Thus for higher order modes up to say $\Psi_{mn} = \Psi_{55}$ or in one dimension only, Ψ_{101} , the contribution that the anomolous phase terms make is $< 1\%$. In order to develop a useful relationship between an error in the phase matching process and the resultant output radius of curvature, equation B.1 can be re-written with the effect of the ϵ term incorporated as a correction factor to the main phase term. Also, for this specific case, the fundamental mode ϵ term is considered negligible. Thus

$$r^2 = \frac{2}{\left(\frac{n_r}{R_d} + \frac{1}{R'}\right)}(1 + \zeta)(n_r - 1)z_L \quad (\text{B.7})$$

and with the thin lens asumption, $z_L(r)$ is essentially parabolic, and so

$$\frac{z_L}{r^2} = 12.4 \text{ mm}^{-1}$$

It is seen that within figure 4.13, it is the focussing of the multi-mode beam to the effective source aperture over the pivot point that is of interest here. Thus our input/output nomenclature as used in this present discussion, is reversed. Thus it is the dependence of R_a upon ζ that must be determined. Re-writing equation B.7 gives

$$\frac{1}{R_a} = 10.7\zeta + 9.1 \text{ mm}^{-1} \quad (\text{B.8})$$

For $\hat{z}_0 \sim 6$, equation 3.25 shows that $R(z) \simeq z$, and so the dependence of the output beam waist position upon the higher order mode content of the beam can be similarly described. Thus

$$\frac{1}{z} \simeq 10.7\zeta + 9.1 \text{ mm}^{-1} \quad (\text{B.9})$$

and so if δ represents the relative change in z for a given anomolous phase term correction factor ζ , then δ is given by

$$\begin{aligned} \delta &= \frac{z(\zeta) - z(0)}{z(0)} \\ &= \frac{1.2\zeta}{1.2\zeta + 1} \end{aligned} \quad (\text{B.10})$$

Recall that the central purpose of this exercise is to obtain an estimate of how significant a corruption, a multi-mode beam suffers, by passing through a lens designed

Anomalous Phase Term Significance						
(m, n)	$(0, 0)$	$(1, 1)$	$(2, 2)$	$(3, 3)$	$(4, 4)$	$(5, 5)$
$(m + n + 1)\epsilon$	$.310^\circ$	$.931^\circ$	1.55°	2.17°	2.79°	3.41°
2π	360°					
% of 2π	.086%	.26%	.43%	.60%	.78%	.95%

Table B.1: The significance of the anomalous phase term for one specific path through the beam, viz. $\omega_a = 26$ mm and $z_L = 8.4$ mm.

for fundamental mode propagation only. If the various higher order mode components of the beam have different output beam waist positions then the effective source aperture will in reality be a three-dimensional aperture. Blurring of the radiation pattern detail can be expected if δ is of significant magnitude. Now δ corresponds to the δ in equation 4.15, which shows that for a δ of say 1% (i.e. $\zeta \sim 0.8\%$), the effect on the radiation pattern will be less than a 0.1 dB variation.

Therefore it is seen that the effect of the lens on a multi-mode beam for this specific set-up is of negligible significance. If however a more compact system was required, with lenses smaller and closer to beam waists, then the effects described here would become increasingly significant.

Appendix C

FE1 : Modelling the Reflectance of a Ferrite Sheet

Program Listing

```
*      A program to evaluate the reflection coefficient for a
*      ferrite sheet, as a function of frequency. It includes
*      ferrite losses. The polarisation is assumed to be
*      uniform throughout.
*
*      STANDARD FORTRAN 77
*
*      M. R. Webb
*      November 11, 1991
*
*      PROGRAM FE1
*      ..Parameters..
*      INTEGER KEYBRD,SCREEN
*      PARAMETER (KEYBRD=5,SCREEN=6)
*      DOUBLE PRECISION Z0
*      PARAMETER (Z0=376.731)
*      CHARACTER TITLE*(*)
*      PARAMETER (TITLE='Reflectance for a Thin Ferrite Sheet')
*      ..Local Scalars..
*      INTEGER I,J,N
*      DOUBLE PRECISION FSTART,FSTOP,FSTEP,XIN,YIN,
+          RINDEX,ATTEN,FREQ,LENGTH,REFL
*      CHARACTER AGAIN,TQUERY
*      ..External Subroutines..
*      EXTERNAL FSPAN,SETUPG,TABLE,INPUT,OPTHDR,OUTPUT,ZIN
*      ..Various UNIRAS routines are called within this program..
*
*      ..Executable Statements..or..Main Program..
*
*      WRITE(SCREEN,FMT=999) TITLE
*      CALL FSPAN(FSTART,FSTOP,FSTEP,KEYBRD,SCREEN)
*      N=IDINT((FSTOP-FSTART)/FSTEP)
```

```

      CALL SETUPG(FSTART,FSTOP,KEYBRD,SCREEN)
      CALL TABLE(TQUERY,OPFILE,KEYBRD,SCREEN)
*    ..The following loop simulates a REPEAT UNTIL loop..
      AGAIN='N'
      I=0
10    CONTINUE
      I=I+1
      CALL INPUT(RINDEX,ATTEN,LENGTH,KEYBRD,SCREEN)
      CALL OPTHDR(TQUERY,OPFILE,RINDEX,ATTEN,I,LENGTH,TITLE)
      FREQ=FSTART
      DO 20 J=1,N+1
        CALL ZIN(FREQ,RINDEX,ATTEN,LENGTH,ZO,XIN,YIN)
*      REFL=DSQRT(((XIN-ZO)**2+YIN**2)/((XIN+ZO)**2+YIN**2))
      REFL=((XIN-ZO)**2+YIN**2)/((XIN+ZO)**2+YIN**2)
      CALL OUTPUT(FREQ,REFL,TQUERY,OPFILE,FSTART)
      FREQ=FREQ+FSTEP
20    CONTINUE
*    ..The next set of statements are the UNTIL conditions..
      IF (I.NE.99) THEN
        WRITE(SCREEN,FMT=998)
        READ(KEYBRD,FMT=*) AGAIN
      ENDIF
*    ..The next statement is the conditional UNTIL jump..
      IF ((AGAIN.EQ.'Y').OR.(AGAIN.EQ.'y')) GOTO 10
*    ..UNIRAS calls to close graphics output..
      CALL GEMPTY
      CALL GCLOSE
      STOP
999  FORMAT(/A)
998  FORMAT(/'Again? ')
      END
*
*    ..Subroutines..
*
      SUBROUTINE FSPAN(FSTART,FSTOP,FSTEP,KEYBRD,SCREEN)
*    ..Local Scalars..
      DOUBLE PRECISION FSTART,FSTOP,FSTEP
*    ..Executable Statements..
      FSTART=70.
      FSTOP=120.
      FSTEP=1.
      WRITE(SCREEN,FMT=899)
      READ(KEYBRD,FMT=*,END=1000) FSTART,FSTOP,FSTEP
1000 CONTINUE
      FSTART=FSTART*1D9
      FSTOP=FSTOP*1D9
      FSTEP=FSTEP*1D9
      RETURN
899  FORMAT(/'Enter the start frequency, the stop frequency ',
+        'and the frequency step in GHz : ')
      END
*
      SUBROUTINE SETUPG(FSTART,FSTOP,KEYBRD,SCREEN)
*    ..Parameters..
      REAL UNDEF
      PARAMETER (UNDEF=999.999)
      REAL RFLMIN,RFLMAX

```

```

PARAMETER (RFLMIN=0.,RFLMAX=1.)
*
  ..Local Scalars..
  DOUBLE PRECISION FSTART,FSTOP
  REAL FBEGIN,FEND,XS,YS
  CHARACTER HRDCPY
*
  ..Executable Statements..
  FBEGIN=REAL(FSTART/1D9)
  FEND=REAL(FSTOP/1D9)
  WRITE(SCREEN,FMT=799)
  READ(KEYBRD,FMT=*) HRDCPY
  IF ((HRDCPY.EQ.'Y').OR.(HRDCPY.EQ.'y')) THEN
*
  ..UNIRAS Graphics Commands Following..
  CALL GROUTE('select mpost ; exit')
  ELSE
  CALL GROUTE('select mx11 ; exit')
  ENDIF
  CALL GOPEN
  CALL RORIEN(1)
  CALL GRPSIZ(XS,YS)
  CALL GVPORT(XS*.2,YS*.2,XS*.7,YS*.7)
  CALL GWBOX(XS*.7,YS*.7,0.)
  CALL GLIMIT(FBEGIN,FEND,RFLMIN,RFLMAX,0.,0.)
  CALL GSCALE
  CALL GCLEAR
  CALL RAXTEX(5,-2,'Frequency (GHz)',UNDEF,UNDEF,3.)
  CALL RAXIS(1,RFLMIN,3.,1)
  CALL RAXTEX(5,-2,'Reflectance',UNDEF,UNDEF,3.)
  CALL RAXIS(2,FBEGIN,3.,1)
  CALL GEMPTY
  RETURN
799 FORMAT(/'Do you want a hardcopy graphics output this time? ')
END
*
SUBROUTINE TABLE(TQUERY,OPFILE,KEYBRD,SCREEN)
*
  ..Local Scalars..
  INTEGER OPFILE
  CHARACTER TQUERY
*
  ..Executable Statements..
  WRITE(SCREEN,FMT=699)
  READ(KEYBRD,FMT=*) TQUERY
  IF ((TQUERY.EQ.'Y').OR.(TQUERY.EQ.'y')) THEN
  WRITE(SCREEN,FMT=698)
  READ(KEYBRD,FMT=*) OPFILE
  ELSE
  OPFILE=6
  ENDIF
  RETURN
699 FORMAT('Do you also want a tabled output? ')
698 FORMAT('Enter the FORTRAN file number for this table: ')
END
*
SUBROUTINE INPUT(RINDEX,ATTEN,LENGTH,KEYBRD,SCREEN)
*
  ..Local Scalars..
  DOUBLE PRECISION RINDEX,ATTEN,LENGTH
*
  ..Executable Statements..
  RINDEX=5.345
  ATTEN=903.3

```

```

    LENGTH=1.5
    WRITE(SCREEN,FMT=599)
    READ(KEYBRD,FMT=*,END=1000) RINDEX
    WRITE(SCREEN,FMT=598)
    READ(KEYBRD,FMT=*,END=1000) ATTEN
    WRITE(SCREEN,FMT=597)
    READ(KEYBRD,FMT=*,END=1000) LENGTH
1000 CONTINUE
    ATTEN=ATTEN/8.69
    LENGTH=LENGTH/1D3
    RETURN
599 FORMAT(/'Enter the refractive index for the ferrite sheet : ')
598 FORMAT('Enter the attenuation constant for the ferrite ',
+ ' sheet in dB/m : ')
597 FORMAT('Enter the thickness of the ferrite sheet in mm : ')
    END

*
    SUBROUTINE OPTHDR(TQUERY,OPFILE,RINDEX,ATTEN,TBLNUM,LENGTH,TITLE)
*
    ..Local Scalars..
    CHARACTER TQUERY
    CHARACTER TITLE*(*)
    INTEGER OPFILE,TBLNUM
    DOUBLE PRECISION RINDEX,ATTEN,LENGTH
*
    ..Executable Statements..
    IF ((TQUERY.EQ.'Y').OR.(TQUERY.EQ.'y')) THEN
        WRITE(OPFILE,FMT=499) TITLE,TBLNUM
        WRITE(OPFILE,FMT=498) RINDEX
        WRITE(OPFILE,FMT=497) ATTEN*8.69
        WRITE(OPFILE,FMT=496) LENGTH*1D3
        WRITE(OPFILE,FMT=495)
    ENDIF
    RETURN
499 FORMAT(/A,' : ', I3)
498 FORMAT(/'Refractive Index of Ferrite Sheet : ', F6.3)
497 FORMAT('Attenuation Constant of Ferrite Sheet : ', F6.1,
+ ' dB/m')
496 FORMAT('Thickness of Ferrite Sheet : ', F6.2,' mm')
495 FORMAT(/'Frequency (GHz)', 5X,' Reflectance',/)
    END

*
    SUBROUTINE OUTPUT(FREQ,REFL,TQUERY,OPFILE,FSTART)
*
    ..Local Scalars..
    CHARACTER TQUERY
    INTEGER OPFILE
    DOUBLE PRECISION FREQ,REFL,FSTART
    REAL FBEGIN,FQY,RRFEL
*
    ..Executable Statements..
    FBEGIN=REAL(FSTART/1D9)
    FQY=REAL(FREQ/1D9)
    RRFEL=REAL(REFL)
    IF ((FQY-FBEGIN).LT.1E-4) THEN
*
        .. UNIRAS Subroutines..
        CALL GVECT(FBEGIN,RRFEL,0)
        CALL GEMPTY
    ELSE
        CALL GVECT(FQY,RRFEL,1)
        CALL GEMPTY
    
```



```

ENDIF
IF ((TQUERY.EQ.'Y').OR.(TQUERY.EQ.'y')) THEN
  WRITE(OPFILE,FMT=399) (FREQ/1D9),REFL
ENDIF
RETURN
399 FORMAT(1X,3X, F6.2,5X,5X,F5.4)
END

*
SUBROUTINE ZIN(FREQ,RINDEX,ATTEN,LENGTH,ZO,XIN,YIN)
*
  ..Local Scalars..
  DOUBLE PRECISION FREQ,RINDEX,ATTEN,LENGTH,ZO,XIN,YIN,
+XF,YF,RF,PHIF,RIN,PHIIN,XTANH,YTANH,XNUM,YNUM,XDEN,YDEN,
+RNUM,PHINUM,RDEN,PHIDEN
*
  ..External Subroutines..
  EXTERNAL PARTS
*
  ..Executable Statements..
  CALL PARTS(FREQ,RINDEX,ATTEN,LENGTH,ZO,XF,YF,XTANH,YTANH)
  RF=DSQRT(XF**2+YF**2)
  PHIF=DATAN2(YF,XF)
  XNUM=ZO+XF*XTANH-YF*YTANH
  YNUM=XF*YTANH+YF*XTANH
  XDEN=XF+ZO*XTANH
  YDEN=YF+ZO*YTANH
  RNUM=DSQRT(XNUM**2+YNUM**2)
  PHINUM=DATAN2(YNUM,XNUM)
  RDEN=DSQRT(XDEN**2+YDEN**2)
  PHIDEN=DATAN2(YDEN,XDEN)
  RIN=RF*RNUM/RDEN
  PHIIN=PHIF+PHINUM-PHIDEN
  XIN=RIN*DCOS(PHIIN)
  YIN=RIN*DSIN(PHIIN)
  RETURN
END

*
SUBROUTINE PARTS(FREQ,RINDEX,ATTEN,LENGTH,ZO,
+XF,YF,XTANH,YTANH)
*
  ..Parameters..
  DOUBLE PRECISION PI,EPS0,C
  PARAMETER (PI=3.1415926536,EPS0=8.854185D-12,C=299.7925D+6)
*
  ..Local Scalars..
  DOUBLE PRECISION FREQ,RINDEX,ATTEN,LENGTH,ZO,XF,YF,
+XTANH,YTANH,SIGMA,DELTA,BETA
*
  ..External Subroutines..
  EXTERNAL MYTANH
*
  ..Executable Statements..
  SIGMA=ATTEN*2.*RINDEX/ZO
  XF=ZO/RINDEX
  YF=(ZO/RINDEX)*SIGMA/(4*PI*FREQ*EPS0*(RINDEX**2))
  DELTA=(SIGMA**2)/(32.*(PI**2)*(FREQ**2)*((EPS0*(RINDEX**2))**2))
  BETA=(2.*PI*FREQ*RINDEX/C)*(1+DELTA)
  CALL MYTANH(ATTEN*LENGTH,BETA*LENGTH,XTANH,YTANH)
  RETURN
END

*
SUBROUTINE MYTANH(X,Y,XTANH,YTANH)
*
  ..Local Scalars..
  DOUBLE PRECISION X,Y,XTANH,YTANH,R,PHI

```

```
*      ..Executable Statements..  
      R=DSQRT((DCOSH(2*X)-DCOS(2*Y))/(DCOSH(2*X)+DCOS(2*Y)))  
      PHI=DATAN2(DSIN(2*Y),DSINH(2*X))  
      XTANH=R*DCOS(PHI)  
      YTANH=R*DSIN(PHI)  
      RETURN  
      END  
*
```

Appendix D

FE2 : Modelling the Reflectance of a Polarisation Active Ferrite Sheet

Program Listing

```
*      A program to evaluate the reflectance of a ferrite sheet
*      as a function of frequency. It includes both ferrite
*      losses and the dual-valued polarisation-dependent
*      permeability. The output is in the form of a table to the
*      screen and a file formatted for UNIGRAPH usage, and also
*      includes an indication of the polarisation states of the
*      reflectances.
```

```
*
*      -----
*      | The rationale for the variable notation: |
*      |-----|
*      | Prefix          Variable Name          Polarisation |
*      |-----|
*      | real -- X          eg. REFL              P -- plus   |
*      | imag -- Y          IN                    M -- minus   |
*      | mod --- R          COPOL                  |
*      | phase - P          |
*      |-----|
*      | eg. For the imaginary part of the REFlectivity |
*      | for LHC or negative polarisation, the |
*      | appropriate variable name is : |
*      |-----|
*      | YREFLM |
*      |-----|
*      | etc. |
*      |-----|
```

```
*      STANDARD FORTRAN 77
```

```
*      M. R. Webb
```

```
*      December 10, 1991
```

```

*      Final Revisions - May 13, 1992
*
      PROGRAM FE2
*      ..Parameters..
      INTEGER KEYBRD,SCREEN,CIRC
      PARAMETER (KEYBRD=5,SCREEN=6,CIRC=99)
      DOUBLE PRECISION Z0,PI
      PARAMETER (Z0=376.731,PI=3.1415926536)
      CHARACTER TITLE*(*)
      PARAMETER (TITLE='Reflectance for a Thin Ferrite Sheet')
*      ..Local Scalars..
      INTEGER I,J,N
      DOUBLE PRECISION FSTART,FSTOP,FSTEP,XINP,YINP,XINM,YINM,
+RINDEX,ATTEN,FREQ,LENGTH,CONDUCT,RTMUP,RTMUM,BS,FATTEN,
+RREFLP,RREFLM,PREFLP,PREFLM,XREFLP,YREFLP,XREFLM,YREFLM,
+RRCPOL,RRXPOL,PRCPOL,PRXPOL,RELLIP,RTILT,
+WM,XFP,YFP,XFM,YFM
      CHARACTER AGAIN,TQUERY
      CHARACTER*20 NAME
*      ..External Subroutines..
      EXTERNAL FSPAN,TABLE,INPUT,OPTHDR,OUTPUT,ZIN,POINCR,PROPGN
*
*      ..Executable Statements..or..Main Program..
*
      WRITE(SCREEN,FMT=999) TITLE
      CALL FSPAN(FSTART,FSTOP,FSTEP,KEYBRD,SCREEN)
      N=IDINT((FSTOP-FSTART)/FSTEP)
      OPEN(CIRC,FILE='circ_pol.dat')
*      ..The following loop simulates a REPEAT UNTIL loop..
      AGAIN='N'
      I=0
      OPFILE=0
      NAME='first.table'
10  CONTINUE
      I=I+1
      OPFILE=OPFILE+1
      CALL TABLE(TQUERY,OPFILE,NAME,KEYBRD,SCREEN)
      CALL INPUT(RINDEX,CONDUCT,LENGTH,WM,
+BS,ATTEN,FATTEN,KEYBRD,SCREEN)
      CALL OPTHDR(TQUERY,OPFILE,SCREEN,RINDEX,CONDUCT,LENGTH,
+I,TITLE,BS,ATTEN,FATTEN,CIRC)
      FREQ=FSTART
      DO 20 J=1,N+1
*      ..Calculate Reflectance Characteristics..
      RTMUP=DSQRT(1+(WM/(WM-(2*PI*FREQ))))
      CALL ZIN(FREQ,RINDEX,CONDUCT,LENGTH,RTMUP,Z0,XINP,YINP,XFP,YFP)
      RTMUM=DSQRT(1+(WM/(WM+(2*PI*FREQ))))
      CALL ZIN(FREQ,RINDEX,CONDUCT,LENGTH,RTMUM,Z0,XINM,YINM,XFM,YFM)
      RREFLP=DSQRT(((XINP-Z0)**2+YINP**2)/((XINP+Z0)**2+YINP**2))
      PREFLP=DATAN2(YINP,XINP-Z0)-DATAN2(YINP,XINP+Z0)
      XREFLP=RREFLP*DCOS(PREFLP)
      YREFLP=RREFLP*DSIN(PREFLP)
      RREFLM=DSQRT(((XINM-Z0)**2+YINM**2)/((XINM+Z0)**2+YINM**2))
      PREFLM=DATAN2(YINM,XINM-Z0)-DATAN2(YINM,XINM+Z0)
      XREFLM=RREFLM*DCOS(PREFLM)
      YREFLM=RREFLM*DSIN(PREFLM)
*      ..Circular Polarisation Quantities..

```

```

WRITE(CIRC,*) FREQ/1D9,RREFLM**2,RREFLP**2
*
* ..End Circular Polarisation Output..
*
* ..Reflectances now calculated below..
RRCPOL=((XREFLM+XREFLP)**2+(YREFLM+YREFLP)**2)/4
PRCPOL=DATAN2((YREFLM+YREFLP),(XREFLM+XREFLP))
RRXPOL=((XREFLM-XREFLP)**2+(YREFLM-YREFLP)**2)/4
PRXPOL=DATAN2((XREFLM-XREFLP),(YREFLP-YREFLM))
*
* ..Obtain the Poincare polarisation parameters..
CALL POINCR(DATAN(DSQRT(RRXPOL/RRCPOL)),(PRXPOL-PRCPOL),
+ RELLIP,RTILT)
*
* ..OUTPUT Results..
*
* WRITE(7,996) FREQ/1D9,(PRXPOL-PRCPOL)*180/PI,
* + DATAN(DSQRT(RRXPOL/RRCPOL))*180/PI,RTILT*180/PI,RELLIP*180/PI
CALL OUTPUT(FREQ,RRCPOL,RRXPOL,RELLIP,RTILT,TQUERY,OPFILE)
FREQ=FREQ+FSTEP
20 CONTINUE
*
* ..The next set of statements are the UNTIL conditions..
IF ((I.NE.98).AND.((TQUERY.NE.'Y').AND.(TQUERY.NE.'y')) THEN
WRITE(SCREEN,FMT=998)
READ(KEYBRD,FMT=*) AGAIN
ENDIF
*
* ..The next statement is the conditional UNTIL jump..
IF ((AGAIN.EQ.'Y').OR.(AGAIN.EQ.'y')) GOTO 10
IF ((TQUERY.EQ.'Y').OR.(TQUERY.EQ.'y')) CLOSE(OPFILE)
CLOSE(CIRC)
STOP
999 FORMAT(/A)
998 FORMAT(/'Again? ')
* 996 FORMAT(5F9.2)
END

*
* ..Subroutines..
*
SUBROUTINE FSPAN(FSTART,FSTOP,FSTEP,KEYBRD,SCREEN)
*
* ..Local Scalars..
DOUBLE PRECISION FSTART,FSTOP,FSTEP
*
* ..Executable Statements..
FSTART=75.
FSTOP=110.
FSTEP=.1
WRITE(SCREEN,FMT=899)
READ(KEYBRD,FMT=*,END=1000) FSTART,FSTOP,FSTEP
1000 CONTINUE
FSTART=FSTART*1D9
FSTOP=FSTOP*1D9
FSTEP=FSTEP*1D9
RETURN
899 FORMAT(/'Enter the start frequency, the stop frequency ',
+ 'and the frequency step in GHz : ')
END

*
SUBROUTINE TABLE(TQUERY,OPFILE,NAME,KEYBRD,SCREEN)
*
* ..Local Scalars..
INTEGER OPFILE
CHARACTER TQUERY
CHARACTER*20 NAME,NEWNME
*
* ..Executable Statements..

```

```

WRITE(SCREEN,FMT=699)
READ(KEYBRD,FMT=*) TQUERY
IF ((TQUERY.EQ.'Y').OR.(TQUERY.EQ.'y')) THEN
  WRITE(SCREEN,FMT=698)
  READ(KEYBRD,FMT=*) NEWNME
  IF (NEWNME.EQ.NAME) THEN
    OPFILE=OPFILE-1
  ELSE
    CLOSE(OPFILE-1)
    NAME=NEWNME
    OPEN(OPFILE,FILE=NAME)
  ENDIF
ENDIF
RETURN
699 FORMAT('Do you want a table for UNIGRAPH ? ')
698 FORMAT('Enter the filename for this table: ')
END

*
  SUBROUTINE INPUT(RINDEX,CONDOC,LENGTH,WM,
+                BS,ATTEN,FATTEN,KEYBRD,SCREEN)
*
  ..Local Parameters..
  DOUBLE PRECISION GYRO,PI,ZO
  PARAMETER (GYRO=1.7590D11,PI=3.1415926536,ZO=376.731)
*
  ..Local Scalars..
  DOUBLE PRECISION RINDEX,CONDOC,LENGTH,BS,ATTEN,
+                FATTEN,W,WM,AMONAP,ATTENP
*
  ..Executable Statements..
  RINDEX=5.21
  LENGTH=1.57
  ATTEN=800.
  FATTEN=94.
  BS=0.334
  WRITE(SCREEN,FMT=599)
  READ(KEYBRD,FMT=*,END=1000) RINDEX
  WRITE(SCREEN,FMT=598)
  READ(KEYBRD,FMT=*,END=1000) LENGTH
  WRITE(SCREEN,FMT=597)
  READ(KEYBRD,FMT=*,END=1000) ATTEN,FATTEN
  WRITE(SCREEN,FMT=596)
  READ(KEYBRD,FMT=*,END=1000) BS
1000 CONTINUE
  LENGTH=LENGTH/1D3
  ATTEN=ATTEN/8.69
  FATTEN=FATTEN*1D9
  WM=GYRO*BS
  W=2*PI*FATTEN
  AMONAP=DSQRT((1+(WM/(WM+W)))/(1+(WM/(WM-W))))
  ATTENP=ATTEN/(1+AMONAP)
  CONDOC=ATTENP*2*RINDEX/(ZO*DSQRT(1+(WM/(WM-W))))
  RETURN
599 FORMAT('/Enter the refractive index for the ferrite sheet : ')
598 FORMAT('Enter the thickness of the ferrite sheet in mm : ')
597 FORMAT('Enter the attenuation constant for the ferrite sheet',
+/, 'for linear polarisation in dB/m, followed by the frequency',
+/, 'at which this measurement was made in GHz : ')
596 FORMAT('Enter the magnetic saturation level ',
+ 'for the ferite in Tesla : ')

```

```

      END
*
      SUBROUTINE OPTHDR(TQUERY,OPFILE,SCREEN,RINDEX,CONDOC,LENGTH,
+TBLNUM,TITLE,BS,ATTEN,FATTEN,CIRC)
*
      ..Local Scalars..
      CHARACTER TQUERY
      CHARACTER TITLE*(*)
      INTEGER OPFILE,TBLNUM,CIRC
      DOUBLE PRECISION RINDEX,ATTEN,LENGTH,CONDOC,BS,FATTEN
*
      ..Executable Statements..
      WRITE(SCREEN,FMT=499) TITLE,TBLNUM
      WRITE(SCREEN,FMT=498) RINDEX
      WRITE(SCREEN,FMT=497) LENGTH*1D3
      WRITE(SCREEN,FMT=496) ATTEN*8.69,FATTEN/1D9
      WRITE(SCREEN,FMT=495) BS
      WRITE(SCREEN,FMT=494) CONDOC
      WRITE(SCREEN,FMT=493)
      WRITE(SCREEN,FMT=492)
      WRITE(CIRC,FMT=490) TITLE
      WRITE(CIRC,FMT=489) RINDEX,LENGTH*1D3,ATTEN*8.69,
+FATTEN/1D9,BS,CONDOC
      WRITE(CIRC,FMT=491)
      IF ((TQUERY.EQ.'Y').OR.(TQUERY.EQ.'y')) THEN
        WRITE(OPFILE,FMT=490) TITLE
        WRITE(OPFILE,FMT=489) RINDEX,LENGTH*1D3,ATTEN*8.69,
+ FATTEN/1D9,BS,CONDOC
        WRITE(OPFILE,FMT=488)
      ENDIF
      RETURN
499 FORMAT(/A,' ',I3)
498 FORMAT('/Refractive Index of Ferrite Sheet : ',F6.3)
497 FORMAT('Thickness of Ferrite Sheet : ',F6.2,' mm')
496 FORMAT('Attenuation Constant of Ferrite Sheet : ',F6.1,
+' dB/m',/, 'Attenuation measurement frequency : ',F6.2,' GHz')
495 FORMAT('The saturated magnetisation level was : ',F6.3,' T')
494 FORMAT('The conductivity was calculated to be : ',F6.3,
+' mho/m')
493 FORMAT('/Frequency      Reflectance      ',
+'Polarisation Tilt  Tilt Power  Epsilon')
492 FORMAT(' (GHz)  co-polar  X-polar ',
+' (degrees)      (%)      (degrees)',/)
491 FORMAT('/      Frequency      LHC      RHC')
488 FORMAT('/Frequency Co_refl  X_refl      ',
+'Tilt  Tilt_Power  Epsilon')
490 FORMAT( A)
489 FORMAT('/n: ',F5.3,', l: ',F5.2,', alpha: ',F5.1,', f_alpha: ',
+ F5.2,', Bs: ',F5.3,', sigma: ',F5.3)
      END
*
      SUBROUTINE OUTPUT(FREQ,RRCPOL,RRXPOL,RELLIP,RTILT,TQUERY,OPFILE)
*
      ..Local Parameters..
      DOUBLE PRECISION PI
      PARAMETER (PI=3.1415926536)
*
      ..Local Scalars..
      CHARACTER TQUERY
      INTEGER OPFILE
      DOUBLE PRECISION FREQ,RRCPOL,RRXPOL,RPWR,RTILT,RELLIP

```

```

*      ..Executable Statements..
      RPWR=(DCOS(RELLIP))**2
      WRITE(SCREEN,FMT=399) FREQ/1D9,RRCPOL,RRXPOL,
+RTILT*180/PI,RPWR*100,RELLIP*180/PI
      IF ((TQUERY.EQ.'Y').OR.(TQUERY.EQ.'y')) THEN
        WRITE(OPFILE,FMT=398) FREQ/1D9,RRCPOL,RRXPOL,
+ RTILT*180/PI,RPWR*100,RELLIP*180/PI
      ENDIF
      RETURN
399 FORMAT( F6.2,4X, F6.4,5X, F6.4,8X, F6.2,9X, F6.2,6X, F6.2)
398 FORMAT(2X, F6.2,4X, F6.4,3X, F6.4,2X, F6.2,4X, F6.2,5X, F6.2)
      END

*
      SUBROUTINE ZIN(FREQ,RINDEX,CONDC,LENGTH,RTMU,ZO,XIN,YIN,XF,YF)
*
*      ..Local Scalars..
      DOUBLE PRECISION FREQ,RINDEX,CONDC,LENGTH,ZO,XIN,YIN,RTMU,
+XF,YF,RF,PHIF,RIN,PHIIN,XTANH,YTANH,XNUM,YNUM,XDEN,YDEN,
+RNUM,PHINUM,RDEN,PHIDEN
*
*      ..External Subroutines..
      EXTERNAL PARTS
*
*      ..Executable Statements..
      CALL PARTS(FREQ,RINDEX,CONDC,RTMU,LENGTH,ZO,XF,YF,XTANH,YTANH)
      RF=DSQRT(XF**2+YF**2)
      PHIF=DATAN2(YF,XF)
      XNUM=ZO+XF*XTANH-YF*YTANH
      YNUM=XF*YTANH+YF*XTANH
      XDEN=XF+ZO*XTANH
      YDEN=YF+ZO*YTANH
      RNUM=DSQRT(XNUM**2+YNUM**2)
      PHINUM=DATAN2(YNUM,XNUM)
      RDEN=DSQRT(XDEN**2+YDEN**2)
      PHIDEN=DATAN2(YDEN,XDEN)
      RIN=RF*RNUM/RDEN
      PHIIN=PHIF+PHINUM-PHIDEN
      XIN=RIN*DCOS(PHIIN)
      YIN=RIN*DSIN(PHIIN)
      RETURN
      END

*
      SUBROUTINE PARTS(FREQ,RINDEX,CONDC,RTMU,LENGTH,ZO,
+XF,YF,XTANH,YTANH)
*
*      ..Parameters..
      DOUBLE PRECISION PI,EPS0,C
      PARAMETER (PI=3.1415926536,EPS0=8.854185D-12,C=299.7925D+6)
*
*      ..Local Scalars..
      DOUBLE PRECISION FREQ,RINDEX,CONDC,LENGTH,ZO,XF,YF,
+XTANH,YTANH,DELTA,BETA,ALPHA,RTMU
*
*      ..External Subroutines..
      EXTERNAL MYTANH
*
*      ..Executable Statements..
      XF=ZO*RTMU/RINDEX
      YF=(ZO*RTMU/RINDEX)*CONDC/(4*PI*FREQ*EPS0*(RINDEX**2))
      ALPHA=CONDC*ZO*RTMU/(2*RINDEX)
      DELTA=(CONDC**2)/(32.*(PI**2)*(FREQ**2)*((EPS0*(RINDEX**2))**2))
      BETA=(2.*PI*FREQ*RINDEX*RTMU/C)*(1+DELTA)
      CALL MYTANH(ALPHA*LENGTH,BETA*LENGTH,XTANH,YTANH)
      RETURN

```



```

      END
*
      SUBROUTINE MYTANH(X,Y,XTANH,YTANH)
*
      ..Local Scalars..
      DOUBLE PRECISION X,Y,XTANH,YTANH,R,PHI
*
      ..Executable Statements..
      R=DSQRT((DCOSH(2*X)-DCOS(2*Y))/(DCOSH(2*X)+DCOS(2*Y)))
      PHI=DATAN2(DSIN(2*Y),DSINH(2*X))
      XTANH=R*DCOS(PHI)
      YTANH=R*DSIN(PHI)
      RETURN
      END
*
      SUBROUTINE POINCR(G,D,ELLIP,TILT)
*
      ..Local Parameters..
      DOUBLE PRECISION PI
      PARAMETER (PI=3.1415926536)
*
      ..Local Scalars..
      DOUBLE PRECISION G,D,ELLIP,TILT,TMP
*
      ..Executable Statements..
      ELLIP=(DASIN(DSIN(2*G)*DSIN(D)))/2
      TMP=DTAN(2*G)
      TILT=(DATAN(TMP*DCOS(D)))/2
      IF (TMP.LT.0) THEN
        TILT=TILT+(PI/2)
      ENDIF
      RETURN
      END
*
      SUBROUTINE PROPGN(FREQ,RINDEX,CONDUCT,ZO,RTMU,ALPHA,BETA)
*
      ..Parameters..
      DOUBLE PRECISION PI,EPS0,C
      PARAMETER (PI=3.1415926536,EPS0=8.854185D-12,C=299.7925D+6)
*
      ..Local Scalars..
      DOUBLE PRECISION FREQ,RINDEX,CONDUCT,ZO,RTMU,ALPHA,BETA,DELTA
*
      ..Executable Statements..
      ALPHA=CONDUCT*ZO*RTMU/(2*RINDEX)
      DELTA=(CONDUCT**2)/(32.*(PI**2)*(FREQ**2)*((EPS0*(RINDEX**2))**2))
      BETA=(2.*PI*FREQ*RINDEX*RTMU/C)*(1+DELTA)
      RETURN
      END
*

```

Appendix E

PSI13 : A Gaussian Beam-Mode Model

Program Listing

```
*      A program to evaluate an algebraic expression
*      for the far-field of an SLM which imposes a
*      180 degree phase shift on one half of the beam
*      incident upon it---a fundamental mode Gaussian
*      beam which is axially symmetric. The expression
*      is a one dimensional expression and incorporates
*      the first and third order modes only of the
*      multi-mode beam expansion.
*
*      STANDARD FORTRAN 77
*
*      M. R. Webb
*      June 26, 1992
*
*      PROGRAM PSI13
*      ..Parameters..
*      INTEGER KEYBRD,SCREEN,OUTPUT
*      PARAMETER (KEYBRD=5,SCREEN=6,OUTPUT=99)
*      DOUBLE PRECISION PI,RTPI,RT3,RT3PI,RT2,RES
*      PARAMETER (PI=3.1415926536,RTPI=1.7724538509,
+          RT3=1.7320508076,RT3PI=RTPI*RT3,
+          RT2=1.4142135624,RES=0.1*PI/180.)
*      CHARACTER TITLE*(*)
*      PARAMETER (TITLE='Far-field pattern: Gaussian beam-modes [1,3]')
*      ..Local Scalars..
*      INTEGER I,N
*      DOUBLE PRECISION PSI,THETA,THETA1,THETA2,
+          OMEGA0,LAMBDA,K,PARAM,A,B,C
*
*      ..Main Program..
*
*      OPEN(OUTPUT,FILE='pattern13.dat')
```

```

WRITE(OUTPUT,FMT=999) TITLE
WRITE(OUTPUT,FMT=995)
WRITE(SCREEN,FMT=999) TITLE
THETA1=-30.*PI/180.
THETA2=30.*PI/180.
OMEGA0=0.0044
LAMBDA=0.003331028
WRITE(SCREEN,FMT=998)
READ(KEYBRD,FMT=*,END=1000) THETA1,THETA2
WRITE(SCREEN,997)
READ(KEYBRD,FMT=*,END=1000) OMEGA0,LAMBDA
THETA1=THETA1*PI/180
THETA2=THETA2*PI/180
OMEGA0=OMEGA0/1D-3
LAMBDA=LAMBDA/1D-3
1000 CONTINUE
K=2*PI/LAMBDA
N=IDNINT((THETA1-THETA2)/RES)
N=IABS(N)
THETA=THETA1
DO 10 I=1,N+1
PARAM=K*OMEGA0*DTAN(THETA)
A=PARAM/RTPI
B=-((PARAM/RT2)**3)/(6*RT3PI)
C=PARAM/(RT2*4*RT3PI)
PSI=DEXP(-(PARAM*PARAM)/4)*(A+B+C)
WRITE(OUTPUT,FMT=996) THETA*180/PI,PSI,PSI*PSI,10*DLOG10(PSI*PSI)
THETA=THETA+RES
10 CONTINUE
CLOSE(OUTPUT)
STOP
999 FORMAT(/A)
998 FORMAT(/'Enter the two angle limits:      ')
997 FORMAT(/'Enter beamwaist size and wavelength:  ')
996 FORMAT(1X,F7.1,3X,2F12.8,F10.2)
995 FORMAT(/'   angle      field      power      dB',/)
END

```